U.S. DEPARTMENT OF COMMERCE
National Technical Information Service

PB-252 506

Spectral Modeling of Atmospheric Flows and Turbulent Diffusion

Flow Research, Inc.

Prepared For
Environmental Sciences Research Lab.

January 1976

KEEP UP TO DATE

Between the time you ordered this report—which is only one of the hundreds of thousands in the NTIS information collection available to you—and the time you are reading this message, several *new* reports relevant to your interests probably have entered the collection.

Subscribe to the **Weekly Government Abstracts** series that will bring you summaries of new reports *as soon as they are received by NTIS* from the originators of the research. The WGA's are an NTIS weekly newsletter service covering the most recent research findings in 25 areas of industrial, technological, and sociological interest—invaluable information for executives and professionals who must keep up to date.

The executive and professional information service provided by NTIS in the **Weekly Government Abstracts** newsletters will give you thorough and comprehensive coverage of government-conducted or sponsored research activities. And you'll get this important information within two weeks of the time it's released by originating agencies.

WGA newsletters are computer produced and electronically photocomposed to slash the time gap between the release of a report and its availability. You can learn about technical innovations immediately—and use them in the most meaningful and productive ways possible for your organization. Please request NTIS-PR-205/PCW for more information.

The weekly newsletter series will keep you current. But *learn what you have missed in the past* by ordering a computer **NTISearch** of all the research reports in your area of interest, dating as far back as 1964, if you wish. Please request NTIS-PR-186/PCN for more information.

WRITE: Managing Editor
5285 Port Royal Road
Springfield, VA 22161

Keep Up To Date With SRIM

SRIM (Selected Research in Microfiche) provides you with regular, automatic distribution of the complete texts of NTIS research reports *only* in the subject areas you select. SRIM covers almost all Government research reports by subject area and/or the originating Federal or local government agency. You may subscribe by any category or subcategory of our WGA **(Weekly Government Abstracts)** or **Government Reports Announcements and Index** categories, or to the reports issued by a particular agency such as the Department of Defense, Federal Energy Administration, or Environmental Protection Agency. Other options that will give you greater selectivity are available on request.

The cost of SRIM service is only 45¢ domestic (60¢ foreign) for each complete microfiched report. Your SRIM service begins as soon as your order is received and processed and you will receive biweekly shipments thereafter. If you wish, your service will be backdated to furnish you microfiche of reports issued earlier.

Because of contractual arrangements with several Special Technology Groups, not all NTIS reports are distributed in the SRIM program. You will receive a notice in your microfiche shipments identifying the exceptionally priced reports not available through SRIM.

A deposit account with NTIS is required before this service can be initiated. If you have specific questions concerning this service, please call (703) 451-1558, or write NTIS, attention SRIM Product Manager.

This information product distributed by

NTIS U.S. DEPARTMENT OF COMMERCE
National Technical Information Service
5285 Port Royal Road
Springfield, Virginia 22161

138191

PB 252 506

EPA-600/4-76-007
January 1976

Environmental Monitoring Series

SPECTRAL MODELING OF ATMOSPHERIC FLOWS AND TURBULENT DIFFUSION

REPRODUCED BY
NATIONAL TECHNICAL
INFORMATION SERVICE
U.S. DEPARTMENT OF COMMERCE
SPRINGFIELD, VA. 22161

Environmental Sciences Research Laboratory
Office of Research and Development
U.S. Environmental Protection Agency
Research Triangle Park, North Carolina 27711

154

RESEARCH REPORTING SERIES

Research reports of the Office of Research and Development, U.S. Environmental Protection Agency, have been grouped into five series. These five broad categories were established to facilitate further development and application of environmental technology. Elimination of traditional grouping was consciously planned to foster technology transfer and a maximum interface in related fields. The five series are:

1. Environmental Health Effects Research
2. Environmental Protection Technology
3. Ecological Research
4. Environmental Monitoring
5. Socioeconomic Environmental Studies

This report has been assigned to the ENVIRONMENTAL MONITORING series. This series describes research conducted to develop new or improved methods and instrumentation for the identification and quantification of environmental pollutants at the lowest conceivably significant concentrations. It also includes studies to determine the ambient concentrations of pollutants in the environment and/or the variance of pollutants as a function of time or meteorological factors.

This document is available to the public through the National Technical Information Service, Springfield, Virginia 22161.

TECHNICAL REPORT DATA
(Please read Instructions on the reverse before completing)

1. REPORT NO. EPA-600/4-76-007	2.	3. RECIPIENT'S ACCESSION NO.
4. TITLE AND SUBTITLE SPECTRAL MODELING OF ATMOSPHERIC FLOWS AND TURBULENT DIFFUSION		5. REPORT DATE January 1976 6. PERFORMING ORGANIZATION CODE
7. AUTHOR(S) Arthur Bass, Steven A. Orszag		8. PERFORMING ORGANIZATION REPORT NO.
9. PERFORMING ORGANIZATION NAME AND ADDRESS Flow Research, Inc. (N.E. Division) 1 Broadway Cambridge, MA 02142		10. PROGRAM ELEMENT NO. 1AA009 11. CONTRACT/GRANT NO. EPA 68-02-1297
12. SPONSORING AGENCY NAME AND ADDRESS Environmental Sciences Research Laboratory Office of Research and Development U.S. Environmental Protection Agency Research Triangle Park, North Carolina 27711		13. TYPE OF REPORT AND PERIOD COVERED Final 14. SPONSORING AGENCY CODE EPA-ORD

15. SUPPLEMENTARY NOTES

16. ABSTRACT

This report presents a survey of discrete spectral and pseudospectral numerical methods to simulate atmospheric flow and turbulent diffusion. Some applications of these methods to air quality simulation modeling are presented. A three-dimensional spectral incompressible numerical model is described in detail. Computational resource limitations precluded successful evaluation of eddy Austauch coefficients. Some numerical results are presented for the rate of relaxation of anisotropic flows.

Recommendations and suggestions for further research are made concerning the prospective utility of these spectral methods for air quality simulation modeling.

PRICES SUBJECT TO CHANGE

17. KEY WORDS AND DOCUMENT ANALYSIS

a. DESCRIPTORS	b. IDENTIFIERS/OPEN ENDED TERMS	c. COSATI Field/Group
* Numerical analysis Turbulence * Turbulent diffusion Air flow Air pollution Environmental simulation * Mathematical models		12A 20D 04A 13B 14B

18. DISTRIBUTION STATEMENT RELEASE TO PUBLIC	19. SECURITY CLASS *(This Report)* UNCLASSIFIED	21. NO. OF PAGES 154
	20. SECURITY CLASS *(This page)* UNCLASSIFIED	22. PRICE $6.75-2.25

EPA Form 2220-1 (9-73)

EPA-600/4-76-007
January 1976

SPECTRAL MODELING OF ATMOSPHERIC FLOWS AND TURBULENT DIFFUSION

by

Arthur Bass, Steven A. Orszag
Flow Research, Inc. (N.E. Division)
1 Broadway
Cambridge, MA 02142

Contract No. 68-02-1297

Project Officer

Kenneth L. Calder
Meteorology and Assessment Division
Environmental Sciences Research Laboratory
Research Triangle Park, North Carolina 27711

U.S. ENVIRONMENTAL PROTECTION AGENCY
OFFICE OF RESEARCH AND DEVELOPMENT
ENVIRONMENTAL SCIENCES RESEARCH LABORATORY
RESEARCH TRIANGLE PARK, NORTH CAROLINA 27711

DISCLAIMER

This report has been reviewed by the Environmental Sciences Research Laboratory, U.S. Environmental Protection Agency, and approved for publication. Approval does not signify that the contents necessarily reflect the views and policies of the U.S. Environmental Protection Agency, nor does mention of trade names or commercial products constitute endorsement or recommendation for use.

Preface

In order to provide a strong quantitative basis for air quality management through selective emission controls, there have been increasing demands in recent years for air quality simulation models of considerable sophistication and complexity. In these models a major component is that describing the atmospheric transport and turbulent dispersion of the pollutants, and many efforts are in progress to improve the specification of these effects. For the turbulent dispersion this is normally done through the use of diffusion coefficients (eddy diffusivities) or by more sophisticated turbulence parameterizations that are developed through various "closure" schemes for the governing equations of flow. These closure approximations are, of course, necessary because of the well-known mathematical intractability of the general non-linear time-dependent Navier-Stokes equations that govern the turbulent flow of a viscous fluid. Closure approximations all involve the use, at some stage in their development, of empirically based constants of parameters, that in some cases may require ad hoc field experiments or observations.

During the past few years, and largely stemming from the pioneering efforts of Professor Steven A. Orszag and his associates, a major breakthrough has been made in developing powerful new mathematical-computational approaches for the accurate numerical simulation of turbulent flow. It has been shown that many aspects of turbulent motion may be numerically simulated with impressive accuracy, directly from the equations of motion, and without the somewhat arbitrary closure approximations involved in normal parameterizations. It was these remarkable results that stimulated the present contract. It was hoped that it might provide the initial step towards providing a basic technique for atmospheric turbulence and dispersion estimates by accurate non-empirical methods. In due course such results might provide a set of diffusion data against which various approximations might be tested.

The recent methods of Professor S. A. Orszag involve so-called spectral techniques, along with sophisticated computer programming. These techniques require expansion of the dependent variable into a Fourier (or other orthogonal) series of smooth functions. The calculation proceeds by performing certain of the mathematical operations in Fourier (or other) space and others in physical configuration space, according to the mathematical form of the operation and its relative efficiency. Transformations between the two spaces are made by Fast Fourier Transform (FFT) methods and the use of special computational techniques. In addition to having very powerful applications to the problems of turbulent flow and dispersion, the spectral technique has a wide potential for numerical simulation of many atmospheric flows. The present report attempts to provide an overview of such applications. It also compares the accuracy and advantages of spectral techniques, with the more conventional finite-difference numerical techniques for the solution of partial differential equations. In some places a tutorial-type presentation results, from the attempt to provide adequate references and to make the potential of spectral methods more familiar to the developers of meteorological air quality simulation models. In addition, it provides an account of an initial research attempt to develop direct solutions, without parameterization approximations, for turbulent dispersion of an inert pollutant in a thermally stratified atmospheric layer that is governed by the Boussinesq equation. Unfortunately, this research failed to reach its desired goal during the relatively short period of the contract, although in anticipation of renewed efforts along similar lines in the future, a fairly detailed account is desirable.

As an example of the power of spectral techniques, some new results in turbulence dynamics are presented, concerning the rate of relaxation of anisotropic flows to asymptotic isotropy.

Finally, general recommendations are made concerning the potential utility of spectral methods in a number of specific problem areas, and specific suggestions are given concerning the prospective improvement of several existing air quality simulation models, using these spectral methods.

Kenneth L. Calder
Project Officer

Environmental Portection Agency
Research Triangle Park
North Carolina
October, 1975

CONTENTS

Page

Title Page i

Disclaimer Page ii

Preface iii

Contents vii

List of Figures ix

List of Tables x

Acknowledgements xi

1.0 Introduction 1

2.0 Overview of Numerical Techniques for Meteorological Flow Simulations 3

2.1 Comparative Accuracy of Finite Difference and Finite Spectral Methods 11

3.0 Spectral Methods 25

3.1 Boundary Conditions and Geometries 31

3.2 Treatment of Boundary Layers 33

3.3 Pseudospectral Methods 39

4.0 Applications of Numerical Spectral Methods 45

5.0 Comparison of Methods of Spectral and Finite Difference Methods for Two Examples 48

5.1 Comparison of Methods for the Diffusive Color Problem 48

5.2 Comparison of Methods for Neuringer's Problem 65

6.0 Spectral Modeling of the Turbulent Diffusion of a Passive Scalar 77

6.1 The Numerical Model 79

6.2 Physical Parameters 86

6.3 An Unsuccessful Experiment 88

CONTENTS (CONT'D)

Page

7.0 Relaxation of Anisotropic Turbulence to Isotropy 107

8.0 Recommendations for Future Research 113

9.0 References 115

Appendix 1 The Data Content of Discrete-Grid Representations 118

Appendix 2 Discrete Fourier Transform Representations 121

Appendix 3 Elimination of Aliasing in Discrete Real-Space Multiplications 124

Appendix 4 The Fast Fourier Transform 132

Appendix 5 Construction of Initial Perturbation Flow Field 138

LIST OF FIGURES

Number Page

5.1 Initial Point-Source Distribution ($t = 0$). . . 52

5.2 Finite-Difference Scheme, 32 x 32 point resolution, $\nu = .05$, $t = 1/4$ revolution 53

5.3 Spectral Scheme, 32 x 32 point resolution, $\nu = 0.5$, $t = 1/4$ revolution 54

5.4 Finite-Difference Scheme, 32 x 32 point resolution, $\nu = .05$, $t = 1/2$ revolution 55

5.5 Spectral Scheme 32 x 32 point resolution, $\nu = .05$, $t = 1/2$ revolution 56

5.6 Finite-Difference Scheme, 32 x 32 point resolution, $\nu = .005$, $t = 1/4$ revolution 57

5.7 Spectral Scheme, 32 x 32 point resolution, $\nu = .005$, $t = 1/4$ revolution 58

5.8 Finite-Difference Model, 32 x 32 point resolution, $\nu = .005$, $t = 1/2$ revolution 59

5.9 Spectral Model, 32 x 32 point resolution, $\nu = .005$, $t = 1/2$ revolution 60

5.10 Correct Neuringer FCN for $\gamma = 1$, $\bar{t} = 0.5$ . . 67

5.11 Neuringer Problem ($\gamma = 1.0$, $\bar{t} = 0.5$) Analytic Value of $F(\bar{x},\bar{y})/F(0,0)$ 68

6.1A U Field (y-z projection), $t = 0$ 90

6.1B U Field (y-z projection), $t = 10^3$ sec 91

6.1C U Field (y-z projection), $t = 2 \times 10^3$ sec . . 92

6.2A U Field (x-z projection), $t = 0$ 93

6.2B U Field (x-z projection), $t = 10^3$ sec 94

6.2C U Field (x-z projection), $t = 2 \times 10^3$ sec . . 95

6.3A U Field (x-y projection), $t = 0$ 96

6.3B U Field (x-y projection), $t = 10^3$ sec 97

6.3C U Field (x-y projection), $t = 2 \times 10^3$ sec . . 98

LIST OF FIGURES (CONT)

Number		Page
6.4A	V Field (y-z projection), $t = 0$	99
6.4B	V Field (y-z projection), $t = 10^3$ sec	100
6.4C	V Field (y-z projection), $t = 2 \times 10^3$ sec	101
6.5A	W Field (y-z projection), $t = 0$	102
6.5B	W Field (y-z projection), $t = 10^3$ sec	103
6.5C	W Field (y-z projection), $t = 2 \times 10^3$ sec	104
7.1	Time History of $R_a(t)$ for $E_1(0) = 0$ and $E_1(0) = 1/2E_2(0)$	110

LIST OF TABLES

Number		Page
2.1	Phase Errors for $\alpha = 0.1$	13
5A	Analytic Evaluation of $F(\bar{x},\bar{y})/F(0,0)$ for $\gamma = 1.0$, $\bar{t} = 0.5$	69
5B	Analytic Value of $F(\bar{x},\bar{y})/F(0,0)$, $\gamma = 4.0$, $\bar{t} = 0.5$	71
5C	Absolute Errors in Spectral Run	72
5D	Absolute Errors in 48*48 Point Finite Difference Run	73
5E	Absolute Errors in 96*96 Point Finite Difference Run	74

Acknowledgements

We acknowledge with thanks the constructive suggestions of K. L. Calder, R. Eskridge, and K. L. Dermerjian, who have contributed greatly to the effectiveness of this report. We are especially greatful to K. L. Calder for suggesting to us the spectral simulation of Neuringer's problem.

1.0 Introduction

Advances in computer technology, together with important achievements in the design of efficient numerical algorithms, have begun to make practical the use of direct spectral methods for numerical simulations of many fluid flow problems. In a spectral method, the dependence of the flow variables upon one or more of the spatial coordinates is represented by expansions in a discrete series of smooth orthogonal functions (Fourier series expansions being the most familiar). The governing dynamic equations are then reformulated as equations relating the spectral coefficients of the fields so analyzed. To permit numerical computation, the expansions are truncated to some finite upper mode. The resolution and accuracy properties of spectral methods are very different from those of the more familiar finite-difference methods, although both classes of methods are related to discrete spatial grids.

Although rapidly growing in popularity, these spectral methods are as yet relatively unfamiliar to large segments of the meteorological communities. We have attempted, therefore, to provide a brief review of some important finite spectral methods for a variety of flow simulations relevant to air quality modeling. The report discusses at some length the relative advantages and disadvantages of finite-difference and finite spectral techniques, especially in regard to ease of implementation, accuracy, and physical utility. Implicit in this description is a clear understanding of the considerations which influence the choice of a particular spectral approach, and determine its range of utility. We have included in Appendix 1, a discussion of the resolution implications of discrete-grid methods, from the point of view of both finite-difference and finite spectral representations.

Next, a review is made of the current state of spectral modeling in a variety of geophysical fluid flow problem areas for which spectral methods have proved fruitful and/or hold much prospective promise: (a) numerical weather prediction, (b) turbulence modeling, (c) methods for advective-diffusive simulations.

In the course of the current contract effort, we have developed a spectral model for the direct simulation of fully three-dimensional, non-linear, time-dependent, turbulent, incompressible flows, and a corresponding computer program for the solution of the Navier-Stokes equations using high-resolution Fourier spectral methods. The model has been designed to treat, within the Boussinesq approximation, the influence of differing stratification profiles upon the spectral evolution of turbulent flow fields. We have attempted, using this program, to study the evolution of a passive scalar field in a sheared, turbulent velocity field, but unforeseen limitations in computer core and running time precluded the attainment of physically realistic results. More successfully, the program was used to look at an important problem in turbulence transport theory, that is the rate at which an initially anistropic flow will relax to isotropy; the relaxation time constant is an important term in some turbulence closure models.

A two-dimensional version of these finite spectral methods has been used for the accurate simulation of two advective-diffusive point-source problems, which may have useful implications for air quality modeling efforts in which discrete point sources are to be represented. It is shown that, in the two cases, finite spectral methods offer significant advantages, both with regard to accuracy and computer storage requirements, compared with finite-difference representations of the same problems.

Finally, recommendations are made concerning the practical uses to which such finite-spectral methods can be put, in the present state of air quality modeling, and in the light of more realistic assessment of available computational resources.

2.0 Overview of Numerical Techniques for Meteorological Flow Simulations

The historical development of numerical methods for the simulation of meteorological and other fluid flows can be traced back to the early part of the century. Especially noteworthy is the pioneering manual forecast effort of L.F. Richardson, during the first World War. Although unsuccessful, this effort provided later generations of numericists with much insight into the limitations imposed by small-scale phenomena which are meteorologically irrelevant, but whose implicit presence in a numerical model leads to computational catastrophe. The impetus of technological progress during the second World War spurred greatly the development of numerical methods for shockwave and other supersonic model calculations, and resulted in the first systematic examinations of finite-difference numerical models for such calculations. With the advent of high-speed calculational devices by the early fifties, it became practical to attempt the first numerical weather predictions (Fjortoft, Von Neumann, Charney), using simple models which isolated, by suitable scaling arguments, the meteorologically-relevant large scales of motion and eliminated the small-scale structural behavior which had frustrated Richardson's efforts thirty years before. The first such numerical forecasts were performed by constructing finite-difference approximations for the evolution of the two-dimensional inviscid barotropic vorticity equation

$$(2.1) \qquad \left(\frac{\partial}{\partial t} + \underline{V}\cdot\nabla\right)(\zeta+f) = 0$$

where $\underline{V}\,(\underline{x},t) = u(\underline{x},t)\hat{\imath} + v(\underline{x},t)\hat{\jmath}$ is the horizontal velocity field, f is the Coriolis parameter, and $\zeta = \frac{\partial v}{\partial x} - \frac{\partial u}{\partial y}$ is the geostrophic vorticity. Considerably more ambitious simulations were soon attempted in a variety of fluid-mechanical contexts, beginning from the viscous, incompressible Navier-Stokes equations:

$$(2.2) \qquad \left(\frac{\partial}{\partial t} + \underline{V}\cdot\nabla\right)\underline{V} = -\frac{\nabla P}{\rho} + \nu\nabla^2\underline{V}$$

$$(2.3a) \qquad \nabla\cdot\underline{V} = 0$$

where $P(\underline{x},t)$ is the pressure, ρ the (constant) density, and ν the kinematic viscosity. Using the incompressibility condition (2.3a) one obtains a Poisson equation for the pressure field,

$$(2.3b) \qquad \frac{1}{\rho}\nabla^2 P = -\nabla\cdot(\underline{V}\cdot\nabla)\underline{V} \quad .$$

Extensions of such models to slightly compressible flows (in the Boussinesq sense) provide the needed coupling of flow kinematics and thermodynamics.

It was soon recognized that the proper formulation of boundary conditions is among the most crucial difficulties encountered in numerical flow simulations. Appropriate boundary conditions may include (a) the specification of the velocity V at no-slip boundaries; (b) the specification of V_n and $\frac{\partial}{\partial n} V_\tau$ at no-stress boundaries (n and τ are respectively, the normal and tangential directions to the boundary); (c) the specification of boundary-layer momentum flux when such fluxes cannot be computed explicitly; (d) thermal boundary conditions, (e) the choice of inflow and outflow boundary conditions for systems whose natural boundaries lie outside the designated computational boundaries, (f) the incorporation of topographic influences and differences in land-sea surface properties. The problems associated with imposition of boundary conditions remain, by and large, the principal impediments to truly accurate numerical flow evolution, and continue to be areas of intensive investigation.

The most widely applicable and popular numerical methods for flow simulations are based upon finite-difference approximations, in one or more geometries, to various versions or extensions of (2.1 - 2.3); comprehensive reviews of finite-difference methods have been provided by Fromm (1970), Kreiss and Oliger (1973), Roache (1972), to name but a few. Difference methods fall into several general classes. We may distinguish, first, between those difference schemes developed for Eulerian, and those developed for Lagrangian, versions of the equations of motion. In the Lagrangian formulation, the coordinate system is embedded in the moving fluid. For flows which are relatively uncomplicated, and not subject to extreme distortions, such methods can lead to accurate results, while accurately preserving advection properties and real discontinuities. However, for sufficiently disorganized flows, the Lagrangian mesh becomes badly distorted, and the calculational accuracy quickly deteriorates. Lagrangian methods have been especially popular in the simulation of strongly compressible flows.

Eulerian systems, in which the coordinate grid is fixed, are much less susceptible to violent computational breakdown as the fluid undergoes large distortion. The penalty paid is the corresponding loss of accuracy in the representation of advection, diffusion, and flow discontinuities. We shall discuss some of these difficulties shortly.

Difference methods may be also distinguished with respect to the choice of variables which are computed prognostically, and those obtained diagnostically. A variable is said to be computed prognostically if the equation used to govern its temporal evolution explicitly includes its time-dependence. For example, the velocity field in (2.2) is a prognostic variable. A variable is said to be diagnostic when the equation used to govern its temporal evolution makes no explicit reference to its time dependence. For example, the pressure field in (2.3) is a diagnostic variable, since its change with time is entirely implicit in the time variation of the velocity field. These choices are far from trivial to make and govern the physical realism which will inhere to the computation. For example, in two-dimensional versions of (2.1 - 2.3) one may solve directly for the variables $\underline{V}$ and P, or alternatively, convert to the vorticity-stream function formulation

(2.4) $$\frac{\partial\zeta}{\partial t} + J(\psi,\zeta) = \nu\nabla^2\zeta$$

where ψ is the stream function defined by

(2.5a) $$u = -\frac{\partial\psi}{\partial y}, \qquad v = \frac{\partial\psi}{\partial x}$$

(2.5b) $$\zeta = \nabla^2\psi$$

and $J(\psi,\zeta)$ is the Jacobian $(\psi_x\zeta_y - \psi_y\zeta_x)$. That is, we solve (2.4) prognostically for ζ, and then obtain ψ by inversion of the Poisson equation (2.5b). The system (2.4 - 2.5) is attractive because it expresses explicitly an important dynamical property, namely the conservation of vorticity under horizontal advection (in the absense of viscous losses). In this formulation, the system preserves the energy integral in a very natural manner as can be demonstrated by multiplying (2.4) by ψ and integrating over space. From the computational point of view, as well, the vorticity-streamfunction approach is particularly appealing because vorticity is the most important dynamical property which governs the evolution of incompressible slightly viscous flows. On the other hand, the pressure (governed by the elliptic equation (2.3b)) is affected instantaneously at all points of space. Thus, with limited spatial resolution and extent, it should be easier to determine time-dependent flows accurately using the vorticity-streamfunction method. However, this expectation is not borne out in practice. Primitive-variable simulations tend to be slightly more accurate for similar computational labor (Orszag 1971a) probably because (2.5) requires finite-difference approximations to more critical derivatives than does (2.1).

However, the vorticity-streamfunction idea is still very useful for the determination of boundary conditions in primitive variable simulations (Orszag and Israeli 1974).

The ability of an inviscid numerical scheme to conserve energy and enstrophy (square vorticity) is an important consideration from the point of view of physical realism, and long-term computational stability. Let us consider briefly how well such properties are preserved by finite-difference schemes. If the Jacobian in (2.4) is evaluated using second-order centered differences on a uniform grid the resulting scheme violates energy and enstrophy conservation. Therefore, Arakawa (1966, 1970) proposed that the Jacobian be approximated by second-order centered differences when it is first written in the equivalent form

$$(2.6) \qquad J = \frac{1}{3}[(\zeta\psi_x)_y - (\zeta\psi_y)_x + \psi_x\zeta_y - \psi_y\zeta_x + (\psi\zeta_y)_x - (\psi\zeta_x)_y]$$

If (2.6) is approximated by second-order centered differences, the discrete analogs of energy and enstrophy conservation

$$(2.7) \qquad \iint \psi J \, dx \, dy = 0; \quad \iint \zeta \, J \, dx \, dy = 0$$

respectively, are preserved. Arakawa's energy-conserving methods have been very popular in recent years, apparently because it has been believed that energy conservation is necessary to avoid nonlinear computational instability (Phillips 1959), usually called "aliasing" instability. However, energy-conserving finite-difference schemes may not be as useful as expected. The Arakawa schemes "semi-conserve" energy; that is, they conserve energy only in the absence of time-differencing errors, but Kreiss & Oliger (1972) have given examples of schemes that semi-conserve energy but that are unstable when leapfrog time-differencing is used. In general, though, Arakawa-type schemes are less susceptible to numerical instability than straightforward centered schemes (Grammeltvedt 1969). They are, however, considerably less efficient and yet not noticeably more accurate. It is now understood that aliasing instability will appear only in simulations with inadequate grid resolution) (Orszag 1971a, 1972, Fornberg 1972, Kreiss & Oliger 1973), and the deliberate use of an energy-conserving scheme to avoid aliasing instability may lead to a grossly inaccurate simulation.

Among the most attractive features of the spectral methods to be discussed is the ease with which in the inviscid case energy and enstrophy are preserved in the absense of time-differencing errors. This is mainly due to the accuracy with which phase and amplitude information is retained using a spectral form of the Jacobian term.

An essential part of the vorticity-streamfunction method is the inversion of the Poisson equation (2.5b). In a finite difference scheme, the inversion is performed by a standard relaxation method. In a spectral scheme, the inversion is trivial, and direct spectral methods, rather than relaxation methods, should be used whenever possible (Hockney 1970, Dorr 1970, Swartztrauber 1972).

Primitive-variable methods are increasingly widespread, especially in three-dimensional NWP simulations. In the staggered-mesh second-order scheme (Fromm 1963, Lilly 1965, Harlow and Welch 1965, Orszag 1969, Williams 1969, Deardorff 1970), velocities are defined at cell boundaries and pressures at cell centers. It has the attractive features of efficiency, small truncation error and energy semiconservation. The Poisson equation for the pressure is most conveniently solved by direct spectral methods. Harlow and Welch (1965) and Piacsek and Williams (1970) have developed techniques to ensure compliance with the incompressibility condition; these are especially useful when relaxation methods are used to solve (2.2, 2.3).

2.1 Comparative Accuracy of Finite Difference and Finite Spectral Methods

In this section we compare finite difference and finite spectral methods with regard to several important classes of numerical error. These may be identified as follows:

(2.1.1) First-Differencing Phase Errors

Consider the usual approximation to the first derivative $\partial A/\partial x$' where A is a scalar function of the spatial variable x:

$$\left(\frac{\partial A}{\partial x}\right)_{x_i} = \frac{A(x_{i+1}) - A(x_{i-1})}{2\Delta x} . \tag{2.8}$$

Suppose we are attempting to represent in this manner the first derivative of the sinusoid function $A(x) = e^{iKX}$. Then the ratio of the approximation (2.8) to the exact result $iK\,A(x)$ is given by $\sin(K\Delta x)/K\Delta x$. This ratio approaches unity only in the limit $K\Delta x \to 0$. Note, that for large K and finite Δx, the approximation (2.8) becomes progressivly poorer. In particular for $K \to \pi/\Delta x$, i.e., as we approach the limit of spectral resolution of the finite mesh, the ratio approaches zero, which is hardly acceptable if there is significant information contained at wavenumbers near the truncation limit N/2. Consider now the effect of such first-differencing errors upon the solution of the one-dimensional advection equation (N is the number of mesh intervals in the grid)

$$\frac{\partial}{\partial t} A(x,t) + U\frac{\partial}{\partial x} A(x,t) = 0 \tag{2.9}$$

where U is a constant, uniform advecting velocity. The solutions to (2.9) can be synthesized by linear combinations of waves of the form

$$A_n(x,t) = e^{iK_n(x-Ut)}. \tag{2.10}$$

In fact, if the values of $A(x,t)$ are given on N discrete points equally spaced by Δx, an arbitrary excitation on these N points may be approximately represented as a linear combination of the N solutions (2.10) with $K\Delta x = 2\pi m/N$ $(-\frac{N}{2} \leq m < \frac{N}{2})$, m integral.

The leapfrog centered "$2\Delta x$ difference" approximation to (2.9) is

$$A_j^{n+1} = A_j^{n-1} - \alpha(A_{j+1}^n - A_{j-1}^n) \tag{2.11}$$

where $A_j^n = A(j\Delta x, n\Delta t)$, Δt is the time increment, and $\alpha = U\Delta t/\Delta x$. The finite-difference equation (2.11) is satisfied by

$$A_j^n = e^{i(Kj\Delta x - n\theta)} \tag{2.12}$$

where $\sin\theta = \alpha\sin(K\Delta x)$. If $|\alpha| \leq 1$ then θ is real for all K and hence the scheme is neutrally stable. In each time step, the exact change of phase of $A(x,t)$ given by (2.10) is $-KU\Delta t = -K\alpha\Delta x$ while the change of phase of (2.12) $= -\theta = -\sin^{-1}[\alpha\sin K\Delta x]$. Since $|\theta/(K\alpha\Delta x)|<1$ when $|\alpha|<1$ and $|K\Delta x| \leq \pi$, it follows that the waves (2.12) lag the true waves (2.10).

Let us compare the ratio of $\delta=\theta/K\alpha\Delta x$ the computational phase θ to the true phase $K\alpha\Delta x$, for the system (2.9), in each of the following three schemes:

(a) second-order Arakawa finite-differencing (Arakawa, 1966)

(b) fourth-order Arakawa finite-differencing (Arakawa, 1966)

(c) truncated Fourier finite spectral.

The fourth-order Arakawa scheme is a higher order generalization of the more popular second-order differencing, and may be expected to be more accurate. The truncated Fourier-expansion method applied to (2.9) leads to

$$A(K,t+\Delta t) = A(K,t-\Delta t) - \begin{Bmatrix} 2ikU\Delta tA(k,t) & ; & \text{if} & |K\Delta x|<\pi \\ 0 & ; & \text{if} & K\Delta x = \pi \end{Bmatrix}$$

so that $\sin\theta = K\alpha\Delta x$. Each of these schemes, when applied to (2.9) using leapfrog time-differencing is neutrally stable for time steps chosen sufficiently small so as to satisfy the appropriate Courant condition. That is, the phase angle θ remains real if $|\alpha|\leq 1$ (in the Arakawa models) or $|\alpha|\leq\frac{1}{\pi}$ in the truncated Fourier spectral model. Table 2.1 displays δ (equivalently, the relative phase error) tabulated versus $K\Delta x$ for the particular choice $\alpha=0.1$, for each of these methods.

Table 2.1

Phase errors for $\alpha = 0.1$

$K\Delta x$	Second-order Arakawa scheme	Fourth-order Arakawa scheme	Truncated Fourier Spectral scheme
$\pi/12$	0.989	1.000	1.000
$\pi/6$	0.955	0.998	1.000
$\pi/4$	0.901	0.989	1.001
$\pi/3$	0.828	0.966	1.002
$\pi/2$	0.637	0.851	1.004
$2\pi/3$	0.414	0.622	1.007

The values of δ listed in Table 2.1 show that the fourth-order scheme has smaller phase errors than the second-order scheme, and that the truncated Fourier scheme has phase errors of less than 1% for all waves satisfying $|K\Delta x| < \frac{2\pi}{3}$, when $\alpha=0.1$.

It should be noticed that the second-order scheme has lagging phase error ($\delta<1$), while the fourth-order scheme has mostly lagging errors. [There is a region of leading phase error $\delta>1$ for very small $K\Delta x$ for the fourth-order scheme]. The lagging phase errors provide an explanation for the wakes of bad numbers given by finite-difference approximations (see also the discussion in Chapter 6).

The truncated Fourier scheme has only leading phase errors for finite Δt, and even these disappear in the limit $\Delta t \to 0$, if $K\Delta x < \pi$. As discussed in Chapter 3, the latter property is intimately related to the fact that this method has spatial errors that decrease more rapidly than any finite power of Δx as $\Delta x \to 0$ (if the exact solution that is being approximated is infinitely differentiable). Finite-difference approximations have non-zero phase errors in the limit $\Delta t \to 0$.

2.1.2 Second-differencing phase errors

These errors are introduced in evaluating the Laplacian operator ∇^2 by the standard finite-difference operation

$$(2.13)\quad (\nabla^2 A)_{x_\ell, y_m} \approx \frac{A(x_{\ell+1}, y_m) + A(x_{\ell-1}, y_m) + A(x_\ell, y_{m-1}) + A(x_\ell, y_{m+1})}{\Delta x^2} .$$

Consider the two-dimensional sinusoid $A(x,y) = e^{i(k_1 x + k_2 y)}$. Then the ratio of the approximate expression (2.13) to the exact result $-(k_1^2 + k_2^2)$ is just

$$(2.14) \qquad \frac{4}{\Delta x^2} \, \frac{\sin^2(\frac{k_1 \Delta x}{2}) + \sin^2(\frac{k_2 \Delta x}{2})}{k_1^2 + k_2^2}$$

which approaches unity only in the limit $k_1 \Delta x \to 0$ and $k_2 \Delta x \to 0$. Note again that for large k_1 or k_2 the second-order finite difference scheme seriously misrepresents the Laplacian operator as, for example, in the evaluation of the viscous term $\nu \nabla^2 V$. Reduction of these errors is possible by use of a fourth-order finite-difference approximation to $\nabla^2 V$, due to the higher order of approximation, but little benefit is gained.

There are no second-differencing errors in the truncated-Fourier expansion method, as the transform of $\nu \nabla^2 \underline{V}$ is exactly $-\nu k^2 \underline{U}(\underline{k})$. The algebraic form $-\nu k^2 \underline{U}(\underline{k})$ makes it a simple matter to treat viscous dissipation implicitly in time in the Fourier method. However, this advantage is slight, because in fully turbulent flows, it is the advective terms which are most important, and the numerical simulations are thereby usually limited by advective rather than diffusive stability criteria.

It should be noted here that, for systems where the pressure field (or the streamfunction field) is recovered diagnostically by solution of a Poisson equation (cf. (2.3b) or (2.5b), for example), the second-differencing phase errors associated with the representations of the Laplacian of these fields are considerably more detrimental to the evolution of the system than those introduced into the viscous terms.

2.1.3 Incompressibility Errors

The imposition of the incompressibility condition is a troublesome problem in many finite-difference schemes and computationally expensive iterative procedures are often required to maintain incompressibility to within a specified precision. Incompressibility can be imposed exactly in a truncated Fourier scheme by the following simple procedure.

Suppose that the three-dimensional velocity field is represented in Fourier space by $\underline{U}(\underline{k})$, where $\underline{U}(\underline{k})$ is the three-dimensional Fourier transform of the real-space velocity field $\underline{V}(\underline{x})$. The divergence of $\underline{U}(\underline{k})$ is given in Fourier space by $\mathbf{ik}\cdot\underline{U}(\underline{k})$. Let us subtract out vectorially the divergent component of $\underline{U}(\underline{k})$ by replacing $\underline{U}(\underline{k})$ with

$$\underline{U}'(\underline{k}) = \underline{U}(\underline{k}) - \frac{\underline{k}(\underline{k}\cdot\underline{U}(k))}{\underline{k}\cdot\underline{k}} . \tag{2.5}$$

Note that if we now take the divergence of this entire expression (that is, by performing the operation $i\underline{k}\cdot$ upon both terms, we get the identity

$$i\underline{k}\cdot\underline{U}'(\underline{k}) = i\underline{k}\cdot\underline{U}(k) - \frac{i(\underline{k}\cdot\underline{k})(\underline{k}\cdot\underline{U}(k))}{(\underline{k}\cdot\underline{k})} = 0 .$$

Hence, incompressibility is maintained exactly if, at the conclusion of each time step, we replace $\underline{U}(\underline{k})$ by $\underline{U}'(\underline{k})$. We have thus removed the divergent component of the velocity field. (Note how trivially such a constraint can be imposed in the Fourier spectral scheme). What is truly remarkable about this method is that, if the Navier-Stokes equations are written in rotational form, i.e.

$$(2.16)\qquad \frac{\partial}{\partial t}\,\underline{V}(x,t) = \underline{V}(\underline{x},t)\times\underline{\omega}(\underline{x},t) - \nabla\left(P + \frac{1}{2}\,\underline{V}\cdot\underline{V}\right) + \nu\nabla^2\underline{V}(x,t)$$

where $\underline{\omega} = \nabla\times\underline{V}$ is the vorticity, then this system may be evolved in time without any reference to the pressure head term, $\nabla(P+\frac{1}{2}\,\underline{V}\cdot\underline{V})$ so long as incompressibility is imposed at each time step in the manner indicated above. This is because, in an incompressible system, the pressure field serves only to enforce incompressibility, by dynamic readjustment of the velocity fields.

2.1.4 Coupling errors

Among the crucial difficulties with finite-difference approaches are the coupling errors introduced when non-linear differential operators are represented. Consider again for example the simple two-dimensional barotropic vorticity equation;

$$(2.17)\qquad \frac{\partial}{\partial t}\,\nabla^2\psi = -\underline{V}\cdot\nabla(\nabla^2\psi)$$

$$\underline{V} = \hat{k}\times\nabla\psi$$

where ψ is the geostrophic streamfunction. If we represent the Fourier transform of $\psi(\underline{x})$ by $\phi(\underline{k})$ as defined in Appendix 2, then it can be shown (Lilly 1965) that the wave-space version of (2.17) is just

$$(2.18)\qquad \frac{\partial}{\partial t}\{\underline{k}\cdot\underline{k}\phi(\underline{k})\} = \frac{1}{2}\int_{\underline{k}'+\underline{k}''=\underline{k}} |\underline{k}'\times\underline{k}''|\,(\underline{k}''\cdot\underline{k}'' - \underline{k}'\cdot\underline{k}')\phi(\underline{k}')\phi(\underline{k}'')\,d\underline{k}\,.$$

For the continuous system, the interaction between components with wavenumbers $\underline{k}'$ and $\underline{k}''$ must vanish identically if either $\underline{k}'$ is parallel to $\underline{k}$ or $|\underline{k}'| = |\underline{k}''|$. However, the Arakawa J_1

algorithm leads instead to a non-vanishing, spurious coupling in this case (Lilly, op.cit.). (Other finite-difference schemes lead to different spurious coupling relationships.) Moreover, the misrepresentation of spectral interactions occurs everywhere throughout the spectral range, and cannot be surmounted by ignoring a particular subrange, as discussed below.

2.1.5 Aliasing

Another fundamental difficulty with finite-difference techniques is "aliasing" associated with a finite grid interval. The phenomenon of aliasing is intrinsic to the representation of non-linear interactions defined over a discrete physical-space grid. It can be illustrated in the following simple manner. Consider the spatial interval of length L, over which is defined an N-point discrete grid x_j , $x_j = j\Delta x$, $j=1, \ldots N$ $(L=N\Delta x)$ Let us now represent the discrete analogues of the fundamental sinusoid $f(x) = \sin \frac{2\pi x}{L}$, and the first two harmonics $g(x) = \sin \frac{4\pi x}{L}$ and $h(x) = \sin \frac{6\pi x}{L}$. The discrete version of the fundamental sinusoid, defined over this grid, is just $f_d(x_j) = \sin \frac{2\pi j}{N}$ and in like manner $g_d(x_j) = \sin \frac{4\pi j}{N}$; $h_d(x_j) = \sin \frac{6\pi j}{N}$. Consider now the discrete-grid representation of the two product fields

$$P(x) = f(x)g(x) = \frac{1}{2}(\cos \frac{2\pi x}{L} - \cos \frac{6\pi x}{L})$$

$$Q(x) = g(x)h(x) = \frac{1}{2}(\cos \frac{2\pi x}{L} - \cos \frac{10\pi x}{L})$$

We might then suppose that

$$P_d(x_j) = \frac{1}{2}(\cos \frac{2\pi j}{N} - \cos \frac{6\pi j}{N})$$

and that

$$Q_d(x_j) = \frac{1}{2}(\cos\frac{2\pi j}{N} - \cos\frac{10\pi j}{N}).$$

To make matters concrete, choose $N=8$. If we were to tabulate $P_d(x)$ and $Q_d(x)$, we would find them to be numerically identical over the discrete-grid $j=1, \ldots 8$, whereas the continuous-space functions certainly differ with regard to the terms $\cos\frac{6\pi x}{L}$, $\cos\frac{10\pi x}{L}$. What has occurred? Trivially, of course, we have imposed an identity, since, for $N=8$, $\cos\frac{6\pi j}{N} = \cos\frac{10\pi j}{N}$. But the physical consequence of this little example is that, over a discrete grid of length eight points, the sixth harmonic of the fundamental spatial waveform is indistinguishable from the second spatial harmonic, and that, in fact, the information contained in the sixth harmonic, if it occurs as a result of non-linear interaction among, say, two lower modes, would be misrepresented by, or aliased down upon, the second harmonic. In like manner, the seventh harmonic would appear aliased as the first harmonic, and so on. We have illustrated the notion of a "folding" frequency (the Nyquist frequency N/2) associated with a discrete spatial grid of finite length N points.

Let us examine the aliasing problem in more formal mathematical manner. The values of the arbitrary functions $f(x)$, $g(x)$ at N equally spaced grid points $x_n = \frac{2\pi n}{N}$ $(n=0, 1, \ldots N-1)$ may be expanded in the discrete Fourier series

$$f(x_n) = f_n = \sum_{|k|\leq K} U(k)e^{ikx_n} \tag{2.19}$$

$$g(x_n) = g_n = \sum_{|k|\leq K} V(k)e^{ikx_n}$$

where k is an integer satisfying $-K \leq k < K$ with $N=2K$, or $-K \leq k \leq K$ with $N=2K+1$. The product function $h(x)=f(x)g(x)$ has the value $h_n = f_n g_n$ at x_n and the expansion

$$(2.20) \qquad h_n = \sum_{|k| \leq K} W(k) e^{ikx_n} \qquad (n=0, \ldots N-1)$$

where

$$(2.21) \qquad W(k) = \sum_{\substack{p+q=K \\ |p|,|q| \leq K}} U(p)V(q) + \sum_{\substack{p+q=K+N \\ |p|,|q| \leq K}} U(p)V(q) + \sum_{\substack{p+q=K-N \\ |p|,|q| \leq K}} U(p)V(q) .$$

The last two terms arise because $\exp(ik'x_n) = \exp(ikx_n)$ for all $n=0, \ldots, N-1$ if $k'=k$ (modulo N).

Aliasing is usually explained by noting that $f(x)$, $g(x)$, $h(x)$ have the exact Fourier expansions

$$(f(x), g(x), h(x)) = \sum (\overline{U}(k), \overline{V}(k), \overline{W}(k)) e^{ikx}$$

where the sum is taken over all integers k, $0 \leq x < 2\pi$, and

$$(2.22) \qquad \overline{W}(k) = \sum_{p+q=K} \overline{U}(p) \overline{V}(q) .$$

(It should be noted that $\overline{U}$, $\overline{V}$, $\overline{W}$ are, in general, not equal to U, V, W, respectively.) It is apparent from (2.22) that the exact $\overline{W}(k)$ includes no counterpart of the last two terms in the expression (2.21) for $W(k)$. The false interactions included in the last two terms in (2.21) are called aliasing interactions; $k+N$ and $k-N$ are aliases of k on the discrete grid x_n, since $e^{i(k+N)x_n} = e^{ikx_n}$ for $n=0, \ldots, N-1$. A finite-difference approximation to the Navier-Stokes equations may lead to difficulty, because of aliasing errors in the discrete-grid approximation of the (scalar) product $\underline{v} \cdot \nabla \underline{v}$. Phillips (1959) gives a simple example where aliasing terms in the representation of a product induce an instability not present without aliasing. This aliasing property of finite-difference representations has several other consequences in the numerical simulation of non-linear fluid flows. We must recognize, first, that the physical process of non-linear turbulent spectral cascade of energy (or vorticity) to small scales is falsified, inasmuch as the folding frequency acts, inthe absense of dissipation, as a reflective boundary in wavespace. That is, since no modes above the Nyquist frequency exist to receive energy, the energy transferred by non-linear interaction must be redistributed among the available modes which lie below the Nyquist cutoff, in order that energy remain a conservative quantity. [This is true, as well, of vorticity, or enstrophy]. Accordingly, it might suggest itself to ignore the small-scale structure, in the expectation that the largest scales are at least adequately represented. But, in fact, all the scales of the system are contaminated by downward-aliased spectral information.

One may ask, therefore, why conventional finite-difference methods are reasonably successful for certain classes of geophysical fluid flow simulations, most notably, for example, in large-scale operational numerical weather prediction. The answer is rather subtle, and concerns the spectral structure of the flow fields being simulated. If the spectrum falls off sufficiently rapidly with increasing wavenumber, then the aliasing-induced contamination of the lowest modes, while present, may be so small as to be ignorable.

It is precisely this property of large, geostrophic-scale atmospheric flow systems (which seem to follow minus-third or minus-fourth spectral power laws) that permits physically credible numerical weather forecasts on these scales. In general, however, the spectral power law of the simulated physical system does not fall off with sufficient rapidity, so as to permit the ignoring of aliasing contaminations. For such problems, therefore, it is especially important that the numerical technique employed can eliminate aliasing errors or strongly limit their extent, if such errors are deemed important. Appendix 3 presents the method developed by Orszag for efficient alias-free multiplication of fields defined over discrete spatial grids.

2.1.6 Treatment of Singularities and Local Discontinuities

Among the most troublesome problems encountered in numerical flow simulation is the treatment of flow structures with singularities and local discontinuities embedded in such flows, as for example, point sources of pollution. Eulerian finite-difference methods permit the numerical evolution of strongly discontinuous flows, but only at the cost of smearing out, or smoothing over, these discontinuities, often in an entirely unrealistic manner. These effects have been demonstrated by Orszag (1971b), who compared second and fourth order finite-difference methods with truncated spectral methods, for the problem of the two-dimensional advection of a passive scalar field, whose initial distribution is circular (hence referred to as a scalar "cone"), by a uniform rotation velocity field. (An extension of this study to viscous flows is included in Chapter 5 of the present report.) One of the most remarkable features of the truncated spectral method that is demonstrated by this problem is the result that the cone is better localized in space, using these truncated spectral representations, than by finite-difference schemes formulated directly in physical space. That is, the cone location is preserved more accurately by expanding the initial excitation in discrete Fourier series, permitting these Fourier coefficients to evolve in time in accordance with the spectral form of the governing dynamical equations, and finally, reconstructing the discrete real-space field from the Fourier coefficients, than by a direct evolution of the real-space field using a finite-difference method. In other words, flow structure with intermittencies in physical space seem to be more accurately followed in terms of their Fourier components than directly in physical space. To explain this rather counter-intuitive result, we discuss in Appendix 1 the data content of discrete real-space representations of continuous spatial functions. The principal consequence, in the present context, is that spectral representations (as by Fourier expansions), allows much better interpolation between discrete real-space grid points than is permitted by the structural data preserved by the local grid-point values alone. That is, the global information preserved in the spectral decomposition of a spatial function permits more precise reconstruction of local details than does the grid-point decomposition of corresponding resolution. This may be better understood by reference to the previous discussion of the phase and aliasing errors which underlie finite-difference methods; in particular the point made that finite-difference schemes have mostly lagging phase errors, so that some of the data needed to reconstruct a spatially local disturbance at a given instant in time is erroneously phase-lagged and so is as yet unavailable at the appropriate local spatial region.

3.0 Spectral Methods

The utility of spectral transformations in the analytic solution of many partial differential equations of classical physics has been long recognized. It is only relatively recently, however, that advances in available computational power and algorithmic breakthroughs have made possible the wide use of numerical spectral methods for the solution of PDE's, in particular, for the solution of a variety of geophysical and other fluid flow problems.

The essential principles which govern the use of spectral methods in numerical simulations may be stated quite simply; instead of solving multidimensional finite-difference equations, one applies semianalytic methods in which the dependence of the flow on one or more independent variables (generally, but not exclusively, the spatial dimensions) is expanded into a series of smooth, and usually orthogonal, functions. The potential choice of orthogonal expansion functions is quite broad; e.g., Fourier, Chebyshev, Lengendre, and Hermite series, among others, are possible candidates in various different flow problems. The specific choice made depends upon the following kind of considerations:

(a) the nature of the boundary conditions to be imposed, and the suitability of the expansion functions chosen in regard to the imposition of these boundary conditions;

(b) the ease with which the governing differential equation can be formulated and numerically evolved with time, in terms of the expansion functions;

(c) the relative computational effort involved in the numerical evaluation of the expansion coefficients;

(d) the accuracy achieved in the expansion, in particular, the rate of convergence of the expansion coefficients;

(e) the relative generalizability which a given class of orthogonal polynomials offers in a variety of flow problems.

A few simple examples will suffice to illustrate these points. For example, in flow in cylindrical geometries the velocity field must be periodic with respect to the zonal coordinate ϕ so that the dependence on ϕ is expandible in a Fourier series

$$\underline{V}(r,\phi, z,t) = \sum_{n=-\infty}^{\infty} \underline{U}_n(r,z,t)e^{in\phi} .$$

If this series is truncated to $|n|\leq N$ modes, we obtain a finite spectral representation that may be suitable for the generation of an approximation to $\underline{V}$. It is, of course, necessary to convert the Navier-Stokes equations into equations for $\underline{U}_n(r,z,t)$ $(|n|\leq N)$ and to discretize the spatial coordinates r and z, and the time t. It may also be appropriate to construct truncated series expansions for the function $\underline{V}$ in terms of polynomials defined over the variables r and z.

The questions of appropriateness of a series expansion for prescribed boundary conditions, rates of convergence, and generalizability can be made more precise by reference to the one-dimensional wave problem

(3.1) $$\frac{\partial U}{\partial t} + \frac{\partial U}{\partial x} = 0 \qquad (-1<x<1)$$

with the following mixed initial-boundary value conditions:

(3.2a) $$U(x,0) = 0$$

(3.2b) $$U(-1,t) = \sin m\pi t.$$

The exact solution is just

$$U(x,t) = 0; \quad (t\leq x+1)$$

$$= \sin m\pi(t-x-1); \quad (t>x+1).$$

(The index m designates the number of full wavelengths within the interval $|x|<1$).

Considering the spatial domain of the problem, it would seem, at first, most natural to attempt a Fourier series solution to this problem. For the particular choice of boundary conditions (expecially 3.2b) the exact solution is trigonometric in nature, and a Fourier series expansion might be expected to succeed well. But, with the more general boundary condition $U(-1,t)=f(t)$, say, the choice of Fourier series would be extremely disadvantageous, since the general boundary condition is not a natural boundary condition for a complete set of trigonometric functions, and the Gibbs phenomenon at $x=-1$ will force rather slow convergence of the Fourier series for U or its spatial derivatives.

Instead, it is most natural to expand $U(x,t)$ in series of orthogonal polynomials, whose convergence rate is governed by the smoothness of the solution, not by the special nature of

$$u(x) = \sum_{n=0}^{\infty} A_n T_n(x) \tag{3.3}$$

$$A_n = O(n^{-(p+1)}). \tag{3.4}$$

In particular, if $u(x)$ is infinitely differentiable, then the Chebyshev coefficients go to zero faster than any finite power of $1/n$; we say that the approximation obtained by truncating (3.4) at N terms is of infinite order, since the error goes to zero faster than any finite power of $1/N$. Also, the latter Chebyshev series may be differentiated termwise any number of times. Notice that the convergence rate of the expansions is governed by the smoothness of the function $u(x)$, irrespective of boundary conditions.

At present, there are three principal classes of discrete-spectral methods for the representation of continuous systems such as (3.1). These are the Galerkin approach (Collatz, 1960), the tau method (Lanczos, 1956), and the collocation method (Collatz, 1960, Lanczos 1956). The three methods can be usefully compared in regard to equations (3.1-3.2). The Galerkin methods employ a new dependent variable $v(x,t)=u(x,t)-\sin m\pi t$, so that $v(x,t)$ satisfies the homogeneous boundary condition $v(-1,t)=0$ and the inhomogeneous wave equations, and equations for the time-dependent coefficients are obtained by requiring that an appropriate inner product of the dynamical equation (3.1) with each of the retained $T_n(x)$ be zero. When rewritten in terms of $u(x,t)$, the semidiscrete Chebyshev-Galerkin equations become (Orszag 1971d)

$$u(x,t) = \sum_{n=0}^{N} a_n(t)T_n(x) \tag{3.5}$$

$$c_n \frac{da_n}{dt} = -2 \sum_{\substack{p=n+1 \\ p+n=\text{odd}}}^{N} pa_p + (-1)^n b(t) \qquad (0 \le n \le N) \tag{3.6}$$

$$\sum_{n=0}^{N} (-1)^n a_n(t) = \sin m\pi t \tag{3.7}$$

where $c_o=2$, $c_n=1$, $(n \geq 1)$. Here $b(t)$ is a "boundary" term that is determined by compliance with (3.7).

The tau method is based on using the finite expansion (3.5) to solve exactly the approximate differential equation $u_t+u_x = \tau_n(t)T_n(x)$. The resulting equations for $a_n(t)$ are precisely (3.6) and (3.7) but with the boundary term $b(t)$ set to zero for $n=0, \ldots, N-1$ and $b(t) = \tau_N(t)$ for $n=N$.

Finally, collocation uses the spectral representation (3.5) to interpolate values of $u(x,t)$ at $(N+1)$ "selected points" $x_p (p=0, \ldots, N)$. With Chebyshev polynomials, it is most natural to choose $x_p=\cos \pi p/N$, so that (3.5) is just a discrete Fourier transform. The polynomial interpolation (3.5) is used merely to evaluate $\partial u/\partial x$ at the points x_p by termwise differentiation. In terms of a_n, collocation gives (Orszag 1972) equations (3.5-3.7) with $b(t)$ replaced by $b(t)/C_{N-n}$; the only change is in (3.6) for $n=N$ where $(-1)^N b(t)$ is replaced by $1/2(-1)^N b(t)$. Collocation (called pseudospectral approximation in a later section) is particularly convenient when there are nonconstant coefficients or nonlinear terms. In these latter cases, pseudospectral approximation is quite different from, and much simpler than, spectral (Galerkin or tau) approximation because of the appearance of aliasing terms in pseudospectral approximation.

Notice that solution of 3.6, 3.7 requires only $O(N)$ arithmetic operations per time step if care is taken to accumulate required sums, and that the transformation (3.5) to the "physical space" $u(x,t)$ can be accomplished in $O(N \log N)$ operations when N is a power of 2, because (3.5) is just a Fourier cosine series for which fast Fourier transforms are applicable.

3.1 Boundary Conditions and Geometries

3.1.1 Periodic Boundary Conditions

Physical intuition leads us to expect that for planar geometries and/or periodic boundary conditions, the use of discrete Fourier series is appropriate. In this case, our intuition is indeed correct; finite Fourier series are the most natural and efficient expansion method.

3.1.2 Free-slip Boundary Conditions

Free-slip--free-slip boundary conditions such as

(a) $U_z=V_z=0 \qquad z=0,\pi$

(b) $W=0 \qquad z=0,\pi$

are mathematically equivalent to symmetry boundary conditions, inasmuch as conditions (a) are most naturally implemented in cosine series and conditions (b) in sine series representations of (U,V), and W respectively. Hence Fourier-series expansions are the appropriate choice for free-slip--free-slip boundaries. For mixed free-slip--no-slip conditions, the use of Fourier series would, in general, be ill-advised.

3.1.3 No-Slip Boundary Conditions

By contrast with free-slip conditions, no-slip boundary conditions impose stringent constraints upon the dynamical fields, which, in general do not lend themselves readily to computationally efficient or accurate implementation in Fourier-series expansion due to Gibbs phenomena at the boundaries. Rather, as has been demonstrated by Orszag (1972) Chebyshev expansion is the technique of choice, principally because the rate of convergence of such an expansion can be specified a priori, without reference to the boundary conditions, and because Chebyshev methods are efficiently implemented by skillful use of Fast Fourier (cosine) transforms. Chebyshev series are not restricted to planar geometries; they may profitably be applied, for example, to handle the radial expansion in flows in cylindrical or spherical geometries, or in any geometry that can be smoothly mapped, by convenient transformation, into either rectangular or circular domains. Metcalfe (1973) has employed Chebyshev expansions in the analysis of a variety of viscous incompressible flows in various cylindrical and spherical geometries.

3.1.4 Inflow and Outflow Boundary Conditions

Spectral methods are capable of high-order accuracy at inflow and outflow boundaries, for example, as in a limited forecast area model (LFM), without the need for special methods to impose the boundary conditions. By contrast, high-order finite-difference methods deteriorate, or may break down completely, near boundaries because grid points outside the physical domain must be invoked. The necessary modifications to maintain accuracy near the boundary can get quite complicated (Kreiss and Oliger 1973).

3.2 Treatment of Boundary Layers

Among the most valuable properties of Galerkin methods using Chebyshev expansions, is the much greater fidelity with which boundary layer structure can be resolved using Chebyshev expansions, compared to a conventional finite-difference representation with comparable number of grid intervals. This follows naturally from the definition of the Chebyshev polynomials, namely:

$$T_n(\theta) = \cos n\,\theta, \quad 0 \leq \theta \leq \pi \ . \tag{3.8}$$

If we perform the mapping $z=\cos\theta$, then the real-space function $f(z)$ has the Chebyshev expansion

$$f(z) = \sum_{n=0}^{\infty} a_n T_n(\cos^{-1} z) \qquad -1 \leq z \leq 1 \quad . \tag{3.9}$$

The discretized form of this relationship, defined over the real-space grid

$$Z_j = j\Delta z \qquad (j=0, \ldots N)$$

is just

$$f_j = \sum_{n=0}^{N} a_n \cos\frac{n\pi j}{N} = \sum_{n=0}^{N} a_n T_n(\cos\theta_j); \ \theta_j = \frac{\pi j}{N} \ . \tag{3.10}$$

Since $Z_j = \cos\frac{\pi j}{N}$, a uniform partition over the angular range $\theta=[0,\pi]$ corresponds to a non-uniform mesh over $z=[-1,1]$, with substantially more resolution in the vicinity of the boundaries than within the interior. For example, for $N=16$, we may tabulate

j	θ_j	$z_j = \cos \theta_j$
0	0	1.0000
1	$\pi/16$	.98079
2	$\pi/8$	.92308
3	$3\pi/16$	.83147
.	.	.
.	.	.
.	.	.
7	$7\pi/16$	.19509
8	$\pi/2$	.00000
.	.	.
.	.	.
.	.	.

The physical significance, of course, is that, near the boundaries, where viscous phenomena are most important, we can allow for greater resolution of the boundary layer structure than would be achievable by the equivalent uniform grid $\Delta z = 0.125$. This permits us to resolve more of the viscous boundary layer structure (the extent depending, of course, upon the boundary layer thickness, $\delta \sim 1/\sqrt{\nu}$, and the number of Chebyshev modes retained). As previously suggested, a striking characteristic of Chebyshev expansions, is the rapidity with which the series converges (faster than any power of $1/N$). Let us put the boundary layer question, and the related matter of convergence, in clear perspective by examining the following simple diffusion problem, i.e., a laminar flow with a viscous boundary layer:

$$(3.11) \qquad \frac{\partial U}{\partial t} = \frac{\nu \partial^2 U}{\partial z^2} \; .$$

Differencing forward in time, and treating the viscous term implicitly, we get:

$$(3.12) \qquad \gamma \frac{\partial^2}{\partial z^2} U^{p+1} - U^{p+1} = - U^p \qquad (\gamma=\nu\Delta t,\ t_p=p\Delta t)$$

Using the discrete Chebyshev transformation (3.10), equation (3.12) may be written as

$$(3.13) \qquad \gamma b_n - \hat{a}_n = - a_n \qquad 0\le n\le N-2$$

where a_n designates the n^{th} Chebyshev mode of U^p, $\hat{a}_n$ is the n^{th} Chebyshev mode of U^{p+1}, and b_n designates the n^{th} Chebyshev mode of $\frac{\partial^2 U^{p+1}}{\partial z^2}$, and N represents the highest Chebyshev mode retained. From the definition of Chebyshev differentiation, and the properties of the Chebyshev polynomials, we also have the following set of relationships between b_n and a_n

$$(3.14) \qquad \hat{a}_n = \frac{c_{n-2}b_{n-2}}{4n(n-1)} - \frac{e_{n+2}b_n}{2(n^2-1)} + \frac{e_{n+4}b_{n+2}}{4n(n+1)} \qquad (2\le n\le N-2)$$

$$\text{where } c_n = \begin{Bmatrix} 0, & n<0 \\ 2, & n=0 \\ 1, & n>0 \end{Bmatrix} \quad , \quad e_n = \begin{Bmatrix} 1, & n\le N \\ 0, & n>N \end{Bmatrix} .$$

In particular, for $n=N-2$, we have

$$(3.15) \qquad b_{N-2} = 4N(N-1)\hat{a}_N .$$

Substituting (3.13) and (3.15) into (3.14) we may eliminate the terms b_n, and obtain a linear tridiagonal matrix system of the form

$$\mathcal{L}\underline{\hat{a}} = -\underline{a}$$

where $\underline{\hat{a}}$ is the vector $\begin{Bmatrix} \hat{a}_0 \\ \hat{a}_1 \\ \vdots \\ \hat{a}_N \end{Bmatrix}$, $\underline{a}$ is the vector $\begin{Bmatrix} a_0 \\ a_1 \\ \vdots \\ a_N \end{Bmatrix}$.

This system may be inverted by any of a number of standard matrix inversion algorithms, the standard LUD algorithm being especially useful.

Suppose $U^p(z)$ is of the form $1 - \frac{\cos 2\theta}{2}$ $(z = \cos^{-1}\theta)$. Then the only non-zero modes in the Chebyshev representation of this function are $a_0 = 1$, and $a_2 = -1/2$.

Let us now compare the Chebyshev solutions to (3.12) (using (3.13) - (3.15)) as we vary parameters γ and N, the number of retained modes. As before we designate the Chebyshev modes of U^p by a_n $(n=0, \ldots, N)$, and the modes of U^{p+1} will be designated by $\hat{a}_n$:

Case 1: $\gamma = 10^{-3}$		$\hat{a}_n$		a_n
	N=8	N=16	N=32	
n=0	.9385	.927039	.927056	1.0000
2	-.6093	-.63308	-.63306	-.5000
4	-.0827	-.10976	-.10976	0
6	-.0451	-.07966	-.07971	.
8	-.2013	-.05092	-.05102	.
10		-.02863	-.02885	.
12		-.01398	-.01443	.

	N=8	N=16	N=32
14		-.00538	-.00641
16		-.00561	-.00253
18			-8.9×10^{-4}
20			-2.8×10^{-4}
22			-8.0×10^{-5}
24			-2.0×10^{-5}
26			-4.7×10^{-6}
28			-9.8×10^{-7}
30			-1.8×10^{-7}
32			-4.6×10^{-8}

Note that for N=8 retained modes, no convergence ($a_n \to 0$ for $n \to \infty$) is apparent. In the case N=16, there is just marginal convergence, but for N=32 modes the convergence is extremely strong. This indicates that there is just marginally enough resolution, using 16 modes, to resolve the boundary layer whose characteristic thickness is $\delta \sim \frac{1}{\sqrt{\nu}} \sim .03$, but that merely by doubling the number of modes, the resolution is about as perfect as we could ever hope to achieve (another doubling would give no better resolution).

Case 2: $\gamma = 10^{-2}$

	$\hat{a}_n$		
	N=8	N=16	N=32
n=0	.857279	.857280	same as N=16
2	-.698663	-.698875	"
4	-.106009	-.106911	"
6	-.036378	-.0391647	"
8	-.016238	-.0101173	"

	N=8	N=16	N=32
10		$-.00190785$	$-.00190785$
12		$-2.71303\ \mathrm{x}10^{-4}$	$-2.71333\ \mathrm{x}10^{-4}$
14		$-2.966\ \mathrm{x}10^{-5}$	$-2.991\ \mathrm{x}10^{-5}$
16		$\underline{-3.089\ \mathrm{x}10^{-6}}$	$-2.619\ \mathrm{x}10^{-6}$
18			$-1.86\ \mathrm{x}10^{-7}$
20			$-1.09\ \mathrm{x}10^{-8}$
22			$-5\ \mathrm{x}10^{-10}$
24			$-2\ \mathrm{x}10^{-11}$
26			$-5\ \mathrm{x}10^{-13}$
28			$-2\ \mathrm{x}10^{-14}$
30			$-6\ \mathrm{x}10^{-16}$
32			$-2\ \mathrm{x}10^{-17}$

In this case, for the characteristic boundary layer thickness $\delta \sim .1$, N=8 modes is just marginally adequate, while 16 modes already displays rapid convergence, and an additional doubling gives essentially nothing more.

Orszag has found an approximate rule which relates the boundary layer thickness implicit in the computation, to the number of modes just necessary to adequately resolve such a layer:

$$N_{CRIT} \sim 3\delta^{-1/2}.$$

Note that for Case 1, $N_{CRIT} \sim 16.8$, and for Case 2, $N_{CRIT} \sim 9.5$, which is entirely consistent with the results shown.

Stated in more familiar terms, the number of Chebyshev modes required for an accurate spectral simulation of a laminar flow with a viscous boundary layer increases only as $R^{1/4}$ (where

R is the Reynolds number of the flow), whereas the resolution requirement of a finite difference model varies as $R^{1/2}$.(1) For the high Reynolds numbers characteristic of realistic meteorological flow problems, the computer storage advantage of Chebyshev methods is enormous. Such methods thus offer the potential of extremely accurate numerical simulation of boundary layer structure.

If, in conjunction with these Chebyshev methods, appropriate coordinate-stretching techniques (Israeli 1971, Ph.D. Thesis) are employed to assist in the resolution of a boundary layer of thickness δ, then the spectral errors are decreased faster than any finite power of δ as $\delta \to 0$, whereas the errors in finite difference methods, due to such coordinate transformations, decrease by finite power of δ.

3.3 Pseudospectral Methods

Our emphasis thus far has been focused upon the purely spectral (Galerkin) methods. We have seen that, within limitations imposed by geometry and boundary conditions, these methods are very powerful. We have suggested also that Galerkin methods are relatively easy to implement for certain important classes of non-linear interactions, as for example the rotational term $V \times \omega$ in the Navier-Stokes equations. The accuracy with which phase information is preserved, and with which aliasing can be controlled, has been discussed and the elimination of aliasing is described in detail in Appendix 3.

---

(1) in a finite-difference representation of νU_{zz}, say $\frac{\nu}{\Delta_z^2}(U_{j+1} - 2U_j + U_{j-1})$ it is evident that Δz must vary with $N^{-1/2}$, or equivalently with $R^{1/2}$.

However, there are many cases of interest for which aliasing errors can be expected to be small, and/or tolerable, and we would not wish to pay the computational price required to eliminate aliasing in such cases. Secondly, it is sometimes necessary to evaluate highly non-linear terms within a spectral framework, and such terms would be extremely difficult to formulate directly in wavespace. Thirdly, if we wish to represent physical processes that are local in real space (such as, for example, the onset of condensation in a numerical model of cloud dynamics) such a local-space condition would be extremely awkward to formulate in a Galerkin framework because a single point in real space is represented in wavespace as a superposition of many modes, and a product term in real space corresponds to a convolution sum in wavespace. Accordingly, Orszag has introduced a modified Galerkin-like approach, which he has termed "pseudospectral." This approach is computationally very economical, retains much of the power of the purely spectral Galerkin method, yet permits us to handle more general non-linear terms, complicated boundary conditions, and processes which are local in real space. The idea behind the pseudospectral method is to represent certain terms in physical space when it would be computationally prohibitive to do so spectrally, but to switch back to wavespace when it is very important, and computationally easy, to preserve accurate phase and amplitude information.

Consider, for example, the temperature equation written in an incompressible Boussinesq system

$$\frac{g}{T_{00}} \frac{\partial T}{\partial t} = - \frac{g}{T_{00}} \nabla \cdot (\underline{V}\ T) - N^2(z) W + \frac{g}{T_{00}} \kappa \nabla^2 T \tag{3.16}$$

where T is the variable temperature field, T_{00} is a standard reference temperature, $\underline{V}$ is the three-dimensional velocity vector, W is the vertical velocity component, $N(z)$ is the Brunt-Vaisala frequency, which depends upon altitude z, g is the acceleration of gravity, κ is the (constant) thermal diffusion coefficient. An appropriate pseudospectral procedure for evaluation of the right hand side might be as follows:

(a_1) Represent each component of $\underline{V}$, and the temperature field T, in real space, and form the vector quantity $(\underline{V}T)$ at each physical grid point, that is

$$\underline{V}T = U(x,y,z)T(x,y,z)\hat{i} + V(x,y,z)T(x,y,z)\hat{j} + W(x,y,z)T(x,y,z)\hat{k};$$

(a_2) transform the vector quantity $(\underline{V}T)$ to a vector term in wavespace, denoted by $(\widetilde{\underline{V}T})$.

(a_3) Evaluate the divergence of the quantity directly in wavespace by multiplying by the wavespace divergence operator $i\underline{k}\cdot$ (where $\underline{k}$ is the wave vector); this has the virtue of preserving the exact phase relationships in the divergence expression, without the first-differencing errors introduced by a finite-difference approximation to the divergence term in real space.

(b) Assuming an explicit evaluation of the thermal diffusion term is adequate, transform T to wavespace, denoting its transform by $\tilde{T}$, and evaluate the Laplacian term directly in wavespace by multiplying $\tilde{T}$ by the scalar operator $-\underline{k}\cdot\underline{k} = -k^2$. This procedure avoids the second-differencing errors associated with the finite-difference form of the Laplacian operator. [The diffusion term can be treated implicitly in a spectral formulation very simply, if, for example, (3.16) is written in the transformed form

$$\frac{g}{T_{00}}\left(\frac{\partial\tilde{T}}{\partial t} + \kappa k^2\tilde{T}\right) = -\frac{g}{T_{00}}\, i\underline{k}\cdot(\widetilde{\underline{V}T}) - \widetilde{(N^2(z)W)}, \tag{3.17}$$

where, as, before, the tilda (~) designates the wave-space transform of the real-space field.]

(c) Represent the vertical velocity W in real space, and at each point of the physical grid form the product $N^2(z)W$; then transform the expression $N^2(z)W$ to wavespace. By first evaluating the product in real space, we avoid a nasty convolution sum, but accept the inevitable aliasing penalty, which may not be a severe limitation, especially if the term is small or if N is a slowly varying function of z.

(d) Since each term on the right hand side of (3.16) is now available in its spectral form, we may evaluate each of the spectral components $\frac{\partial\tilde{T}}{\partial t}$. Finally, then, we inverse transform $\frac{\partial\tilde{T}}{\partial t}$ to real space to obtain the local rate of change of temperature.

Thus, the pseudospectral method makes effective use of finite spectral operations when it is convenient and/or crucial to do so, but returns to finite real space collocation operations when the equivalent spectral operation is computatively prohibitive, or aliasing errors are tolerable. A more elegant statement of the method, which has perhaps been adequately motivated by the example above, has been provided by Orszag (1971a). That is, the philosophy of the pseudospectral method is to calculate in either spectral or physical space according to whichever representation is more natural. In particular, one chooses a suitable orthogonal expansion as an interpolatory tool, in order to be able to differentiate without phase error. Derivatives are evaluated entirely by explicit multiplications in spectral space (rather than by finite differences in real space). Operations like differentiations in finite-difference schemes and convolutions in spectral schemes are avoided.

Let us apply the pseudospectral idea for efficient evaluation of the non-linear terms of the equations of motion. The principal error of finite-difference schemes is first-differencing or phase error (cf. section 2.1). These errors are avoided so long as spectral methods are used to compute derivatives. For example, $\partial v/\partial x$ at $x=x_j$, where $x_j=2\pi j/N$ $(j=1, \ldots, N)$, may be computed without phase error by first Fourier analyzing $v_j=v(x_j)$ into its discrete Fourier components $v(k)$ $(|k| \leq N/2)$ and then setting

$$(3.18) \qquad \left(\frac{\partial v}{\partial x}\right)_{x=x_j} = \sum_{|k| \leq \frac{N}{2}} ikv(k)e^{ikx_j} .$$

A term like $v\partial v/\partial x$ in an equation of motion can then be evaluated at the grid point x_j as the local physical-space product of $v(x_j)$ with $(\partial v/\partial x)_{x=x_j}$. If derivatives are computed in this manner, the resulting scheme is not subject to phase error, but it is "fully aliased" in the sense that spectral terms modulo $\pm 2k$ appear in the spectral analysis of the scheme (see section 2.1.5).

If a pseudospectral approximation is made to the Navier-Stokes equations written in the form (2.2) by evaluating derivatives as in (3.18), the resulting fully-aliased equations may be subject to unconditional instability (Orszag, 1971b). However, if the Navier-Stokes equations are first expressed in rotation form

$$\frac{\partial}{\partial t} \underline{V}(\underline{x},t) = \underline{V}(\underline{x},t) \times \underline{\omega}(\underline{x},t) - \nabla P(\underline{x},t) + \nu\nabla^2\underline{V}(\underline{x},t) \tag{3.19}$$

where $P = p+u^2/2$ and $\underline{\omega} = \nabla \times \underline{v}$ is the vorticity, the pseudospectral approximation obtained by calculating in analogy to (3.18) (using local operations on the Fourier modes of v), is normally satisfactory. The reason is that the pseudospectral approximation to the rotation, rather than the advective form ($V\cdot\nabla V$) of the non-linear terms of the Navier-Stokes equations semi-conserves energy (i.e. conserves energy in the absense of time-differencing errors). Aliasing errors, although present, cannot directly cause unconditional non-linear instability. Pseudospectral approximation to (3.18) gives phase-error-free simulations that are a factor two more efficient than those obtained by the fully alias-free algorithm of Appendix 3, with the same wavenumber cutoff (Orszag, 1971b).

The pseudospectral method discussed here is basically the same as the "method of selected points" or "collocation" method, introduced by Lanczos (1956). The principal difference is the use of the fast Fourier transform to effect rapid transforms between spectral and physical space representations.

4.0 Applications of Numerical Spectral Methods

In this section we discuss briefly some of the principal areas of fluid research, relevant to meteorological problems, in which numerical spectral methods have been found especially fruitful, namely:

(a) the simulation of atmospheric dynamics;

(b) the simulation of turbulence and tests of turbulence theories;

(c) advective-diffusive modeling.

Recent years have witnessed an avalanche of papers concerning spectral simulations of various problems in atmospheric flows and numerical weather prediction. For example, Eliasen, et al. (1970), have considered spectral harmonic methods for integration of the primitive equations on the sphere; Merilees (1973, 1974) has described pseudospectral methods for such problems; Bourke (1972), Gordon and Stern (1974) have described experiments with multilevel baroclinic global general circulation models constructed in spectral manner. An especially important spectral model is the stratospheric dynamics model of the MIT group (Cunnold, et al. 1975) which incorporates elements of both the purely Galerkin and the pseudospectral approaches for the simulation of the dispersion of chemical pollutants in the upper atmosphere. Many of the recent advances in the field of atmospheric spectral modeling are described in the Copenhagen symposium volume (GARP, 1974), to which the reader's attention is directed.

The employment of spectral methods for direct numerical simulation of turbulent flows is of very recent origin. Spectral simulations of this sort, which require explicit retention of 1-3x10^4 modes, have become practical only with the introduction of efficient transform techniques (Orszag 1969, Patterson and Orszag 1971). Simulations have been performed for homogeneous two-dimensional turbulence (Herring,et al. 1974) and homogeneous isotropic three-dimensional turbulence (Orszag and Patterson 1972), at moderate Reynolds numbers. Extensions of these studies to inhomogeneous flows, turbulent wakes and jets, etc., are being actively pursued (Herring 1974, Orszag and Pao 1974).

It would not be appropriate here to attempt to review the salient conclusions regarding the structure of turbulence, and the validation of turbulence theories, which have emerged from such studies. One point, however, is certainly worth emphasizing here. That is, throughout the course of such spectral simulations, it has become empirically evident that the large-scale flow features exhibit a remarkable degree of Reynolds-number independence. As a consequence, it may not be necessary to simulate turbulence at the huge Reynolds numbers appropriate to the atmosphere, if our principal concern is with synoptic-scale features; that is, much valuable information can be obtained from simulations whose Reynolds numbers are such that all dynamically relevant scales of motion can be included explicitly in the computation, without recourse to closure arguments or subgrid-scale modeling. It appears that, once a certain critical Reynolds number is attained (and such Re_{crit} are remarkably low!) the large-scale features are sensibly independent of the detailed mechanisms by which energy (or enstrophy) are cascaded to the smallest scales, provided that the initial flow conditions are Reynolds-number independent.

Of more immediate importance, with regard to the improvement of air-quality simulation modeling efforts, are the insights which are emerging concerning the utility of spectral methods in the numerical simulation of advective-diffusive problems. In a pioneering effort, Orszag (1971b) considered the Crowley color problem (Crowley, 1968), namely the two-dimensional convection of a passive scalar field by a uniform rotation velocity. This problem has been considered as well by Molenkamp (1968), from the finite-difference point of view. Orszag compared solutions to this problem using second-order and fourth-order Arakawa finite-differencing schemes, and the Galerkin Fourier approach discussed before. He demonstrated that results obtained using the truncated Fourier-expansion scheme on a 32x32 space grid (cutoff wavenumber K=16) are at least as good as those obtained by the fourth-order scheme on a 64x64 grid, and significantly better than those obtained by the fourth-order scheme on a 32x32 grid, or by the second-order scheme on 32x32 and 96x96 grids. It appears that, for those problems for which the "color" problem and the Neuringer problem discussed in Chapter 5 are typical examples, second-order schemes require at least four times as many grid intervals in each spatial direction, and fourth-order schemes require at least two times as many grid intervals, as the truncated Fourier expansion scheme.

We have recently extended this study to incorporate diffusive terms. These new results are presented in Chapter 5 of this report. As will be seen, the conclusions which emerge support strongly the argument for the use of spectral techniques where feasible, especially in regard to high Reynolds number flow simulations.

5.0 A Comparison of Spectral and Finite Difference Methods for Two Examples

To date, little effort has been directed toward exploiting spectral techniques for numerical air-pollution simulations. This section illustrates some of the computational advantages of the spectral technique for the simulation of advective-diffusive problems, by reference to (a) a diffusive generalization of the Crowley "color" problem (Crowley 1968, Molenkamp 1968, Orszag 1971a), that is, the advection-diffusion of an instantaneous point-source scalar in a two-dimensional field of solid rotation; and (b) a problem proposed by Neuringer (Neuringer, 1968), concerning the advection-diffusion of a point source in a sheared wind field. We compare numerical solutions using the spectral (truncated Fourier) method with those using the conventional second-order finite-difference method. It is shown that, for simulations of comparable accuracy, the spectral method permits very substantial reductions in required core storage, and less computational time as well.

We also present a rebuttal to some criticisms offered in a private communication by Chan and Stuhmiller (denoted by C-S) to a preliminary version of these results.

5.1 Comparison of Methods for the Diffusive Color Problem

We follow the evolution of the two-dimensional system

$$(5.1)\quad \frac{\partial C}{\partial t} + U\frac{\partial C}{\partial x} + V\frac{\partial C}{\partial y} = \nu\left(\frac{\partial^2 C}{\partial x^2} + \frac{\partial^2 C}{\partial y^2}\right) + \delta(x-x_0,\ y-y_0,\ t)$$

where C represents a passive scalar quantity, the advecting velocity field (U,V) has been chosen to be a field of rigid rotation; ν is a diffusion coefficient; and the δ function represents an instantaneous point source for the scalar field C.

The finite-difference model employed is

$$
\begin{aligned}
C^{n+1}_{i,j} = C^{n}_{i,j} &- \frac{3}{2}\Delta t \left\{ U\left(\frac{C^{n}_{i+1,j} - C^{n}_{i-1,j}}{2\Lambda}\right) + V\left(\frac{C^{n}_{i,j+1} - C^{n}_{i,j-1}}{2\Lambda}\right) \right\} \\
&+ \frac{1}{2}\Delta t \left\{ U\left(\frac{C^{n-1}_{i+1,j} - C^{n-1}_{i-1,j}}{2\Lambda}\right) + V\left(\frac{C^{n-1}_{i,j+1} - C^{n-1}_{i,j-1}}{2\Lambda}\right) \right\} \\
&+ \frac{\nu\Delta t^{2}}{\Lambda^{2}} \left\{ C^{n}_{i+1,j+1} + C^{n}_{i-1,j-1} + C^{n}_{i+1,j-1} + C^{n}_{i-1,j+1} - 4C^{n}_{i,j} \right\} \\
&+ \delta^{\circ}(i_0,j_0)
\end{aligned}
\tag{5.2}
$$

where $\delta^{\circ}(i_0,j_0)$ represents an instantaneous point source located at point (i_0,j_0), and $\Delta = \Delta x$ or Δy is the horizontal grid increment. The advective terms are written with Adams-Bashforth time-differencing and the viscous term is explicitly differenced in time. Periodic boundary conditions are assumed.

The finite spectral model employed is

$$
\begin{aligned}
\tilde{C}^{n+1}_{k_1,k_2} = \frac{1}{\left(1 + \frac{\nu\Delta t k^{2}}{2}\right)} \Bigg[&\left(1 - \frac{\nu\Delta t k^{2}}{2}\right)\tilde{C}^{n}_{k_1,k_2} - \frac{3}{2}\Delta t \left\{ ik_1(\tilde{UC}^{n})_{k_1,k_2} + ik_2(\tilde{VC}^{n})_{k_1,k_2} \right\} \\
&+ \frac{1}{2}\Delta t \left\{ ik_1(\tilde{UC}^{n-1})_{k_1,k_2} + ik_2(\tilde{VC}^{n-1})_{k_1,k_2} \right\} \Bigg] \\
&+ \left(\widetilde{\delta^{\circ}(i_0,j_0)}\right)
\end{aligned}
\tag{5.3}
$$

where k_1, k_2 represent the two horizontal wavenumbers,

$$k^2 = k_1^2 + k_2^2$$

and the tilda (~) designates the two-dimensional discrete Fourier transform of the indicated field.

In particular, the term

$$\widetilde{(UC^n)}_{k_1,k_2}$$

designates the (k_1, k_2) component of the alias-free product of the velocity component U with the real-space field C at time step n. The achievement of alias-free non-linear products is performed as described in Appendix 3. The time-differencing used for the advective terms is the Adams-Bashforth scheme, while the viscous term is represented with Crank-Nicholson time differencing. The expression (5.3) makes use of the fact that the constant advecting velocity field is non-divergent.

To emphasize the power of the spectral approach, the finite-difference computations are performed with both 32x32 and 96x96 points grid resolution, whereas the spectral calculations are performed only on a 32x32 point grid. In each case we used a true point singularity as the initial source term, of non-dimensional magnitude 1.0 units. Thus the initial conditions are identical in each case, which satisfies an objection raised by (C-S) to the preliminary results. Previous experience with spectral calculations of the color equation show that the spectral approach is remarkably accurate for a distributed scalar field (Orszag, 1971a) but should be appreciably less accurate for a true point source. In every case the numerical time step was chosen sufficiently small that time-differencing errors were negligible.

For each system, the physical-space grid is square, and the center of rotation coincides with the center of the grid. The initial point-source distribution is located midway between the center of rotation and the left boundary of the grid. The frequency of rotation is such that one full rotation requires 100 time steps.

We present results for the following cases:

(a) Finite-Difference Scheme with 32x32 point resolution, viscosity $\nu = .05$

(b) Spectral Scheme with 32x32 point resolution (i.e. wavenumber cutoff K=16), viscosity $\nu = .05$

(c) Finite-Difference Scheme with 32x32 resolution, $\nu = .005$

(d) Spectral Scheme with 32x32 point resolution, $\nu = .005$.

Figure 5.1 displays the initial point-source distribution, that has been entirely machine-constructed with ten equal contour intervals, dashed lines representing negative-valued contour lines. The contour intervals were generated automatically with contour spacing

$$\Delta C = \frac{C_{max} - C_{min}}{10}$$

where C_{max}, C_{min} are respectively, the maximum and minimum values of the scalar field C encountered anywhere on the grid at the given time step. Thus, no two figures show the same contour spacing, a point which will become important shortly. However, the choice of contour interval is now made in entirely objective manner, as was not the case in the preliminary results seen by (C-S).

Figure 5.1 Initial Point-Source Distribution (t=0)

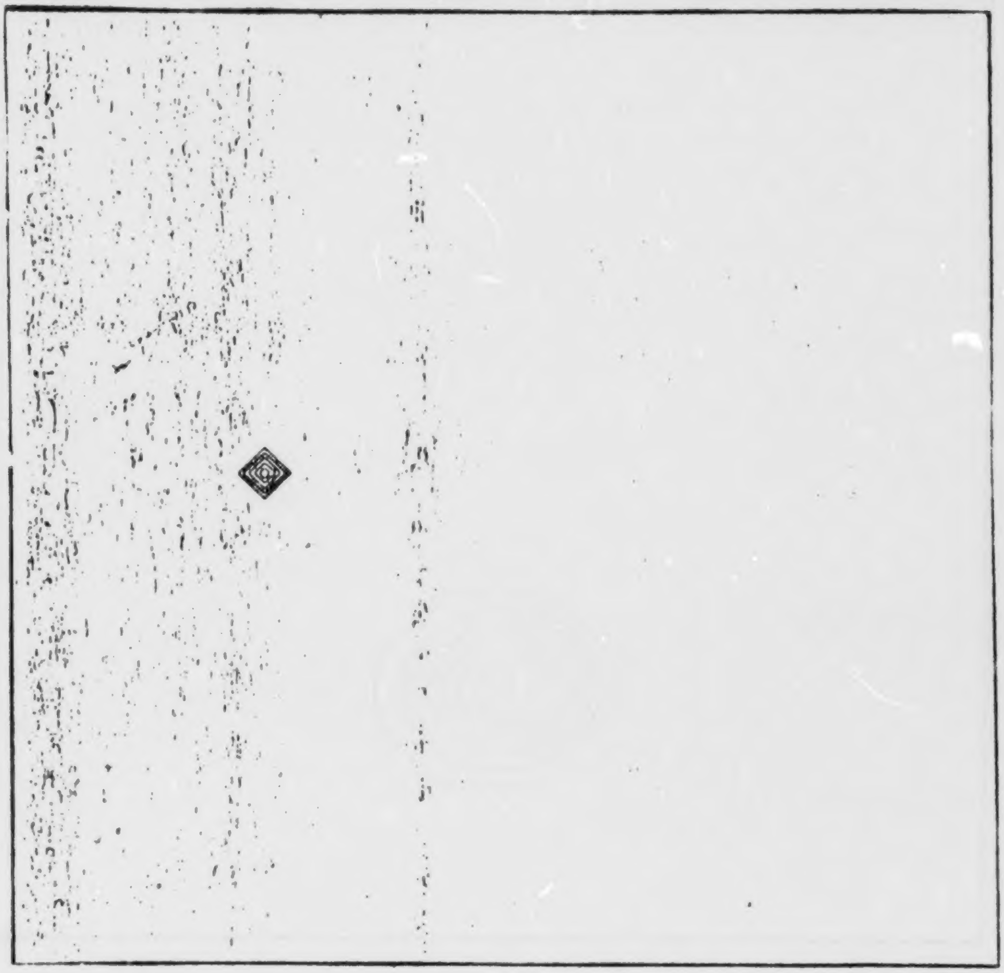

Contour from 0. to 1.00E+00

Figure 5.2 Finite-Difference Scheme
($\nu = .05$, t = 1/4 revolution)
32 x 32 point resolution

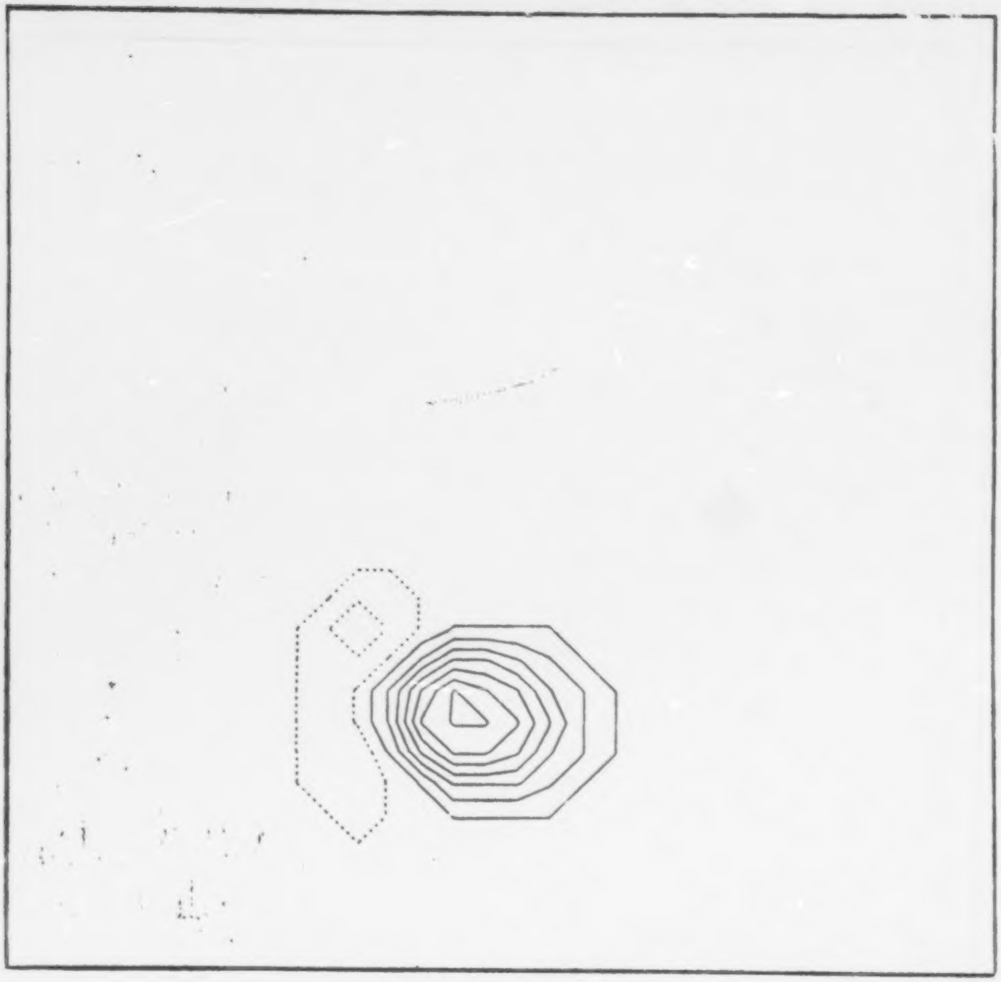

F.D. Scheme T = 25.0000
Contour from -1.42E-02 to 5.31E-02 Interval 6.73E-03

Figure 5.3 Spectral Scheme
32 x 32 point resolution

$\nu = .05$
t = 1/4 revolution

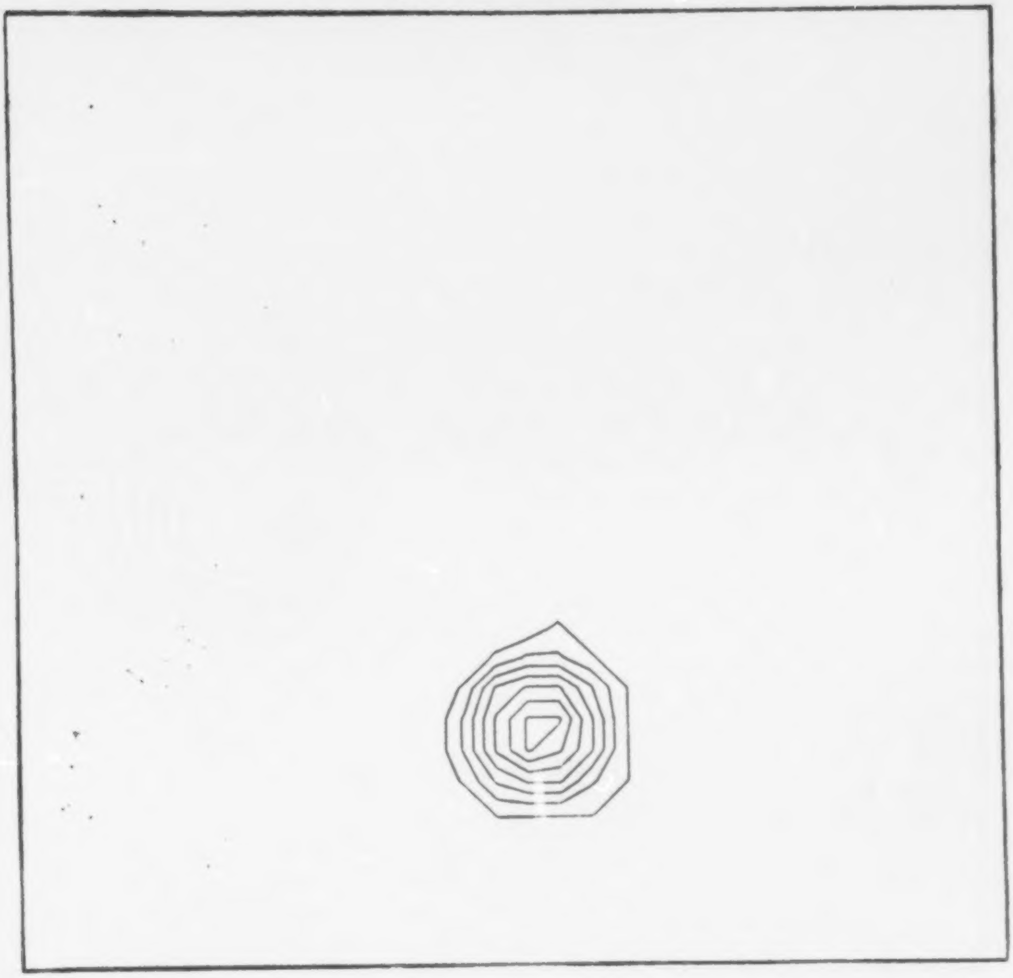

Spectral Scheme T = 25.0000
Contour from -1.19E-03 to 6.21E-02 Interval 7.91E-03

Figure 5.4 Finite-Difference Scheme
32 x 32 point resolution
$\nu = .05$
t = 1/2 revolution

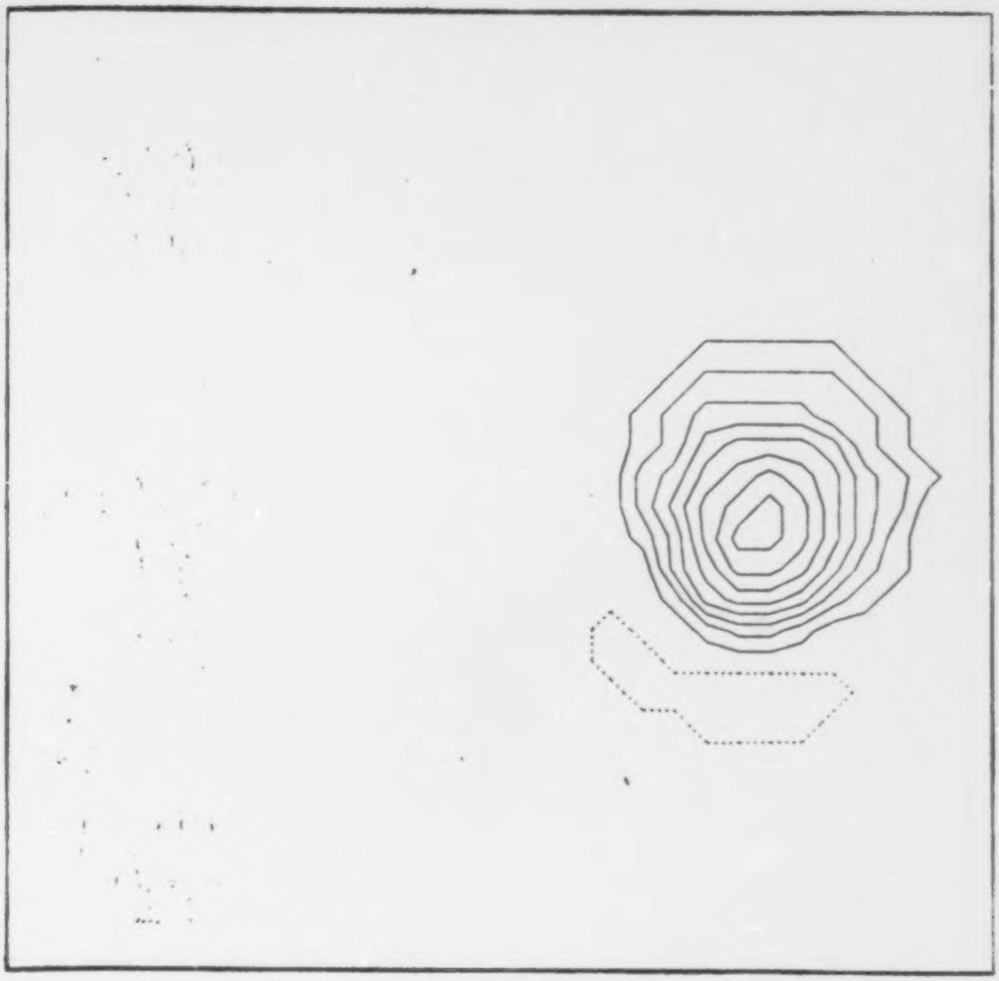

F.D. Scheme T = 50.0000
Contour from -4.58E-03 to 2.84E-02 Interval 3.30E-03

Figure 5.5 Spectral Scheme
32 x 32 point resolution
$\nu = .05$
t = 1/2 revolution

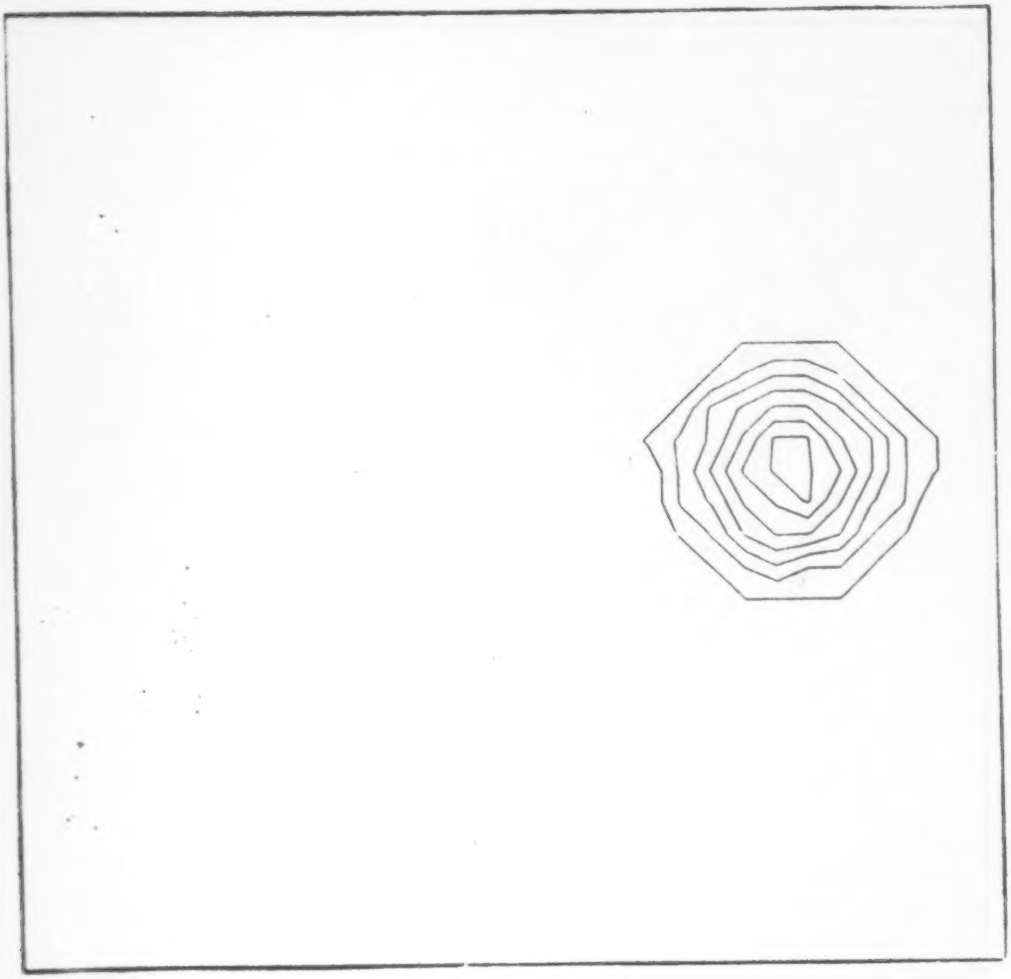

Spectral Scheme T = 50.0000
Contour from -5.92E-04 to 3.15E-02 Interval 4.01E-03

Figure 5.6 Finite-Difference Scheme

32 x 32 point resolution

$\nu = .005$

t = 1/4 revolution

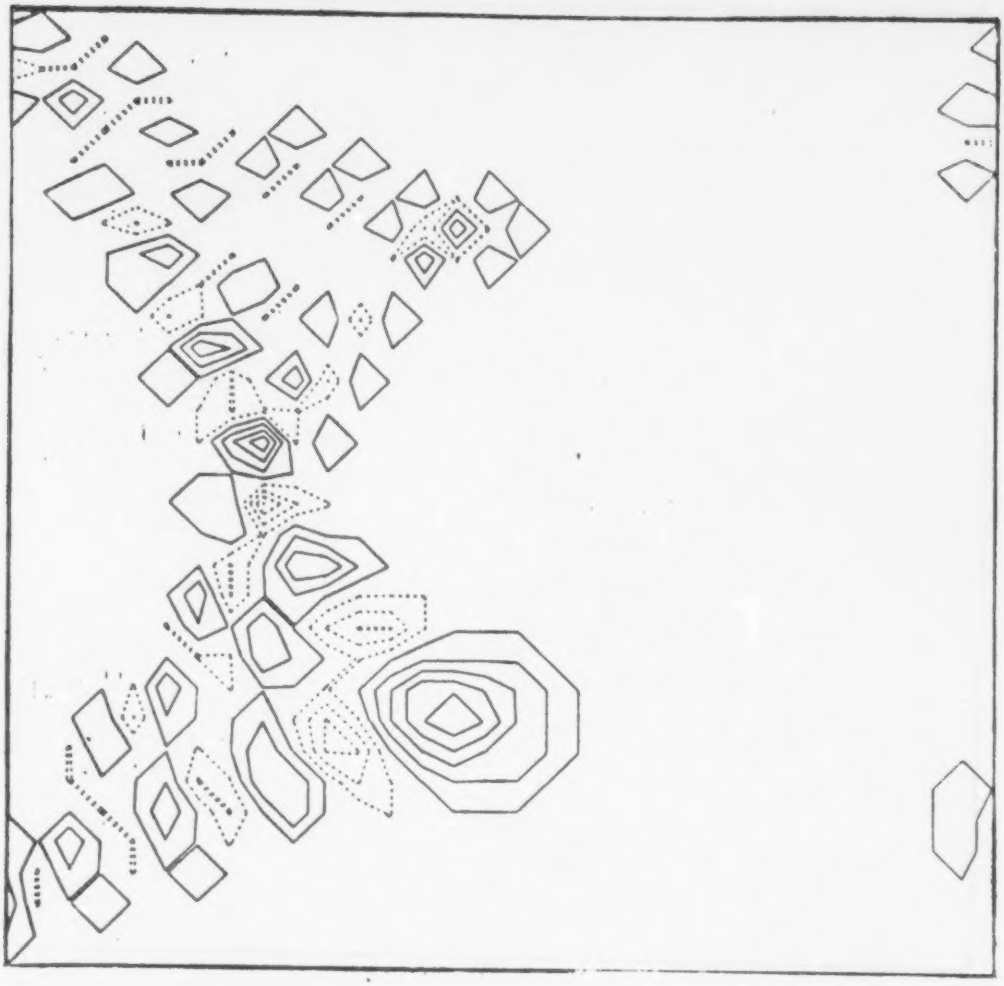

F.D. Scheme T = 25.0000

Contour from -1.09-01 to 1.13E-01 Interval 2.22E-02

Figure 5.7 Spectral Scheme
32 x 32 point resolution
$\nu = .005$
t = 1/4 revolution

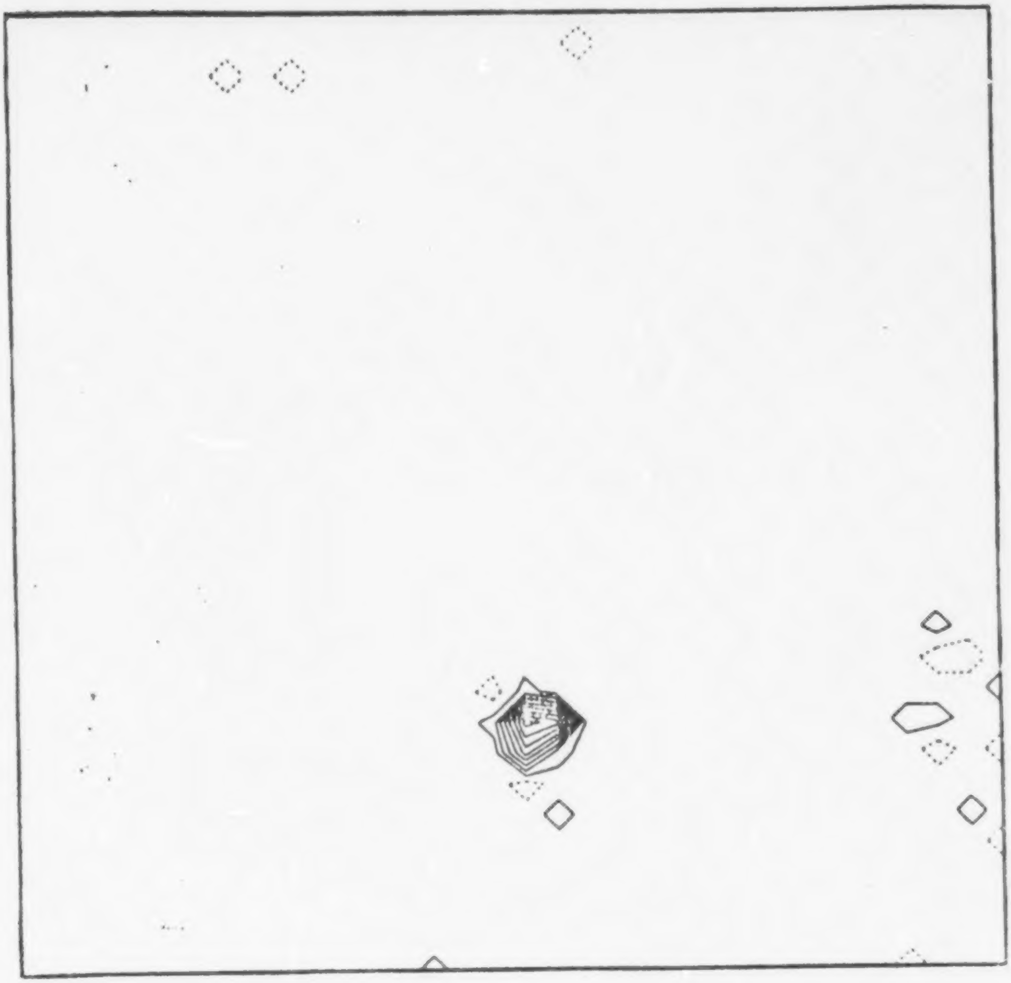

Spectral Scheme T = 25.0000
Contour from -6.38E-02 to 3.70E-01 Interval 4.34E-02

Figure 5.8 Finite-Difference Model
32 x 32 point resolution
$\nu = .005$
t = 1/2 revolution

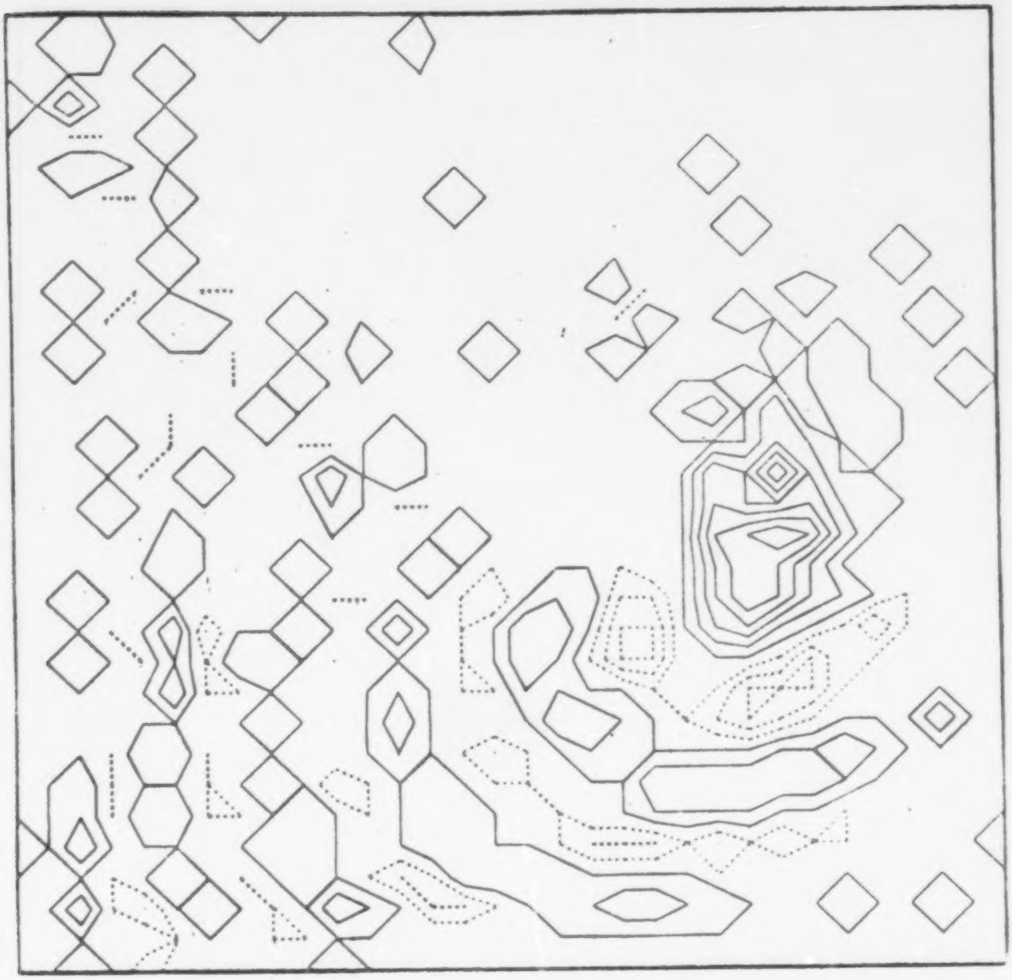

F.D. Scheme T = 50.0000

Contour from -5.02E-02 to 7.58E-02 Interval 1.26E-02

Figure 5.9 Spectral Model
32 x 32 point resolution
$\nu = .005$
t = 1/2 revolution

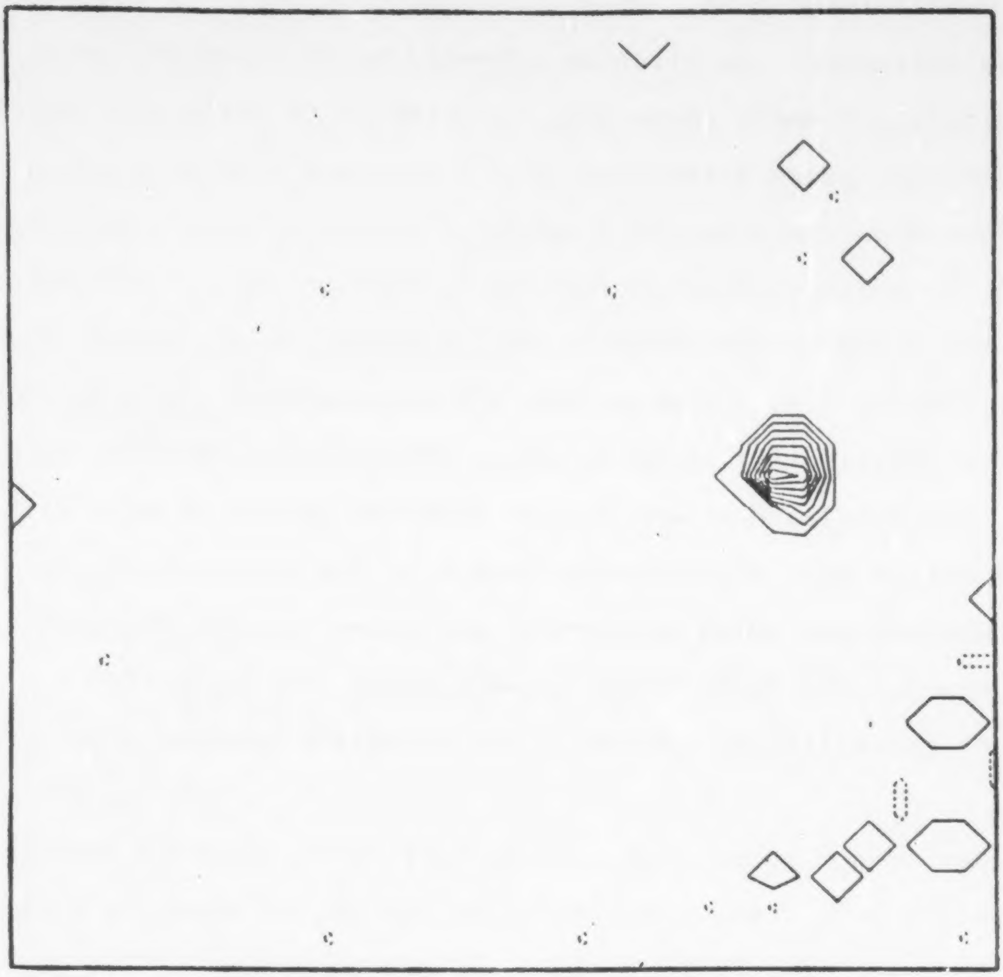

Contour from -5.62E-2 to 2.55E-1 Interval 3.11E-1

In figures 5.2, 5.3 we compare, respectively, cases (a) and (b) after one-quarter resolution. Note that the contour interval in the spectral case (5.3) is about 17% larger than that in the finite-difference case. It is observed that case (b) more accurately reproduces the circular symmetry to be expected, while case (a) displays a small phase lag, relative to the expected center of symmetry, axial distortion, and a spurious numerical noise manifested as characteristic negative "trailing wake" (the explanation for which we have considered in section 2.1). Proceeding with the temporal evolution of both systems out to $t=1/2$ revolution, figures 5.4, 5.5 show that the spectral run continues to yield a distribution which is quite circularly symmetric, with no wake structure, and preserves the expected center of mass of the distribution much more closely than does the finite-difference run, wherein the axial distortion and phase lag are becoming quite pronounced. The differences between these two cases (for $\nu = .05$) are not yet striking, however. The situation changes greatly as $\nu \to 0$.

Let us now compare the two methods for a ten-fold reduction in viscosity, $\nu = .005$, i.e., cases (c) and (d) as shown in figures 5.6, 5.7, for $t=1/4$ resolution. With a reduction in ν, we would expect that the effect of the strong discontinuity in the source distribution would become more apparent, since the smoothing effect of the diffusion term is correspondingly reduced. Now the spectral scheme shows to considerably better advantage with regard to preservation of phase, symmetry of distribution, and suppression of superfluous trailing wake structure. In fact, it would already be difficult to argue that the finite-difference model corresponds to physical reality in any useful sense. Let us look as well at the results for t=1/2 resolution (figures 5.8, 5.9). The continued high fidelity of the spectral model to the expected continuum solution is truly impressive. Note that the phase information is still preserved remarkably well, and the spurious numerical noise is of small amplitude ($\lesssim$ 10% of the peak).

The (32x32) spectral runs required about eight times longer cpu execution time than the (32x32) finite-difference runs. However, it should be emphasized that these runs did not use optimally-coded Fast Fourier Transform routines (which would save about 50% execution time). Moreover, we employed for these runs a fully alias-free spectral algorithm, and Orszag has shown that the partly aliased pseudospectral method offers, in this case, a four-fold reduction in required computation time, without appreciable degradation of results. Together, therefore, these modifications would effect at least an eight-fold savings in computation time. These results suggest therefore that spectral methods are cost-effective for simulation of the diffusive color problem and offer significant core storage savings compared to finite-difference methods, for equivalent accuracy.

Finally, it is necessary to correct a misconception entertained by Chan and Stuhmiller, as evidenced by a comment of theirs concerning the use of spectral techniques for the color problem:

"The example used in the comparison is a linear problem, i.e., the velocity field is given explicitly ..."In spectral method, there are two general approaches to nonlinear problems in which the nonlinearity is of the product type. The first approach is to do the entire calculation in the Fourier space; the nonlinear products lead to evaluation of 'convolution sum' which is in general very time consuming. The second approach is to transform from Fourier space into physical space and perform the multiplication there for the nonlinear terms. When transforming back into Fourier space, 'aliasing' has to be controlled to avoid the buildup of errors. Bass was probably referring to the second approach as the "spectral method" in his memo. The first approach is not susceptible to phase errors since the amplitude and phase of each Fourier mode are dealt with directly as dependent variables. But the evaluation of convolution sums for nonlinear problems makes this approach rather expensive. On the other hand, the second approach is not free of phase error because of the calculation performed in the physical space."

In response to these comments we should note that, first, the color problem is "linear" in the sense that the velocity fields do not enter quadratically, but inasmuch as it is necessary to evaluate the advective product $V\cdot\nabla C$ where $V=V(x,y)$ is a spatially variable field, the computation is nonlinear in the usual sense; and we require an accurate efficient technique for the alias-free representation of multiplicative fields.

Second, it is not true that the "spectral method" to which we referred is implicitly aliased, or is phase-error contaminated. The spectral method (a truncated Galerkin Fourier method) which we used in these calculations is

(a) entirely free of phase error

(b) entirely free of aliasing misrepresentations, since we used the alias-renewal technique described in Appendix 3.

Apparently Chan and Stuhmiller have confused spectral with pseudospectral methods. The alias-free evaluation of nonlinear products does not require the explicit evaluation of convolution sums. Perhaps the most single advantage of the methods introduced by Orszag is that we can achieve the same results as would be obtained by computationally expensive convolution, with much greater efficiency via the "shifted-grid" algorithms (Orszag 1971a, 1971b).

5.2 Comparison of Methods for Neuringer's Problem

In this section we compare spectral and conventional second-order finite-difference numerical solutions to the problem solved analytically by Neuringer (1968), namely, the advection-diffusion of an instantaneous point source in a two-dimensional linearly sheared wind field.

Neuringer presents an analytic solution for the evolution of the two-dimensional system

$$\frac{\partial t}{\partial t} + ay\frac{\partial t}{\partial x} - c\frac{\partial t}{\partial y} = d\left(\frac{\partial^2 f}{\partial x^2} + \frac{\partial^2 f}{\partial y^2}\right) + \delta(x-x', y-y', t) \tag{5.4}$$

where the δ-function represents an instantaneous source and a, c, d are constants. He shows that with the transformations

$$\bar{t} = at$$

$$\bar{x} = (a/c)(x-aty-act^2/2)$$

$$\bar{y} = (a/c)(y+ct)$$

and with the δ-function source at the origin, $\bar{x}' = \bar{y}' = 0$, the analytic solution is

$$F(\bar{x},\bar{y},\bar{t}) = \frac{1}{\bar{t}\sqrt{1+\bar{t}^2/12}} \quad \exp\left[-\gamma\left\{\frac{(\bar{x}/2-\bar{t}\bar{y}/4)^2}{\bar{t}(1+\bar{t}^2/12)}\right\}\right] \tag{5.5}$$

where

$$\gamma^2 = c^2/ad \; .$$

Figs. 2-5 in Neuringer's paper attempt to show the variation of the dimensionless distribution function F. It was observed that these figures are entirely incorrect, except for the special paraetric choices $\bar{x} = 0$ or $\bar{y} = 0$. We have therefore reevaluated numerically Neuringer's analytic expression for $F(\bar{x},\bar{y},t)$, equation (5.5) above. Fig. 5.10 exhibits some correct representative curves of $\bar{F}$ vs. $\bar{x}$ for the case $\gamma = 1.0$, $t = 0.5$. (Note, for example, that by comparison with fig. 5.10, Neuringer's curve for $\bar{y} = -5$ is wrong by more than six orders of magnitude, while the curve for $\bar{y} = 0$ is correct.)

Superimposed on fig. 5.10 are some points sampled from a spectral simulation of equation 5.4 with 32x32 point resolution, and the same choices of parameters γ, $\bar{t}$, and $(\bar{x},\bar{y})$ dependence. On the scale of the figure the spectral results are indistinguishable from the analytic results. Table 5A presents some sampled values for the ratio $F(\bar{x},\bar{y})/F(0,0)$ spaced at unit intervals of x and y, obtained from direct numerical evaluation of equation 5.4. In this and subsequent tables the notation 2(-8) is to be understood as 2×10^{-8}, and so forth. In Fig. 5.11 we display a two-dimensional contour plot of this ratio, constructed from more detailed numerical tables. The corresponding contour plots constructed from the spectral and finite difference runs cannot be distinguished by eye from those shown in the figure and so are not included.

To permit more exact comparison of the spectral and finite-difference computations for Neuringer's problem, we have performed a second series of three runs, with parameter γ now chosen for convenience as 4.0, and the computation carried out to time $\bar{t} = 0.5$. For each run, the time increment was chosen small enough so that time-differencing errors were negligible. The three runs compared were:

(a) spectral computation on a 32x32 point space grid (hereafter called run (a));

Figure 5.10

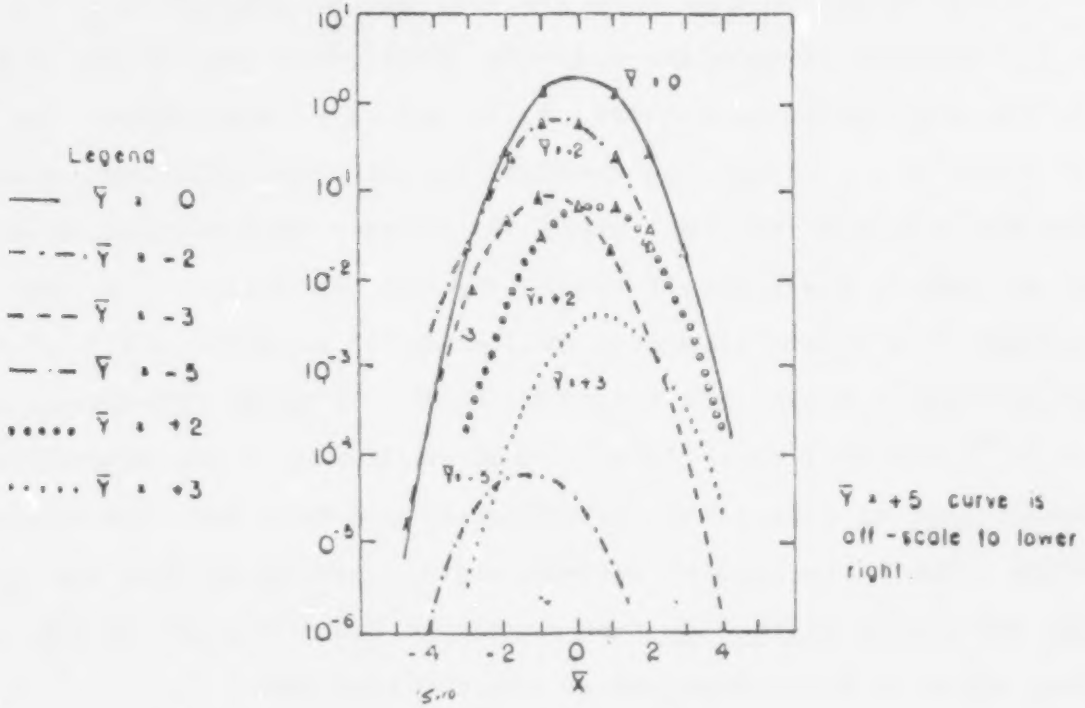

Ȳ = +5 curve is off-scale to lower right.

Figure 5.10 Correct Neuringer FCN for $\gamma = 1$, $\bar{t} = 0.5$
Δ = Points Obtained from Spectral Run for Same Combinations $(\bar{X}, \bar{Y})$

Figure 5.11

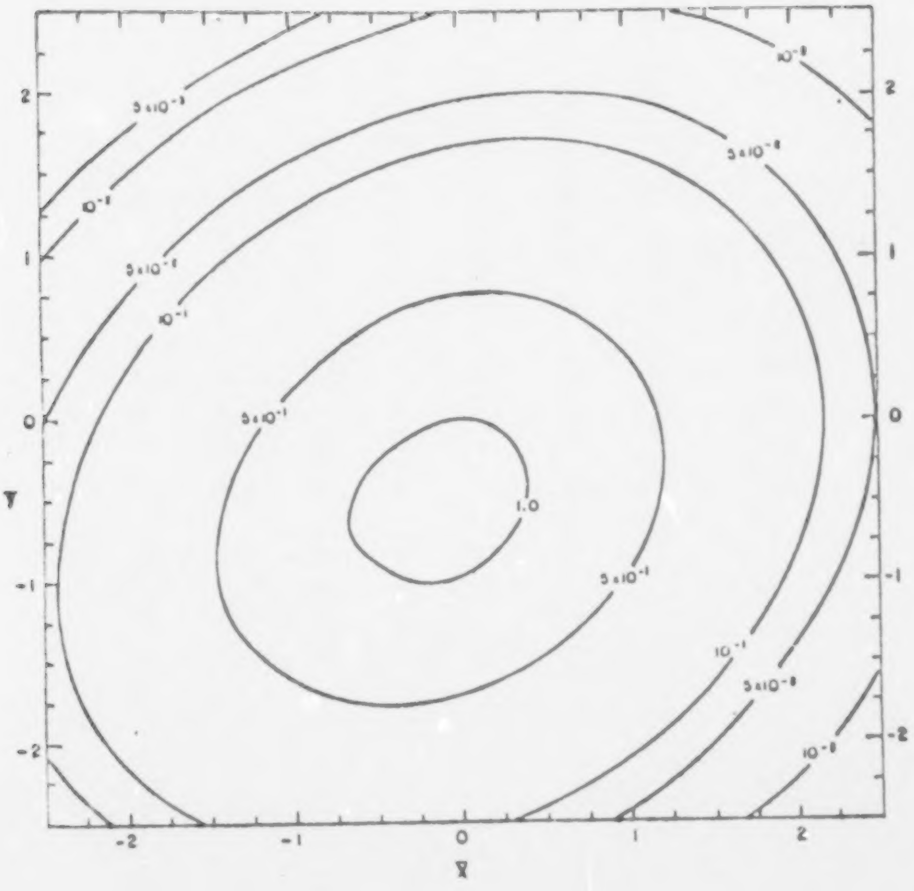

Figure 5.11 Neuringer Problem ($\gamma = 1.0$, $\bar{t} = 0.5$)
Analytic Value of $F(\bar{x},\bar{y})/F(0,0)$

TABLE 5A

Analytic Evaluation of $F(\bar{x},\bar{y})/F(0,0)$ for $\gamma = 1.0$, $\bar{t} = 0.5$

		$\bar{x}$								
		- 4	- 3	- 2	- 1	0	1	2	3	4
	4	-	2(-8)	5.5 (-7)	6.40(-6)	2.78(-5)	4.54(-5)	2.78(-5)	6.40(-6)	5.5 (-7)
	3	4(-8)	2.53(-6)	6.10(-5)	5.53(-4)	1.88(-3)	2.40(-3)	1.15(-3)	2.08(-4)	1.40(-5)
	2	2.45(-6)	1.23(-4)	2.33(-3)	1.65(-2)	4.40(-2)	4.40(-2)	1.65(-2)	2.33(-3)	1.23(-4)
	1	5.29(-5)	2.08(-3)	3.08(-2)	1.71(-1)	3.57(-1)	2.79(-1)	8.21(-2)	9.06(-3)	3.75(-4)
$\bar{y}$	0	3.95(-4)	1.22(-2)	1.41(-1)	6.13(-1)	1.00(0)	6.13(-1)	1.41(-1)	1.22(-2)	3.95(-4)
	-1	1.02(-3)	2.46(-2)	2.23(-1)	7.59(-1)	9.70(-1)	4.65(-1)	8.38(-2)	5.66(-3)	1.44(-4)
	-2	9.12(-4)	1.72(-2)	1.22(-1)	3.25(-1)	3.25(-1)	1.22(-1)	1.72(-2)	9.12(-4)	1.81(-5)
	-3	2.82(-4)	4.17(-3)	2.32(-2)	4.83(-2)	3.78(-2)	1.11(-2)	1.22(-3)	5.08(-5)	7.9 (-7)
	-4	3.02(-5)	3.49(-4)	1.52(-3)	2.48(-3)	1.51(-3)	3.49(-4)	3.02(-5)	9.8 (-7)	1(-8)

(b) second-order finite-difference computation on a 48x48 point grid (called run (b)), with one and one-half times greater horizontal resolution than run (a);

(c) Second-order finite-difference computation on a 96x96 point grid (called run (c)), with three times greater horizontal resolution than run (a).

The equations used in the finite-difference and spectral models to simulate (5.4) are virtually identical to those described for the color problem, e.g., equations (5.2) and (5.3), the only differences occurring in the representation of the advective terms. That is, the velocity field $U(x,y)$ is replaced by $+(ay)$, and the velocity field $V(x,y)$ is replaced by the constant $-c$. The time-stepping schemes used here are identical to those described for the color problem.

Table 5B displays the values of the ratio $F(\bar{x},\bar{y})/F(0,0)$ obtained by tabulating expression (5.5), for equally-spaced points $(\bar{x},\bar{y})$ spanning the region of maximum concentration amplitude. Table 5C shows the absolute errors made by the spectral run, i.e., the differences between the analytic values of the ratio $F(\bar{x},\bar{y})/F(0,0)$ and those obtained from the spectral computation. In like manner, Tables 5D, 5E display the absolute errors of the 48x48 point and the 96x96 point finite difference runs, respectively.

Upon examination of these tables, we may draw several significant conclusions. First, we observe that the errors made by the run (b) are consistently about four times greater than, and uniformly in the same direction as, the errors made by run (c). Second, we see that, in the region of maximum amplitude, both the (a) and

TABLE 5B

Analytic Value of $F(\bar{x},\bar{y})/F(0,0)$

($\gamma = 4.0, \quad \bar{t} = 0.5$)

		$\bar{x}$				
		- 1	- 1/2	0	+ 1/2	+ 1
$\bar{y}$	+ 1/2	.019	.104	.216	.169	.050
	0	.141	.613	1.000	.613	.141
	- 1/2	.368	1.252	1.600	.767	.138
	- 1	.332	.885	.885	.332	.047
	- 3/2	.104	.216	.169	.050	.005
	- 2	.011	.018	.011	.003	<.001

TABLE 5C

Absolute Errors in Spectral Run

				$\bar{x}$		
		- 1	- 1/2	0	+ 1/2	+ 1
$\bar{y}$	+ 1/2	<.001	-.001	-.002	-.003	-.004
	0	<.001	<.001	-	-.001	-.004
	- 1/2	+.004	+.007	+.011	+.012	+.004
	- 1	+.007	+.013	+.019	+.016	+.009
	- 3/2	+.003	+.008	+.001	+.007	+.004
	- 2	<.001	+.003	+.005	+.002	+.001

TABLE 5D

Absolute Errors in 48*48 Point Finite Difference Run

		$\bar{x}$				
		- 1	- 1/2	0	+ 1/2	+ 1
$\bar{y}$	+ 1/2	-.003	-.013	+.020	-.015	-.007
	0	-.006	-.017	-	-.017	-.006
	- 1/2	-.023	-.056	-.028	-.036	-.009
	- 1	-.039	-.085	-.063	-.034	-.006
	- 3/2	-.007	-.006	<.001	-.003	<.001
	- 2	+.004	+.007	+.005	<.001	<.001

TABLE 5E

Absolute Errors in 96*96 Point Finite Difference Run

				$\bar{x}$		
		- 1	- 1/2	0	+ 1/2	+ 1
$\bar{y}$	1/2	+.001	-.003	-.005	-.004	-.002
	0	-.002	-.004	-	-.004	-.002
	- 1/2	-.006	-.014	-.007	-.008	-.002
	- 1	-.010	-.022	-.016	-.009	-.002
	- 3/2	-.002	-.001	<.001	-.001	<.001
	- 2	+.001	+.002	+.001	<.001	<.001

(c) computations are of about equal accuracy and capture equally well the spatially local peak structure (although the finite-difference approach is "local" and the spectral approach is "global" in nature). Third, with some reference to the more extensive tabulations from which these tables have been extracted, it is seen that, in the wings of the distribution, the analytic result and the finite-difference calculations decay to zero very rapidly. By contrast, the spectral computation makes a small oscillatory error of absolute magnitude less than $3*10^{-3}$ that of the peak amplitude. This small-amplitude residual oscillatory error is typical of spectral representations for strongly peaked fields. However, as we have noted previously, the error made by truncating a spectral representation at N terms decreases more rapidly as N is increased than any power of 1/N. Hence, for only modest additional increase in spectral resolution, the magnitude of this characteristic oscillation can be reduced to negligible proportions.

It is important to note that, for this two-dimensional computation, therefore, the core storage advantage of the spectral method, in this case, is almost thirty-fold. This makes it practicable, from the point of view of available core, to pursue a much larger class of calculations than are presently possible with finite-difference methods.

Again, as regards execution time, the spectral method is more than competitive. Run (a) required about 36% more computation time than did run (c). However, as before, the spectral calculations were made in fully alias-free manner, and an immediate four-fold reduction in computation time is possible if we relax the requirement for fully alias-free spectral interactions, by performing the calculations is pseudospectral manner. Thus, for comparable accuracy, the spectral approach is to be preferred, on economic grounds, for solution of advection-diffusion problems typified by Neuringer's problem. We believe, therefore, that spectral methods merit serious attention for prospective air-quality simulation efforts.

6.0 Spectral Modeling of the Turbulent Diffusion of a Passive Scalar

This chapter describes a modeling effort, as yet unsuccessful, using state-of-the-art spectral methods to study the turbulent diffusion of a passive scalar source in a fully three-dimensional, turbulent, sheared velocity field, without recourse to closure arguments. The impetus for this effort stemmed from the expectation that such a model would provide an idealized set of turbulent diffusion data, free of closure parameterization assumptions, against which various air-quality turbulent diffusion models might be tested. Moreover, it was anticipated that the model might permit the compilaation of model turbulent diffusion data, suitable for the evaluation of eddy Austauch coefficients, for a variety of cases for which observational data are lacking, or for which existing data are unreliable.

These expectations seemed well justified, at the initiation of this study effort, by the very real successes achieved by earlier spectral numerical models of this type in reproducing the essential dynamics of three-dimensional turbulent flows in a number of cases (Orszag and Patterson 1972, Orszag and Pao 1974), and by the demonstrated utility of the numerical results so obtained in testing the validity of various formal turbulence theories. The model experiments contemplated for the current effort presupposed, therefore, the availability of computational resources (core storage and CPU time) comparable to that employed in the previous successful efforts. It was not until well along in the current contract study, and only after the various computer codes had been written and checked out, that the computational resources available to us were thenceforth severely restricted. The critical limitation was that of core storage. The experiments had been planned on the premise that the codes could be run with $(32)^3$ modal resolution, as had previously been the case at the Lawrence Berkeley CDC facility. Unfortunately, new and unforeseen user demands upon that facility had the practical effect of restricting our model experiments to only $(16)^3$ modes. Previous experience with homogeneous turbulence codes suggested that $(16)^3$ modal resolution was but marginally adequate for the evolution of physically realistic turbulent flows, and we had but little hope for the prospective success of a $(16)^3$ model for strongly sheared flows. Nevertheless because of our problems with Lawrence Berkeley we had no choice but to proceed with our experiments at the reduced resolution. Initially we hold out some hope for partial success because the largest scales of motion (which are the most important for turbulent eddy transport) could still be adequately resolved. However, after the fact, the difficulty of achieving physically credible small-scale equilibrium statistics in the presence of a strongly sheared mean flow at the $(16)^3$ resolution precluded our getting satisfactory results. (The attainment of equilibrium is necessary to make possible a meaningful comparison of our numerical model with the corresponding predictions of a turbulence closure model based upon equilibrium turbulent conditions.)

The remainder of this chapter is devoted, first, to a thorough description of the model we have developed. Then, a discussion is given of the difficulties encountered, by reference to figures which depict the evolution of the velocity and vorticity fields during the course of one of our unsuccessful experiments.

6.1 The Numerical Model

In this section we define the Boussinesq equations describing the physical system to be simulated, and develop the spectral forms of these equations which are actually implemented in the computer model which has been constructed.

We begin from the familiar Boussinesq system of equations for shallow layer convection in an effectively incompressible fluid. The scaling arguments underlying the derivation of these equations are presented in Spiegel and Veronis (1960) and Calder (1967), and will not be restated here. The Boussinesq equations may be written as

$$(6.1) \qquad \frac{d\underline{V}}{dt} = -\frac{\nabla p}{\rho_{00}} + \frac{gT\hat{\lambda}}{T_{00}} + \nu\nabla^2\underline{V}$$

$$(6.2) \qquad \nabla\cdot\underline{V} = 0$$

$$(6.3) \qquad \frac{g}{T_{00}}\frac{dT}{dt} + N^2W = \kappa\frac{g}{T_{00}}\nabla^2T$$

where

$$\frac{d}{dt} = \frac{\partial}{\partial t} + \underline{V}\cdot\nabla$$

$\hat{\lambda}$ is a unit vector in the vertical direction

$\underline{V}$ is the three-dimensional velocity field

p is the deviation of pressure from its equilibrium value P_e

T is the deviation of temperature from its equilibrium value T_e, which is a linear function of height z, $T_e = T_{00}(1-z/H)$

T_{00}, ρ_{00} are the surface equilibrium temperature and density, respectively,

N^2, the square of the Brunt-Vaisala frequency, = $\frac{g}{T_{00}}\left(\frac{\partial T_e}{\partial z} + \frac{1}{c_p}\right)$, assumed constant

ν, the kinematic viscosity, = μ/ρ_{00}, where μ is the coefficient of viscosity

σ, the thermal viscosity = σ/P_{00}, where σ is the thermal conductivity

Equation (6.1) is the momentum equation, incorporating the continuity condition (6.2). Equation (6.3) is the heat equation. For convenience, we will define the variables $P = p/\rho_{00}$, $\Theta = \frac{gT}{T_{00}}$, whence

$$(6.4) \qquad \frac{\partial \underline{V}}{\partial t} + \underline{V}\cdot\nabla\underline{V} = -\nabla P + \Theta\hat{\lambda} + \nu\nabla^2\underline{V}$$

$$(6.5) \qquad \frac{\partial \Theta}{\partial t} + \underline{V}\cdot\nabla\Theta + N^2 W = \kappa\nabla^2\Theta$$

The term $\Theta\hat{\lambda}$ in (6.4) provides the convective coupling of temperature to the vertical velocity field, and the term N^2W in (6.5) represents the effect of basic-state stratification upon the evolution of the thermal field.

Equation (6.4) may be written in the rotational form

$$(6.6) \qquad \frac{\partial \underline{V}}{\partial t} - \underline{V}\times\underline{\omega} = -\nabla\left(P + \frac{1}{2}\underline{V}\cdot\underline{V}\right) + \Theta\hat{\lambda} + \nu\nabla^2\underline{V}$$

where $\underline{\omega} = \nabla\times\underline{V}$ is the vorticity field..

Equation (6.5) may be written, using the incompressibility condition, as

$$(6.7) \qquad \frac{\partial \Theta}{\partial t} + \nabla\cdot(\underline{V}\Theta) + N^2 W = \kappa\nabla^2\Theta.$$

Equations (6.6), (6.7) and (6.2), together with appropriate initial and boundary conditions, define the system to be simulated spectrally.

To integrate this system with time, we use truncated Fourier spectral methods. That is, we represent the velocity and temperature fields in truncated discrete Fourier series (Appendix 2) of the form

$$(6.8) \qquad \underline{V}(\underline{x},t) = \sum_{|\underline{k}|<K} \underline{U}(\underline{k},t)e^{i\underline{k}\cdot\underline{x}}$$

$$(6.9) \qquad \theta(\underline{x},t) = \sum_{|\underline{k}|<K} \Theta(\underline{k},t)e^{i\underline{k}\cdot\underline{x}}$$

where the summations extend over all three-dimensional wave vectors $\underline{k}$ whose absolute values are smaller than K, the truncation wavenumber. $\underline{U}(\underline{k},t)$ and $\Theta(\underline{k},t)$ are, respectively, Fourier series coefficients of the velocity and temperature fields. We have, of course, assumed periodicity in each spatial direction.

A straightforward application of the discrete Fourier transformation to the momentum equation (6.4) leads to the spectral form (Orszag 1971a)

$$(6.10) \qquad \left(\frac{\partial}{\partial t} + \nu k^2\right)U_\alpha(\underline{k},t) = -i\underline{k}_\beta\left(\delta_{\alpha\gamma} - \frac{k_\alpha k_\gamma}{k^2}\right) \sum_{\substack{|\underline{p}|<K \\ |\underline{k}-\underline{p}|<K}} U_\beta(\underline{p},t)U_\gamma(\underline{k}-\underline{p},t)$$

$$+ \Theta(\underline{k},t)\delta_{\alpha 3}$$

where α,β,γ may each range over the three indices 1, 2, 3 (i.e., the three orthogonal directions in wavespace). The symbol $\delta_{\alpha\gamma}$ is the Kronecker delta, and summation over repeated Greek indices is implied. The pressure term has been eliminated by use of the incompressibility condition (see also the discussion in section 2.1.3). Note, however, that the form (6.10) requires that a convolution sum be evaluated for each pair of indices (β,γ). Such an approach is quite costly computationally, especially for a fully three-dimensional system. Instead, we have employed the pseudospectral approach to integration of the momentum and heat equations. Returning to equation (6.6), we see that the source of the convolution term is the nonlinear vector product term $\underline{V}\times\underline{\omega}$. To avoid the convolution requirement we use the following procedure:

(a) Beginning from the Fourier transform of the velocity field, $\underline{U}(\underline{k},t)$, create the Fourier transform of the vorticity field, $\Omega(\underline{k},t)$ by performing the wavespace operation $\underline{\Omega}(\underline{k},t) = i\ k \times U(\underline{k},t)$.

This is the direct analogue of $\underline{\omega} = \nabla\times\underline{V}$. Note that because the vorticity field is evaluated in wavespace, it is free of first-differencing phase and amplitude errors.

(b) Recover the real-space vorticity field $\underline{\omega}(\underline{x},t)$ by inverse discrete Fourier transformation upon $\Omega(\underline{k},t)$, namely

$$\underline{\omega}(\underline{x},t) = \sum_{|\underline{k}|<K} \underline{\Omega}(\underline{k},t)e^{i\underline{k}\cdot\underline{x}}.$$

Similarly, recover the realspace velocity field $\underline{V}(\underline{x},t)$ by (6.8).

(c) Evaluate, in discrete real-space, the vector cross product term $\underline{V}(\underline{x},t) \times \underline{\omega}(\underline{x},t) =$, say, $\underline{\psi}(\underline{x},t)$. This product is, of course, fully aliased unless the procedure outlined in Appendix 3 is used.

(d) Generate the discrete Fourier transform of $\underline{\psi}(\underline{x},t)$, denoted by $\underline{\Psi}(\underline{k},t)$

$$\underline{\Psi}(\underline{k},t) = \sum_{\underline{x}} \underline{\psi}(\underline{x},t)e^{-i\underline{k}\cdot\underline{x}} .$$

(e) Represent the diffusion term $\nu\nabla^2\underline{V}(\underline{x},t)$ in wavespace as

$$- \nu k^2\underline{U}(\underline{k},t) \cdot$$

Then equation (6.6) may be written in prognostic spectral form as

$$(\frac{\partial}{\partial t} + \nu k^2)\underline{U}(\underline{k},t) - \underline{\Psi}(\underline{k},t) = \theta(\underline{k},t)\hat{\lambda} . \tag{6.11}$$

The spectral form of the pressure head term, $-\nabla(P + \frac{1}{2} V\cdot V)$, need not be included in (6.11), since the only effect of this term is to guarantee that the velocity field remains incompressible. Instead, incompressibility can be enforced, at each successive time step, by requiring the replacement of $U(\underline{k},t)$ by

$$\underline{U}'(\underline{k},t) = \underline{U}(\underline{k},t) - \frac{k}{k^2}(\underline{k}\cdot\underline{U}(k,t)) \tag{6.12}$$

whence $i\underline{k}\cdot\underline{U}'(\underline{k},t) = 0$, thus maintaining the incompressibility (see section 2.1.3). The nonlinear term $\nabla\cdot(\underline{V}\theta)$ in the thermal equation (6.7) may be treated in a similar pseudospectral manner, by the following procedure:

(a) From the real-space velocity field $\underline{V}(\underline{x},t)$, and the real-space temperature field $\theta(\underline{x},t)$, from the real-space vector $\underline{V}(\underline{x},t)\theta(\underline{x},t) =$, say, $\underline{Z}(\underline{x},t)$.

(b) Create the Fourier transform of $\underline{Z}(\underline{x},t)$, which will be denoted by $\underline{\zeta}(\underline{k},t)$:

$$\underline{\zeta}(\underline{k},t) = \sum_{\underline{x}} \underline{Z}(\underline{x},t)e^{-i\underline{k}\cdot\underline{x}} \quad .$$

(c) Evaluate the divergence term $\nabla\cdot(\underline{V}\theta)$, directly in wavespace, as $ik\cdot\underline{\zeta}(\underline{k},t)$. (The divergence operation is $i\underline{k}\cdot$ in wavespace).

Thus, (6.7) may be written in spectral form as

$$\frac{\partial}{\partial t} + \kappa k^2)\theta(\underline{k},t) = - i\underline{k}\cdot\xi(\underline{k},t) - N^2U_3(\underline{k},t) \tag{6.13}$$

where $U_3(\underline{k},t)$ designates the Fourier transform of the vertical velocity field w.

Leapfrog time differencing was used for the advective terms and Crank-Nicolson time differencing for the diffusion terms. Thus, if the superscript $()^n$ designates the value of a field at the n^{th} time step $(t_n{=}n\Delta t)$ the time evolution of the system can be explicitly represented as

$$\begin{aligned}(1 + \frac{\nu k^2\Delta t}{2})\underline{U}^{n+1}(\underline{k},t) &= (1 - \frac{\nu k^2\Delta t}{2})\underline{U}^{n-1}(\underline{k},t) \\ &\quad + \Delta t[\underline{\Psi}^n(\underline{k},t) + \theta^n(\underline{k},t)\hat{\lambda}]\end{aligned} \tag{6.14}$$

$$\begin{aligned}(1 + \frac{\kappa k^2\Delta t}{2})\theta^{n+1}(\underline{k},t) &= (1 - \frac{\kappa k^2\Delta t}{2})\theta^{n-1}(\underline{k},t) \\ &\quad - \Delta t[i\underline{k}\cdot\underline{\xi}^n(\underline{k},t) + N^2U_3^n(\underline{k},t)]\end{aligned} \tag{6.15}$$

$$\underline{U}^{n+1}(\underline{k},t) \leftarrow \underline{U}^{n+1}(\underline{k},t) - \frac{i(k.k)}{k^2}\,U^{n+1}(k,t)). \tag{6.16}$$

Finally, we have included in our model a passive scalar field, whose turbulent evolution is governed by the velocity field $v(\underline{x},t)$. The scalar conservation equation may be written as

$$(6.17) \qquad \frac{dc}{dt} = \nu_c \nabla^2 c + s(\underline{x},t)$$

where $c(\underline{x},t)$ is the scalar field, ν_c is the scalar diffusion coefficient, and $s(\underline{x},t)$ is a source term for the scalar field. If we let $C(\underline{k},t)$ denote the Fourier transform of $c(\underline{x},t)$, $S(\underline{k},t)$ denote the Fourier transform of $s(\underline{x},t)$, and $\underline{M}(\underline{k},t)$ denote the Fourier transform of the product $\underline{V}(\underline{x},t)c(\underline{x},t)$, then the temporally discretized version of (6.17), by analogy with (6.15) is just

$$(6.18) \qquad (1 + \frac{\nu_c k^2 \Delta t}{2}) C^{n+1}(\underline{k},t) = (1 - \frac{\nu_c k^2 \Delta t}{2}) C^{n-1}(\underline{k},t) - \Delta t[i\underline{k}\cdot\underline{M}^n(\underline{k},t)] + \Delta t\, S^n(\underline{k},t).$$

The prognostic equations (6.14, 6.15, 6.18), together with the replacement (6.16) define the numerical model. Initial and boundary conditions will be discussed shortly.

6.2 Physical Parameters

An attempt was made to design an experiment to simulate the turbulent diffusion of a passive scalar field in a sheared, turbulent flow, in such manner that reasonable comparison could be made with the results of one or more turbulence closure models for the same physical problem. To this end, the geometrical dimensions of our numerical model were fixed as 9.6 km in each of the two horizontal directions and 0.96 km in the vertical direction. The horizontal and vertical grid intervals were 600 m and 60 m respectively. All fields were taken to be periodic in the two horizontal directions. At the upper and lower boundaries of the system, free-slip boundary conditions were imposed on the horizontal velocity components (that is $U_z = V_z = 0$), while the vertical velocity W and the scalar field C were constrained to be zero.

For the initial experiments, we chose a neutrally stratified flow, with no convective coupling between the thermal and vertical velocity fields, because it was felt that the inclusion of the stratification and Boussinesq forcing terms from the outset would impose an unwanted degree of complexity in the interpretation of the results. Accordingly, the terms $\Delta t \theta^n$ in (6.14) and $N^2 U_3^n$ in (6.15) were suppressed. Since the temperature field no longer had any dynamical significance, equation (6.15) was in fact ignored. A linearly sheared mean-velocity profile $\bar{U}(z)$ was chosen of the form:

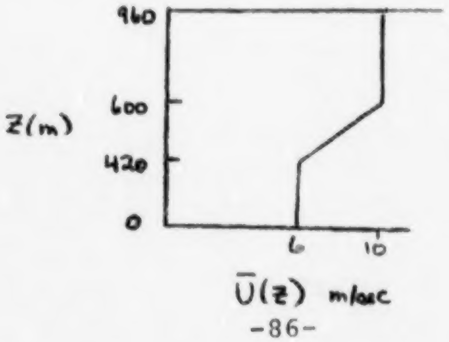

The mean flow field was perturbed initially by a small-amplitude, random three-dimensional field, the construction of which is explained in Appendix 5. The mean shear profile $\overline{U}(z)$ was maintained constant throughout the evolution of the flow by fixing in time the corresponding spectral components $U_3(0,0,K_3)$. Of course, fixing the mean wind field implies a continuous source of kinetic energy for the perturbation wind field (by Reynolds-stress conversions of the form $(u'w'\overline{U}_z)$. It was hoped that the turbulent perturbation wind field would come to approximate energy equilibrium, the Reynolds-stress excitation being matched by sufficiently vigorous viscous dissipation at the smallest scales. (In fact, during each of a number of experiments over a range of Reynolds numbers, the system never tended toward equilibrium in any physically meaningful sense. At large Reynolds numbers, there would result a strong cascade of energy toward high wavenumber, which could not be dissipated sufficiently rapidly. If the Reynolds number was reduced to the point where energy dissipation could keep up with the generation of kinetic energy, the perturbation flow structure typically degenerated into a set of large-scale vortices, in a totally unphysical manner. Some examples of these characteristic difficulties will be shown in a later section. In retrospect, this behavior may be understood as a consequence of the very limited modal resolution with which the experiments were attempted, together with the strong mean-shear profile adopted.)

6.3 An Unsuccessful Experiment

In this section we follow the evolution of the turbulent flow fields in one experiment. The objective was, as previously discussed, to create a turbulent flow structure for which the generation of kinetic energy (by conversion of the mean shear $\bar{U}_z$) would come to equilibrium with the viscous dissipation of kinetic energy. The difficulties encountered, which proved insurmountable at present, are illustrated.

To aid in visualization, all velocity fields are pictured in the form of contour plots. Positive-valued contour lines are shown as solid lines, negative-valued contour lines are shown as dashed lines. The minimum and maximum contour values and the contour interval are indicated for each figure. These contours have been constructed by an automatic contouring package.

In order to depict the three-dimensional spatial variation of the velocity fields u, v, and w, the fields are displayed in each of three orthogonal planes. That is, for example, we show the variation of the u velocity component in the y-z plane for some fixed x-coordinate, say x_0, the variation of u in the x-z plane for fixed y_0, and the variation of u in the x-y plane for fixed z_0. The choices x_0, y_0, z_0 are arbitrary; because the fields are turbulent, the individual contours are to be understood only as representative of the characteristic spatial structure in the given plane.

In the experiment to be discussed, the perturbation kinetic energy spectrum was chosen to have the spectral power law dependence $E'(k) \propto (\frac{1}{1+k^3})$ where $k=(k_1^2+k_2^2+k_3^2)^{1/2}$ is the non-dimensional wavenumber. The rms magnitudes of the initial perturbation velocity fields, compared to the rms magnitude of the mean velocity field $\bar{U}(z)$, were

$$\frac{<(U')>^{1/2}}{<\bar{U}^2>^{1/2}} = 2.2 \times 10^{-2}; \quad (U')\mathrm{rms} \sim 0.2 \text{ m/sec}$$

$$\frac{<(V')^2>^{1/2}}{<\bar{U}^2>^{1/2}} = 2.4 \times 10^{-2}; \quad (V')\mathrm{rms} \sim 0.2 \text{ m/sec}$$

$$\frac{<(W')^2>^{1/2}}{<\bar{U}^2>^{1/2}} = 5.6 \times 10^{-3}; \quad (W')\mathrm{rms} \sim 0.05 \text{ m/sec}.$$

The ratio of total perturbation energy to mean energy was initially about 5×10^{-4}. The viscosity coefficient used in the vertical direction was fixed as 1/100 that of the viscosity coefficients used in the two horizontal directions, consistent with the (square of the) ratio of vertical to horizontal spatial intervals. The particular choice made in this experiment was $\nu_{\mathrm{HORIZONTAL}} = 10$ m^2/sec., $\nu_{\mathrm{VERTICAL}} = 0.1$ m^2/sec. (In other experiments we took values of ν which were tenfold higher and lower). The equivalent large-scale Reynolds number, based upon a characteristic velocity $U=10$ m/sec., a horizontal length scale $L = \frac{10}{2\pi}$ km, and the value of $\nu_{\mathrm{HORIZONTAL}}$, was thus ~ 1600. The characteristic eddy circulation time L/U was $\sim 10^3$ sec. The time step, as prescribed by the Courant advection condition for a spectral scheme,

$$\frac{U\Delta t}{\Delta x} \leq \frac{1}{\pi}$$

was taken as 10 sec., which is a slightly conservative choice.

Figure 6.1A U Field (y-z projection), t =0

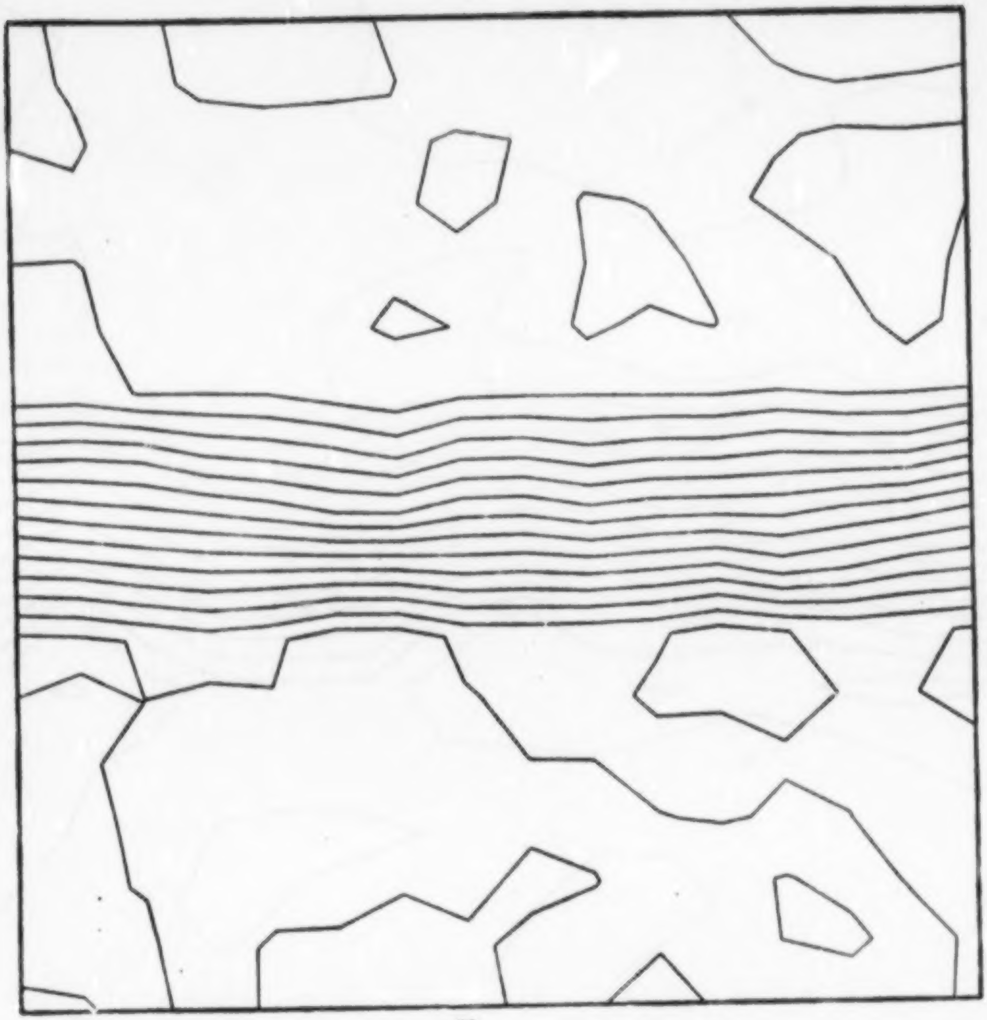

U_{min} = 5.4 m/sec

U_{max} = 10.2 m/sec

Contour Interval = 0.3 m/sec

Figure 6.1B U Field (y-z projection), $t = 10^3$ sec

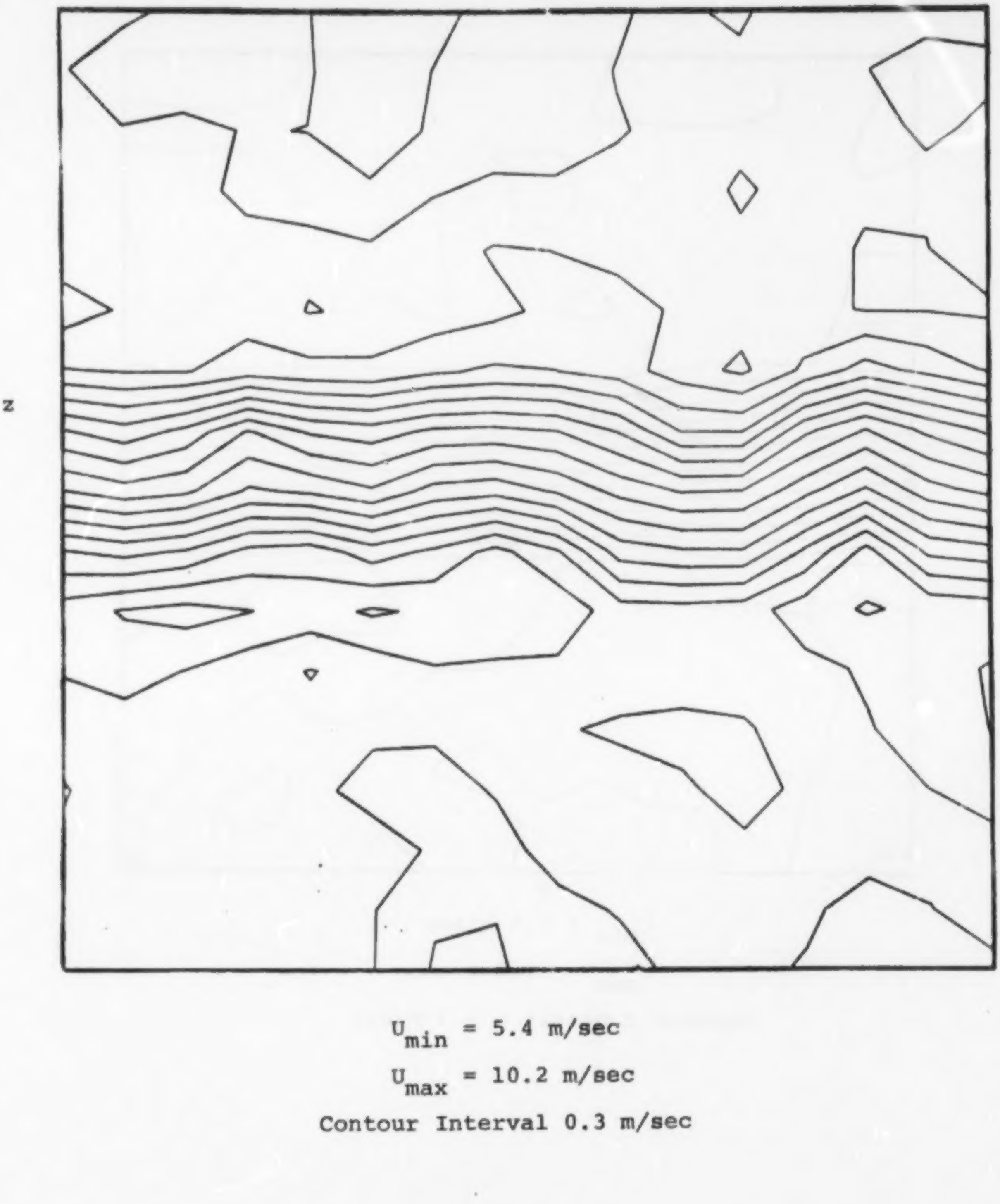

U_{min} = 5.4 m/sec

U_{max} = 10.2 m/sec

Contour Interval 0.3 m/sec

Figure 6.1c U Field (y-z projection), t = 2 x 10^3 sec

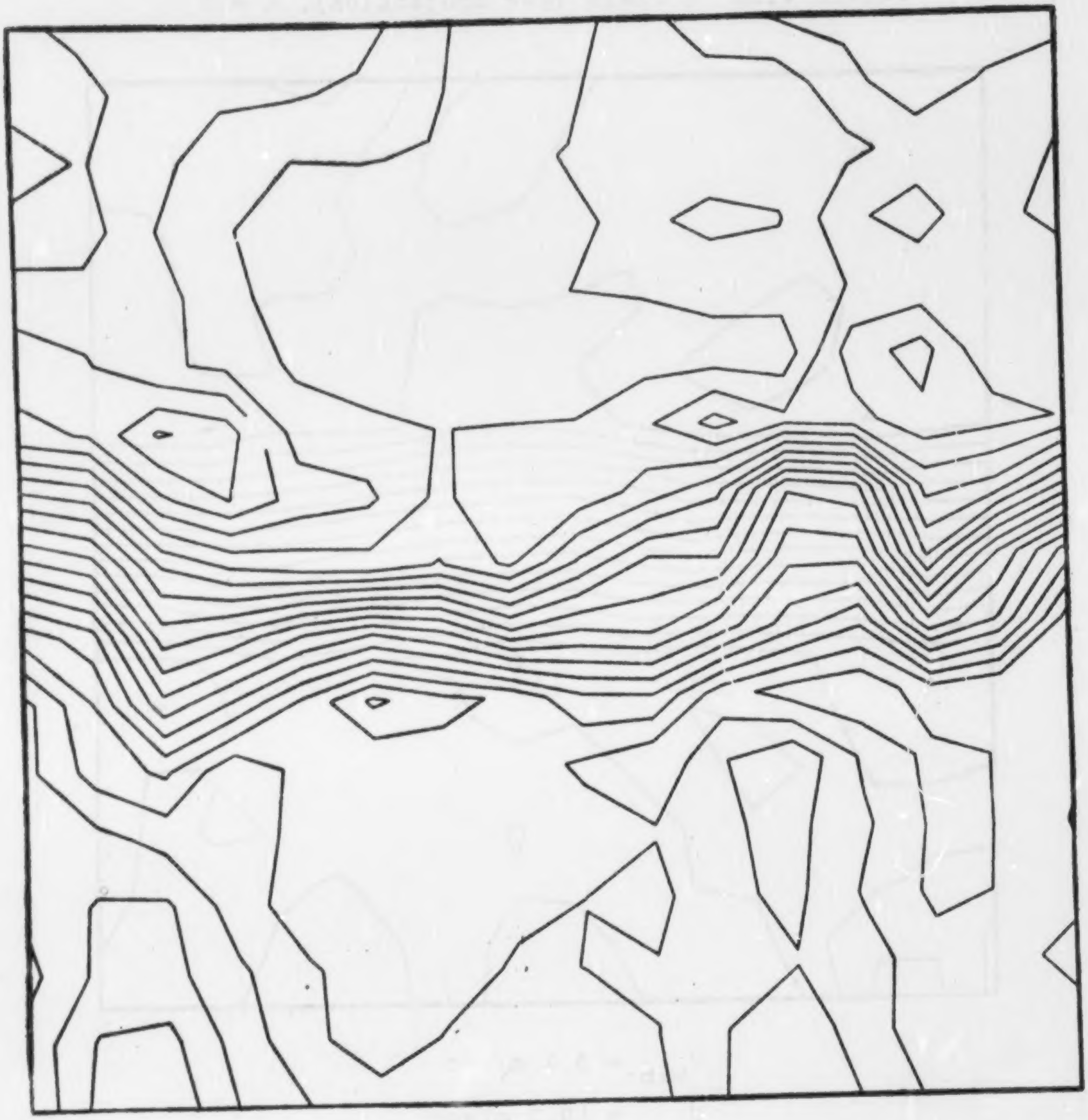

U_{min} = 4.8 m/sec

U_{max} = 10.8 m/sec

Contour Interval 0.3 m/sec

Figure 6.2A U Field (x-z projection), t = 0

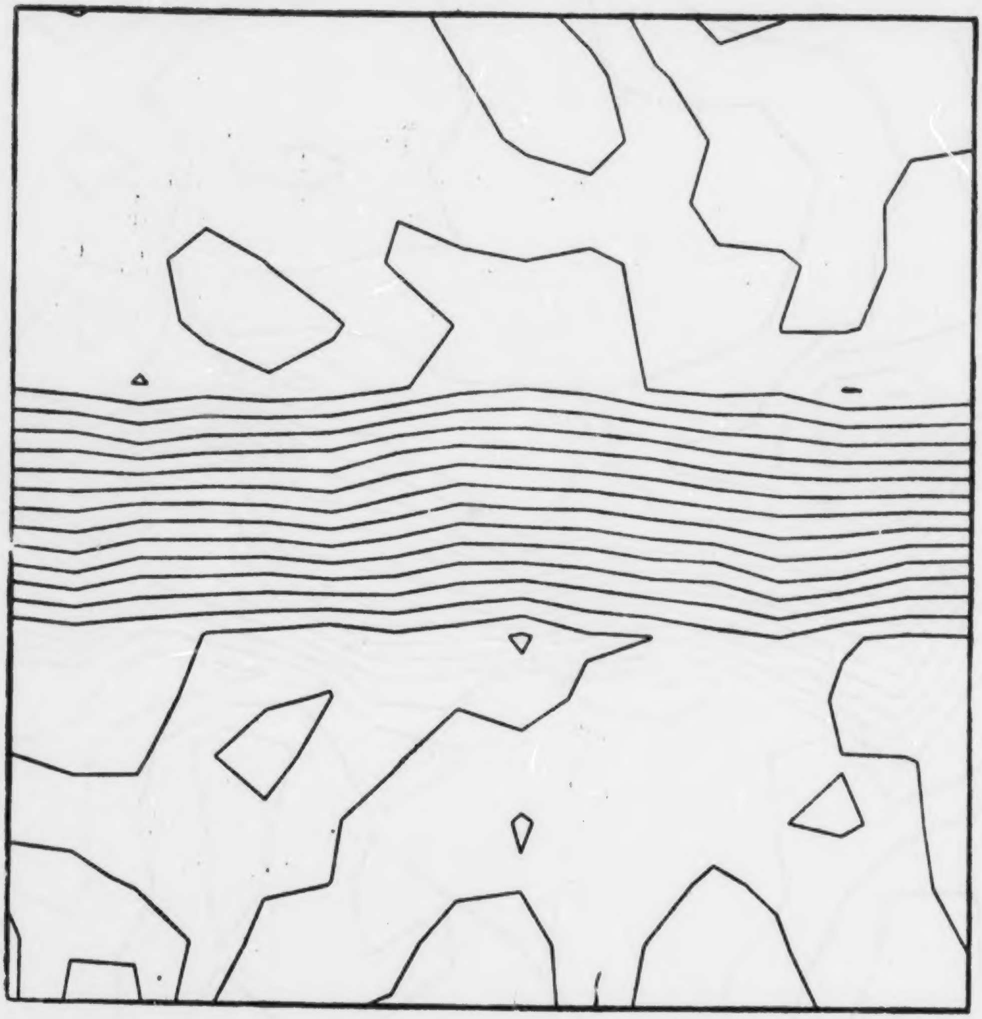

U_{min} = 5.1 m/sec

U_{max} = 10.2 m/sec

Contour Interval = 0.3 m/sec

Figure 6.2B U Field (x-z projection), $t = 10^3$ sec

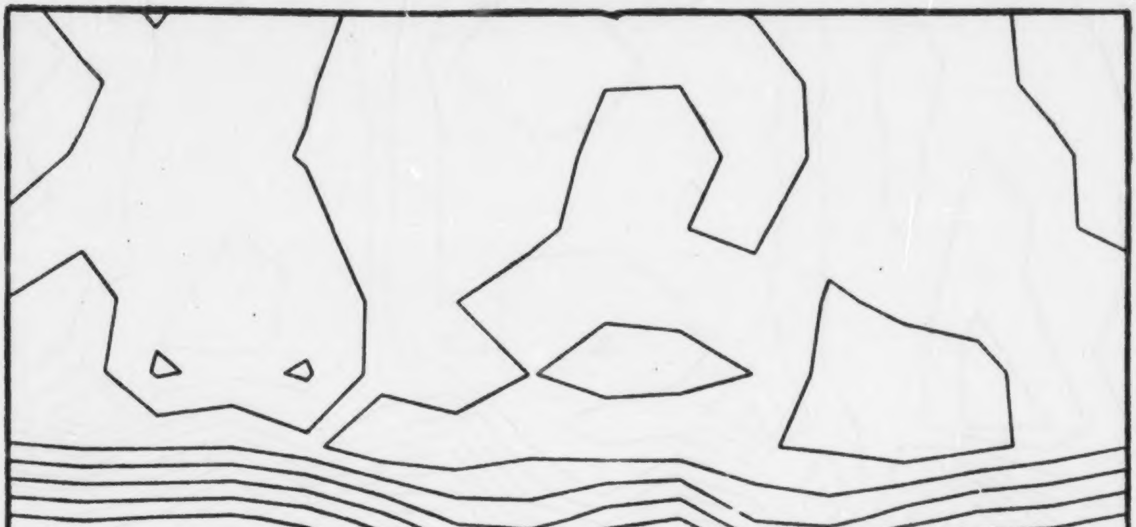

U_{min} = 5.1 m/sec

U_{max} = 10.2 m/sec

Contour Interval = 0.3 m/sec

Figure 6.2C U Field (x-z projection), t = 2 x 10^3 sec

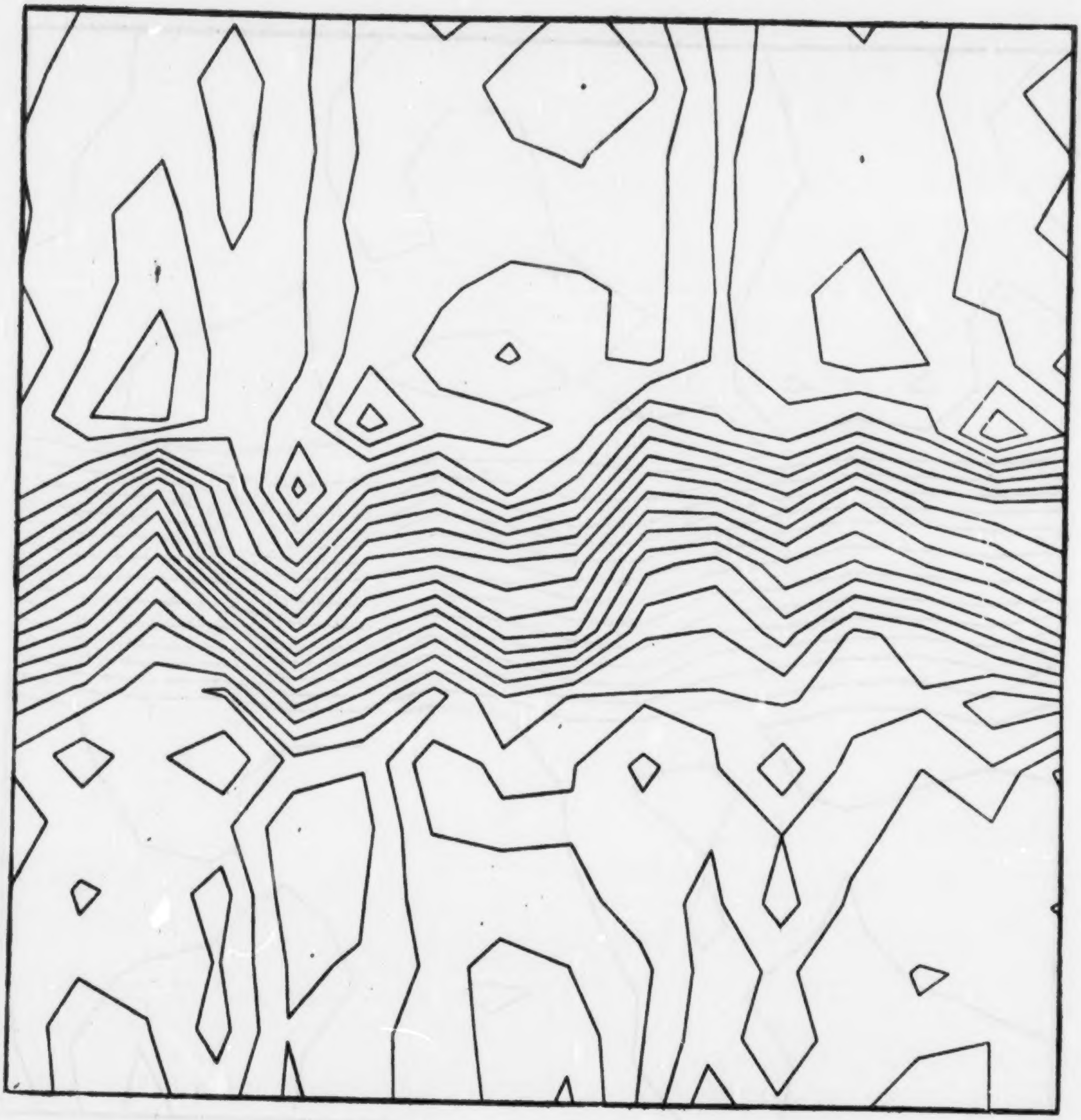

U_{min} = 5.1 m/sec

U_{max} = 10.8 m/sec

Contour Interval 0.3 m/sec

Figure 6.3A U Field (x-y projection), t = 0

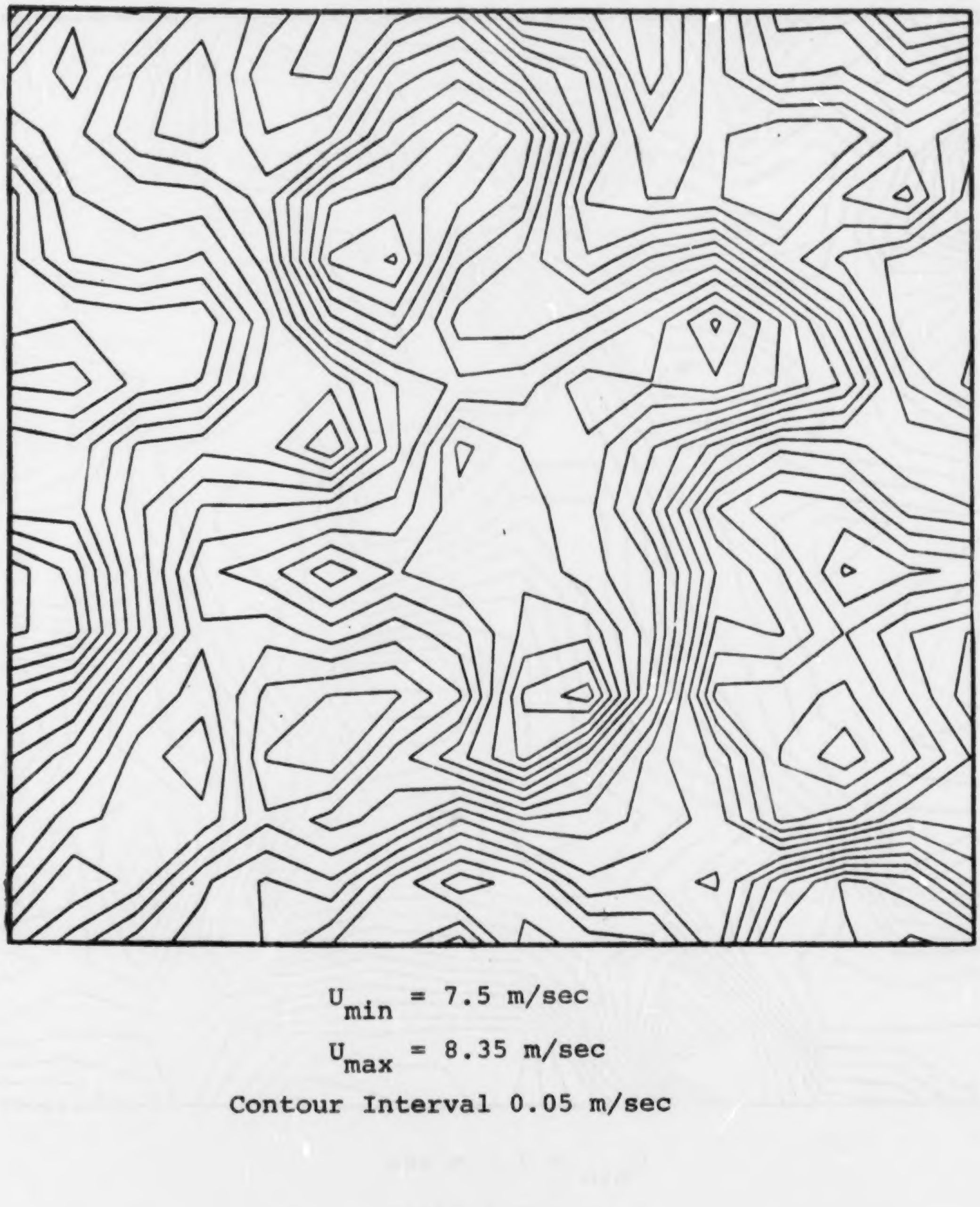

U_{min} = 7.5 m/sec

U_{max} = 8.35 m/sec

Contour Interval 0.05 m/sec

Figure 6.3B U Field (x-y projection), $t = 10^3$ sec

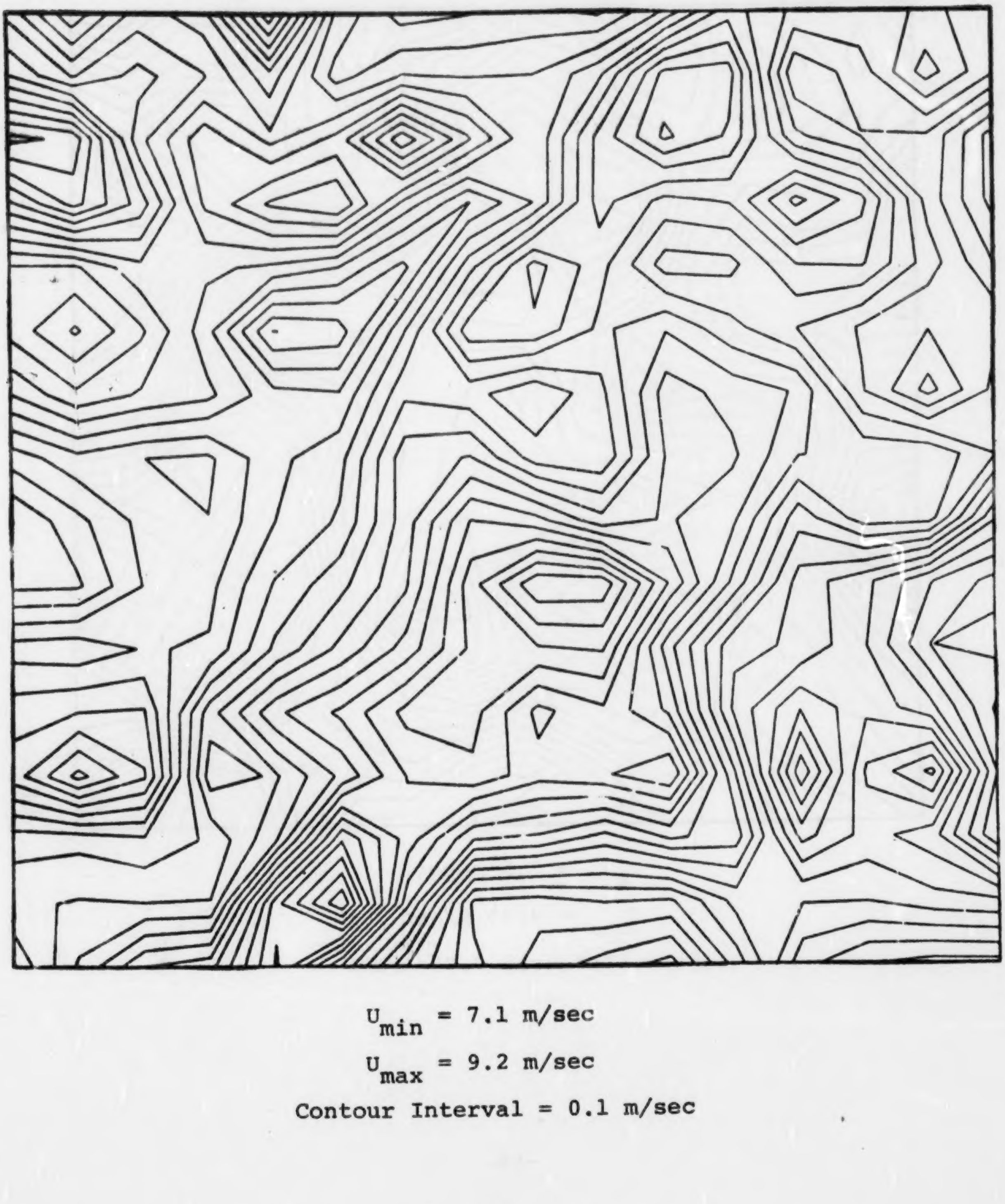

$U_{min} = 7.1$ m/sec

$U_{max} = 9.2$ m/sec

Contour Interval = 0.1 m/sec

Figure 6.3C U Field (x-y projection), $t = 2 \times 10^3$ sec

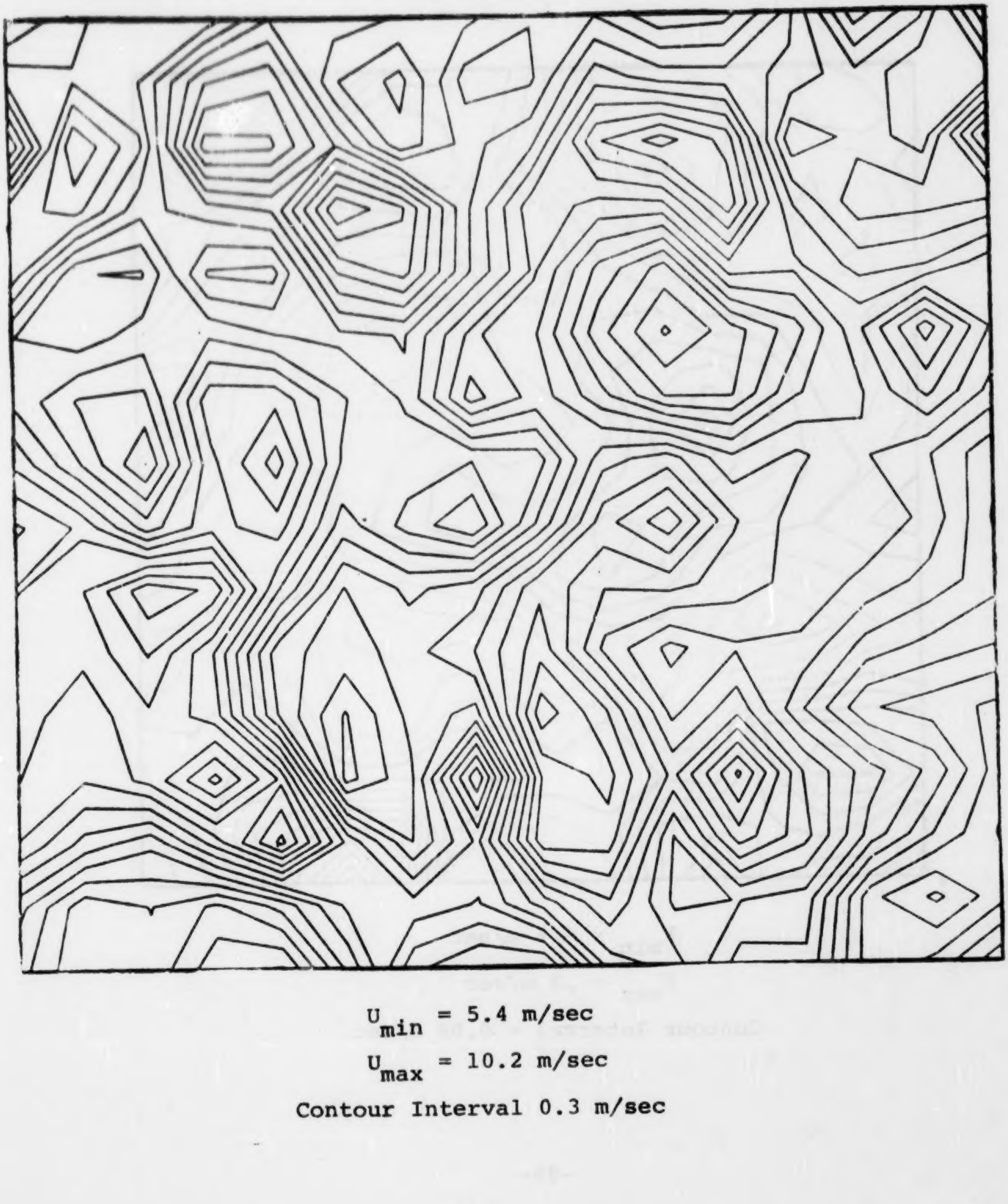

U_{min} = 5.4 m/sec

U_{max} = 10.2 m/sec

Contour Interval 0.3 m/sec

Figure 6.4A V Field (y-z projection), t = 0

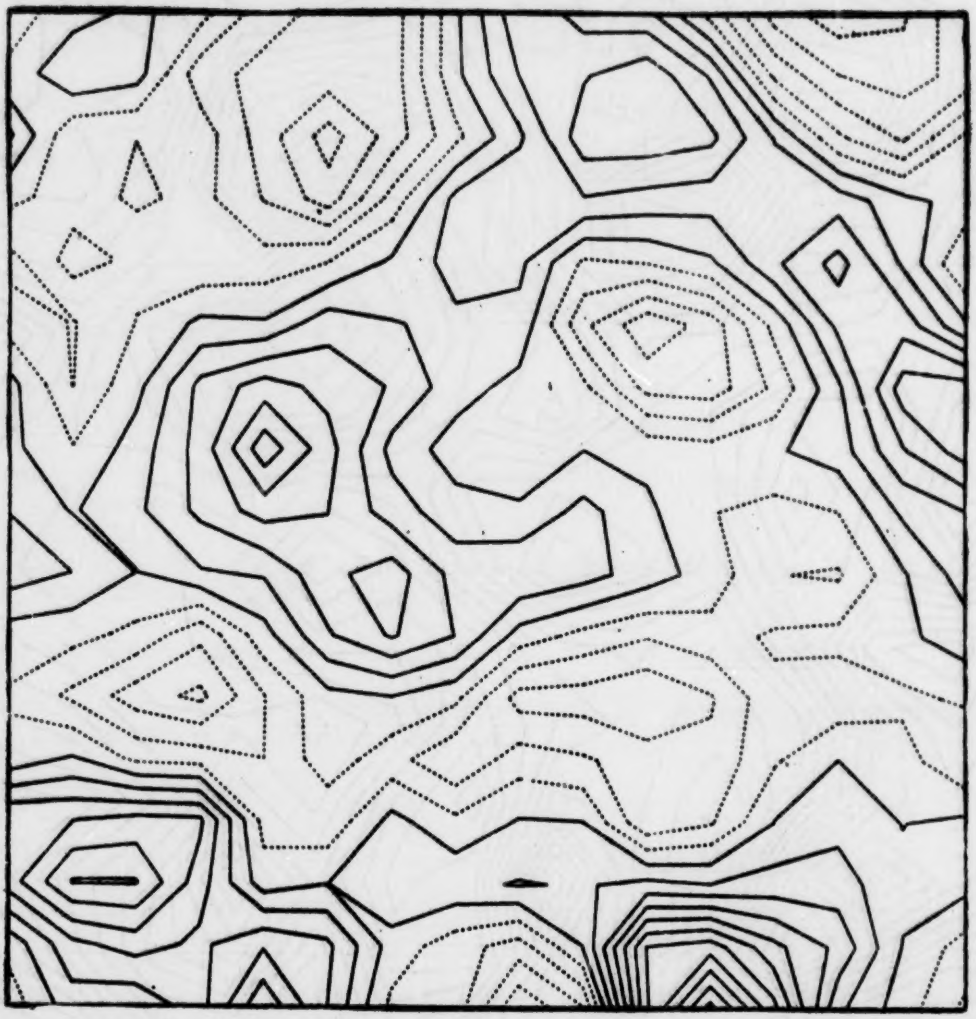

V_{min} = -.4 m/sec

V_{max} = .8 m/sec

Contour Interval = 0.08 m/sec

Figure 6.4B V Field (y-z projection), t = 10^3 sec

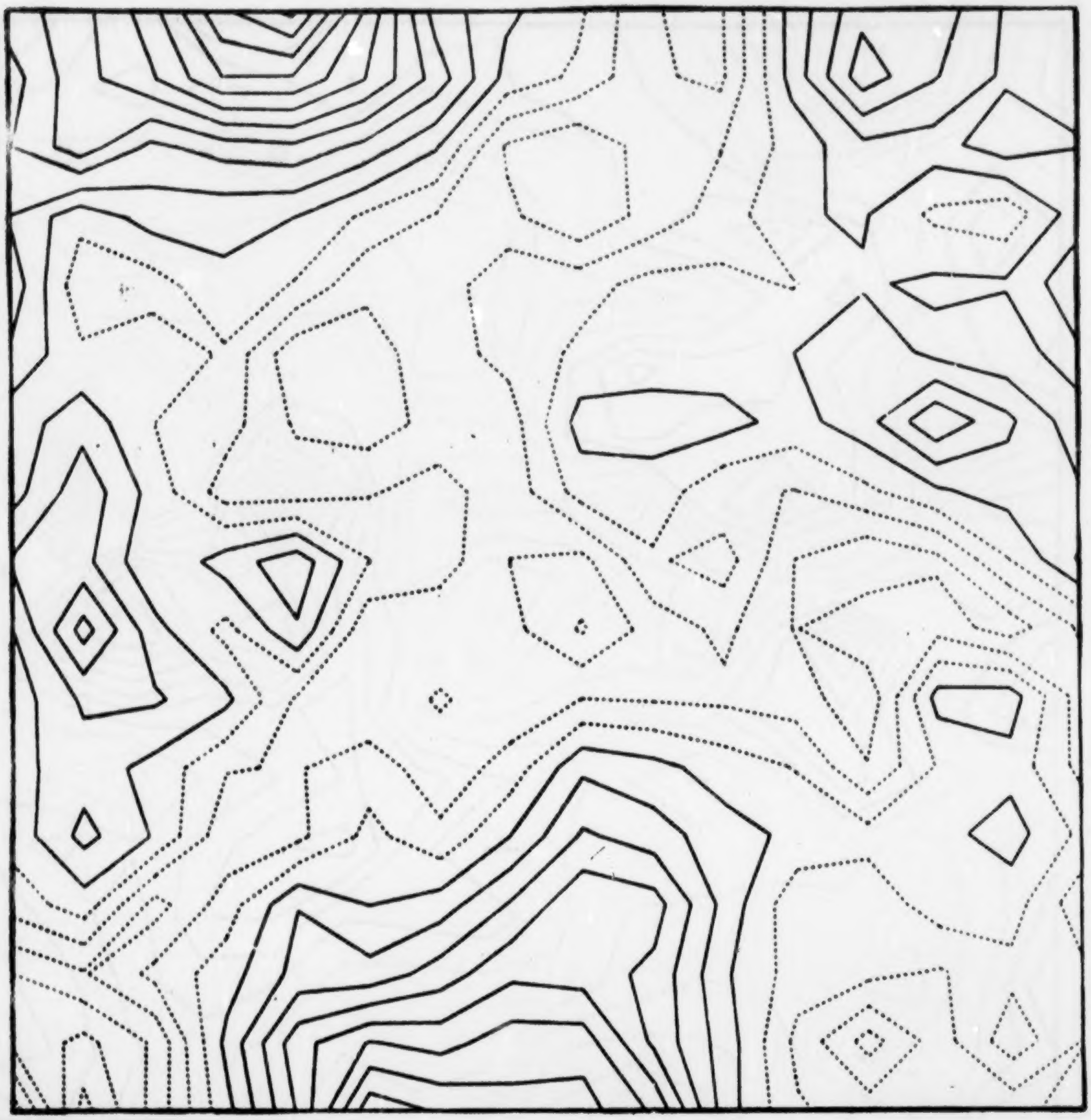

V_{min} = -.48 m/sec

V_{max} = .80 m/sec

Contour Interval = 0.08 m/sec

Figure 6.4C V Field (y-z projection), t = 2 x 10^3 sec

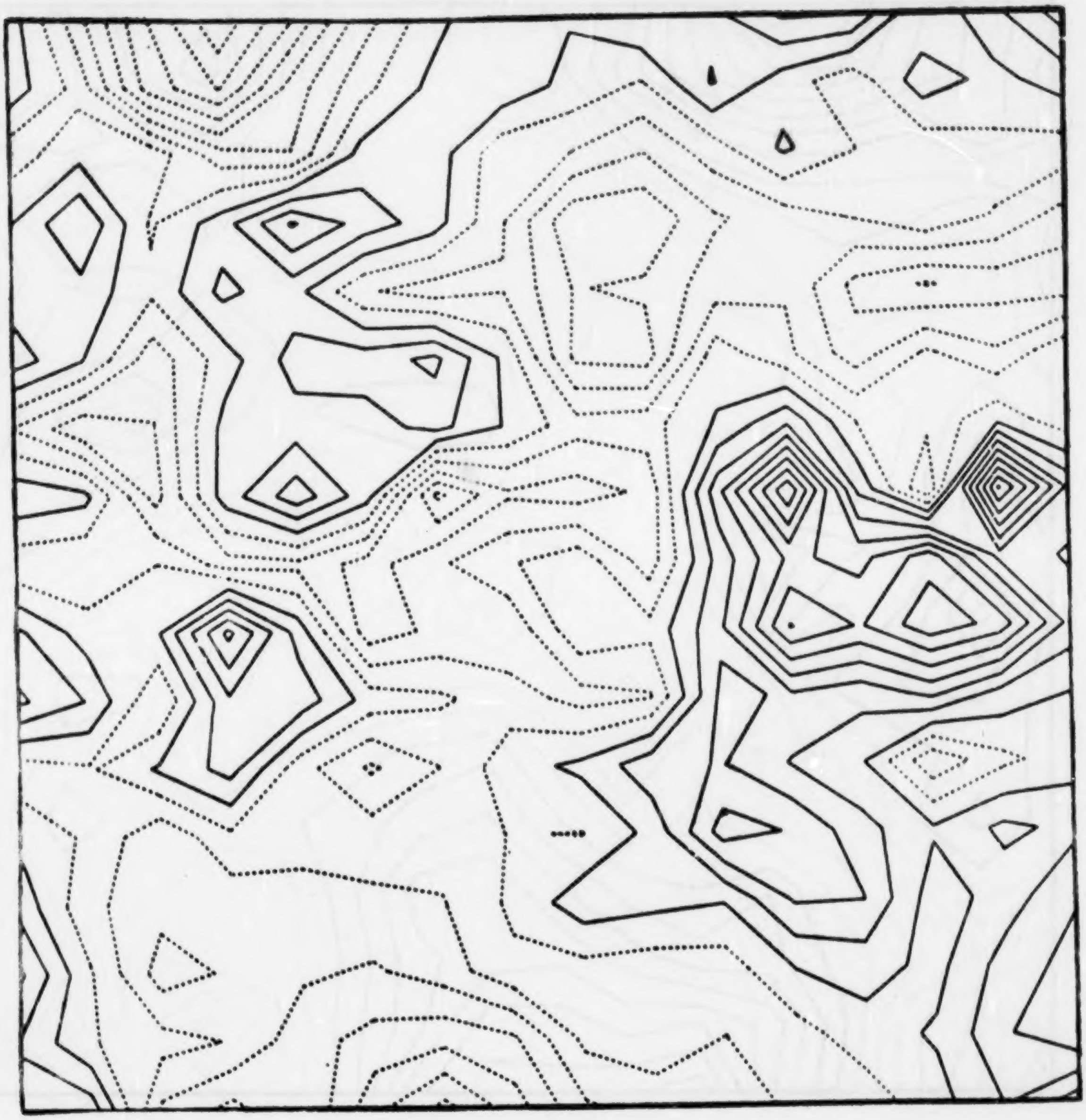

V_{min} = -.64 m/sec

V_{max} = .56 m/sec

Contour Interval 0.08 m/sec

Figure 6.5A W Field (y-z projection), t = 0

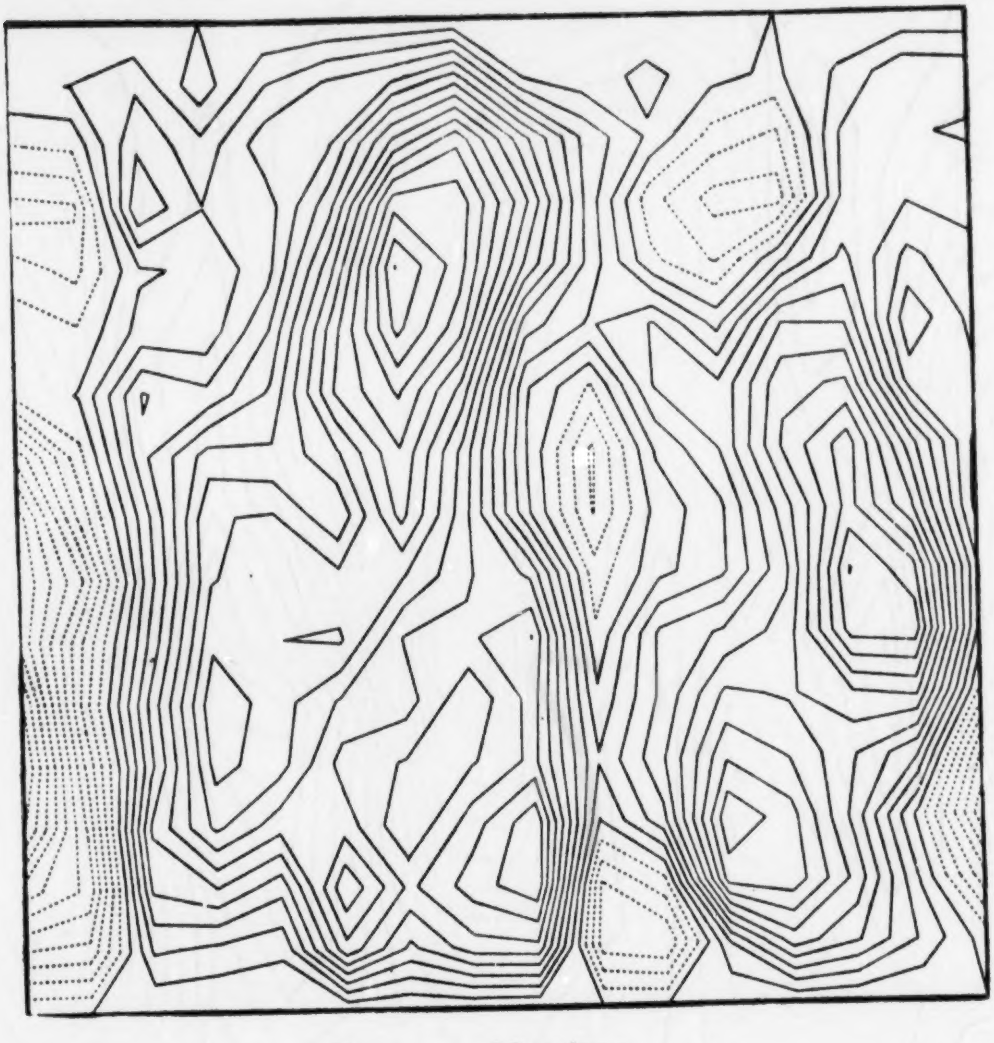

W_{min} = -.12 m/sec

W_{max} = .15 m/sec

Contour Interval = .01 m/sec

Figure 6.5B W Field (y-z projection), t = 10^3 sec

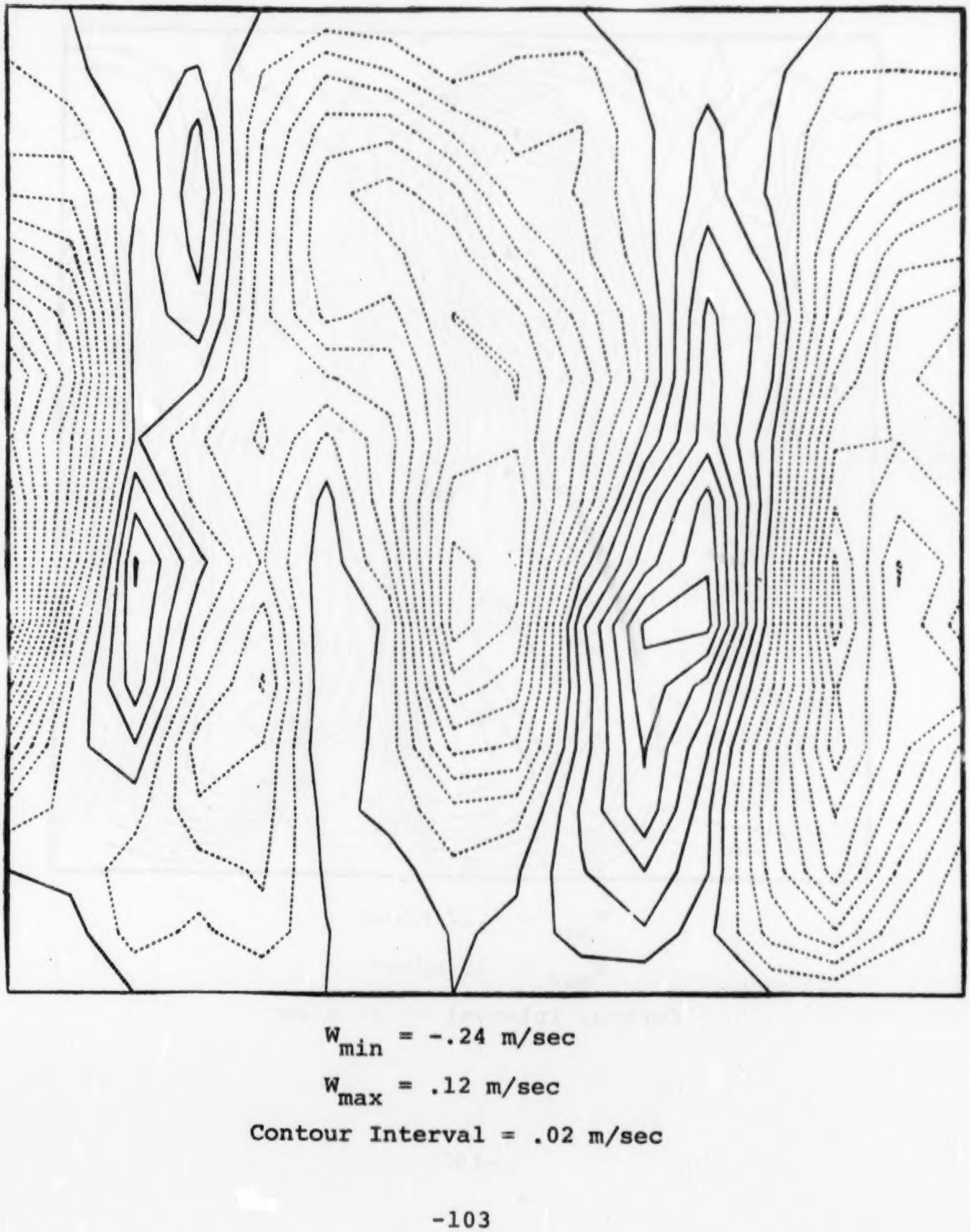

W_{min} = -.24 m/sec

W_{max} = .12 m/sec

Contour Interval = .02 m/sec

Figure 6.5C W Field (y-z projection), $t = 2 \times 10^3$ sec

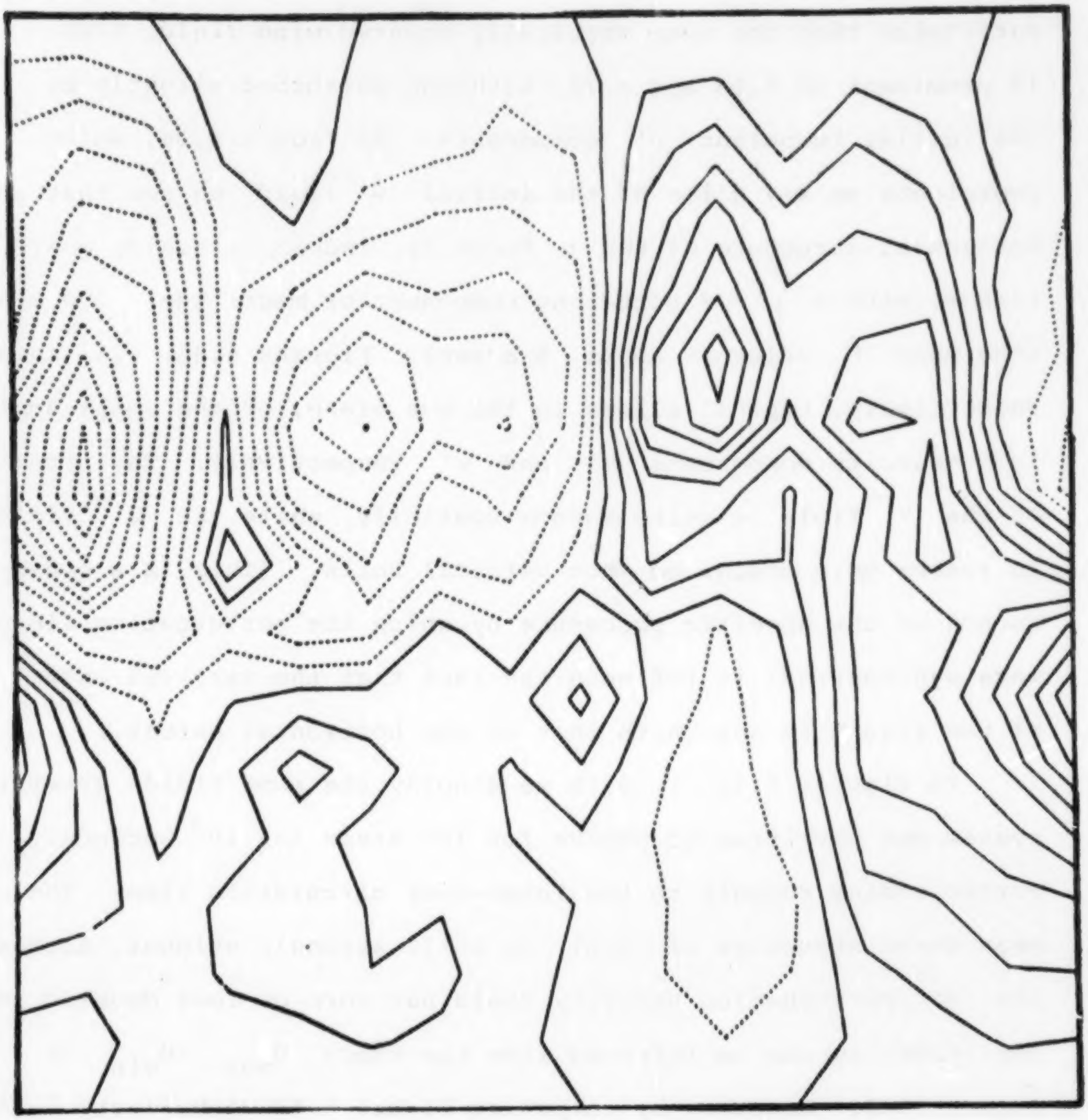

$W_{min} = -.30$ m/sec

$W_{max} = .27$ m/sec

Contour Interval .03 m/sec

The typical structure of the initial velocity fields is represented in figures 6.1A, 6.2A, 6.3A, 6.4A, 6.5A. Note in particular that the mean vertically sheared wind field $\bar{U}(z)$ is prominent in 6.1A and 6.2A, although perturbed slightly by the initial turbulent u' components. In figure 6.3A, which represents an x-y slice of the initial u field, we see that the horizontal structure of the u field is, indeed, initially quite random, with a μ' fluctuating component of magnitude 0.4 m/sec (the mean $\bar{U}$ value is about 8 m/sec). Figures 6.4A, 6.5A show, respectively, typical slices in the y-z plane, of the small-amplitude velocity components v' and w' respectively. The structure of the v' field is quite random spatially, while the w' field is rather more organized into vertical rolls. (This is a consequence of the specific procedure by which the perturbation fields were synthesized; it reflects the fact that the vertical extent of the system is one-tenth that of the horizontal extent.)

In figures 6.1B ... 6.5B we display the same fields after the system was permitted to evolve for 100 steps (or 10^3 seconds), corresponding roughly to the large-eddy circulation time. The mean shear structure of $\bar{U}(z)$ is still strongly evident, although the u' perturbation velocity field has more or less doubled in amplitude, as can be inferred from the range $U_{max} - U_{min}$ in figure 6.3B. However, by comparing figure 6.4B with figure 6.4A, and figure 6.5B with figure 6.5A, we see that the small-scale structure of the perturbation velocity fields v' and w' has been damped appreciably, which suggests that, in this experiment, turbulent energy is being dissipated at the higher wavenumbers more rapidly than it is being cascaded downscale by nonlinear exchange with low-wavenumber modes.

After another 100 times steps of evolution, the situation is worse yet. Although the perturbation velocity fields have roughly doubled again in magnitude, this growth is almost entirely at the very lowest wavenumbers as may best be seen in figures 6.1C and 6.5C.

Since, after two eddy circulation times, the turbulent velocity fields were clearly further from equilibrium than before, it was pointless to continue the time evolution of this experiment. We therefore started anew, in a second experiment, this time with ten-fold lesser viscosity. Although the decrease in viscosity tended to preserve relatively more of the small-scale structure, the growth of total perturbation energy was unrealistically rapid, and the contour plots showed the mean wind field was soon masked by the magnitude of the perturbation velocity fields. Alternatively, we also tried a ten-fold increase in viscosity, which resulted in a rather more constant magnitude of perturbation kinetic energy, but at the price of even stronger suppression of all but the very lowest harmonic components. After further experiments with somewhat difficult initial conditions, it was reluctantly concluded that, with the limited resolution and cpu time available, it would not be possible at this time to evolve a turbulent flow in reasonable equilibrium with the desired mean shear profile.

7.0 Relaxation of Anisotropic Turbulence to Isotropy

One of the critical parameters of turbulent transport models is the rate at which an initially non-isotropic flow decays to its asymptotic isotropic state. Return-to-isotropy terms appear explicitly, for example, in the turbulence closure model of Donaldson (1973) and that Lumley and Khajeh-Nouri (1973), in the form of the pressure-strain correlation expression

$$\overline{P'\left(\frac{\partial u'_i}{\partial x_k} + \frac{\partial u'_k}{\partial x_i}\right)}\ .$$

This represents, for incompressible flow, a redistribution of turbulent kinetic energy among the three velocity components. A variety of closure prescriptions have been given for this term. For example, Donaldson has chosen the Rotta model (Rotta, 1951)

$$\overline{P'\left(\frac{\partial u'_i}{\partial x_k} + \frac{\partial u'_k}{\partial x_i}\right)} = -\frac{\rho_0 q}{\lambda_1}\left(\overline{u_i'u'_k} - \frac{\delta_{ik} q^2}{3}\right)$$

where $q = (\overline{u'_i u'_i})^{1/2}$ is a scalar measure of the turbulent velocity field, λ_1 is a length scale introduced for dimensional consistency (and requires independent specification), and ρ_0 is the density.

Instead of specifying the rate of return to isotropy in ad-hoc fashion, one may have recourse to numerical simulation for an experimental measure of this parameter. It is important to use direct spectral methods to ensure high accuracy. To perform such a simulation, we require a fully three-dimensional closure-free Navier-Stokes model. The basic model described in section 6.1

serves especially well with the following minor modifications:

(a) the thermal and scalar concentration equations are ignored;

(b) the vertical boundary conditions are modified to permit general periodic symmetry conditions in the vertical (rather than the particular cosine-like or sine-like conditions previously specified).

To best examine the relaxation-to-isotropy process, it is useful to start from an axisymmetric turbulent flow, i.e., a turbulent three-dimensional flow field with one axis of symmetry. The initial flow conditions for such a relaxation problem may be constructed in the following manner. We begin from a velocity field $\underline{V}(\underline{x},t)$ which is statistically homogeneous and axially symmetric about an axis whose direction is described by the vector n. Suppose we define the second-order two-point moments of $\underline{V}$, namely:

$$\langle V_i(\underline{x},t)V_j(\underline{x}',t')\rangle = \Psi_{ij}(\underline{x},\underline{x}',t,t').$$

The Fourier transform of Ψ is given by

$$\Psi_{ij}(\underline{K},t,t') = \int \exp\{i\underline{K}\cdot(\underline{x}-\underline{x}')\Psi_{ij}(\underline{x},\underline{x}',t,t')d(\underline{x}-\underline{x}')\}.$$

For the axisymmetric case, this may be decomposed into

$$\begin{aligned}\Psi_{ij}(\underline{K},t,t') = {} & \phi^{(1)}(\underline{K},t,t')e_i^{(1)}(\underline{K})e_j^{(1)}(\underline{K}) \\ & + \phi^{(2)}(\underline{K},t,t')e_i^{(2)}(\underline{K})e_j^{(2)}(\underline{K})\end{aligned}$$

where the two vectors $\underline{e}^{(1)}$ and $\underline{e}^{(2)}$ are

$$\underline{e}^{(1)}(\underline{K}) = (\underline{K} \times \underline{n})/|\underline{K} \times \underline{n}|$$

$$\underline{e}^{(2)}(\underline{K}) = \underline{K} \times (\underline{K} \times \underline{n})/|\underline{K} \times (\underline{K} \times \underline{n})| .$$

Here, $\underline{e}^{(1)}$ is the direction transverse to the axis of symmetry, and $\underline{e}^{(2)}$ is orthogonal to both $\underline{K}$ and $\underline{e}^{(1)}$. The functions $\phi^{(1)}(\underline{K})$ and $\phi^{(2)}(\underline{K})$ are given by

$$\phi^{(1)}(\underline{K}) = <|(\underline{K} \times \underline{n})\cdot U(\underline{K})|^2>/|\underline{K} \times \underline{n}|^2$$

$$\phi^{(2)}(\underline{K}) = <|\underline{n}\cdot U(\underline{K})|^2>/|\underline{K} \times \underline{n}|^2$$

where $\underline{U}(\underline{K})$ is the Fourier transform of $\underline{V}(\underline{x})$. The function $\phi^{(1)}(\underline{K})$ represents the modal kinetic energy in the direction transverse to the symmetry axis $\underline{n}$, and $\phi^{(2)}(\underline{K})$ represents the modal kinetic energy in the direction orthogonal both to wave vector $\underline{K}$ and to $\underline{n}$. If the statistical properties of the initial velocity field are invariant to rotation about the symmetry axis, then $\phi^{(1)}(\underline{K})$ and $\phi^{(2)}(\underline{K})$ are invariant as well.

A useful 'experimental' measure of the rate of return to isotropy is provided by the non-dimensional parameter

$$R_a(t) = \frac{E(t)}{\varepsilon(t)} \quad \frac{\frac{d}{dt}\left|E_2(t) - E_1(t)\right|}{E_2(t) - E_1(t)}$$

where

$$E_1(t) = 2\pi\int_0^\infty dK\, K^2\phi^{(1)}(K,t)$$

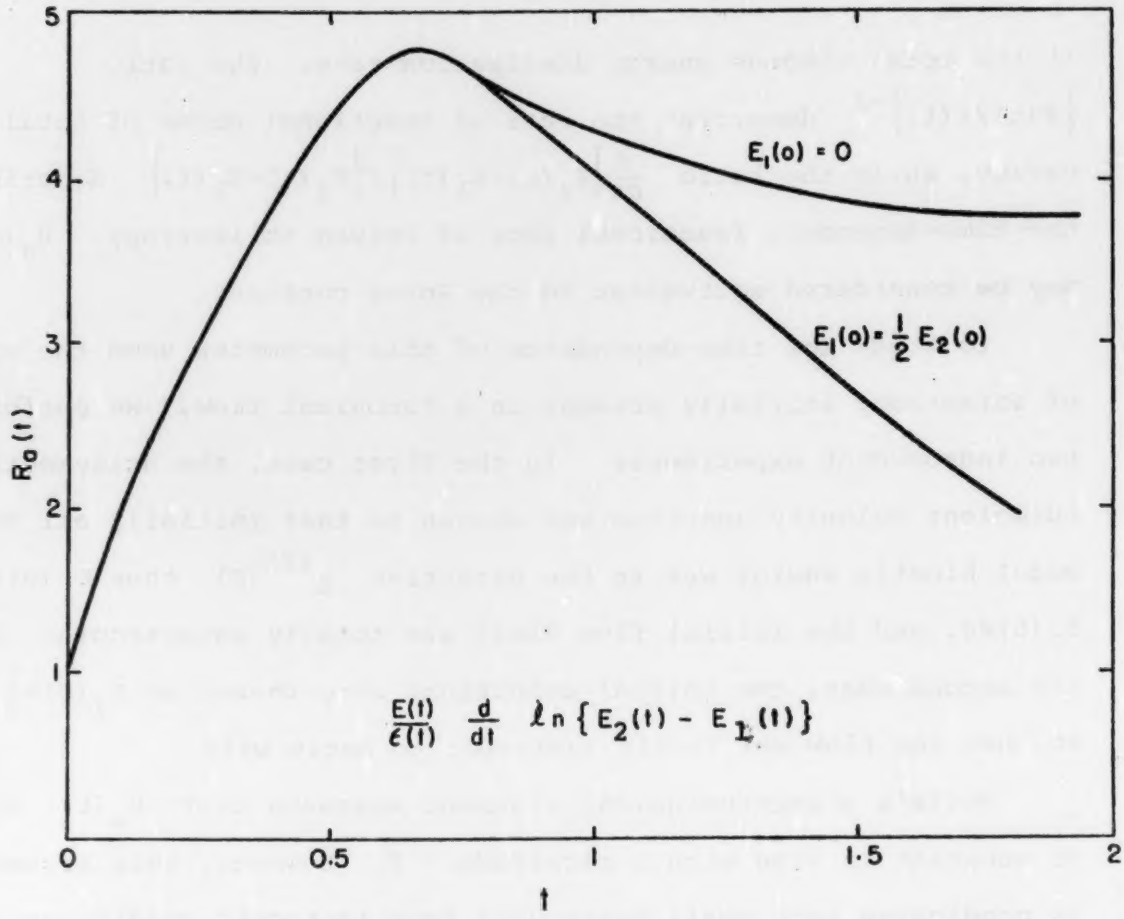

Figure 7.1 Time History of $R_a(t)$ for $E_1(0) = 0$ and $E_1(0) = 1/2\ E_2(0)$

$$E_2(t) = 2\pi \int_0^\infty dk\ K^2 \Phi^{(2)}(K,t)$$

represent the kinetic energies in the orthogonal directions $\underline{e}^{(1)}(\underline{K})$, $\underline{e}^{(2)}(K)$, respectively, $E(t) = E_1(t) + E_2(t)$ is the total kinetic energy, and

$$\varepsilon(t) = 4\pi^2 \int_0^\infty dk\ K^4 [\Phi^{(1)}(K,t) + \Phi^{(2)}(K,t)]$$

is the total viscous energy dissipation rate. The ratio $\left|E(t)/\varepsilon(t)\right|^{-1}$ describes the rate of fractional decay of total energy, while the ratio $\frac{d}{dt}\left|E_2(t)-E_1(t)\right| / \left|E_2(t)-E_1(t)\right|$ describes the time-dependent fractional rate of return to isotropy. $R_a(t)$ may be considered equivalent to the Rotta constant.

To study the time-dependence of this parameter upon the extent of anisotropy initially present in a turbulent flow, we performed two independent experiments. In the first case, the axisymmetric turbulent velocity spectrum was chosen so that initially all the modal kinetic energy was in the direction $\underline{e}^{(2)}(K)$, thus $E_1(0)=0$, $E_2(0)\neq 0$, and the initial flow field was totally anisotropic. In the second case, the initial conditions were chosen as $E_1(0)=\frac{1}{2}E_2(0)$, so that the flow was fairly isotropic to begin with.

Rotta's phenomenological argument suggests that $R_a(t)$ should be constant in time with a magnitude ~ 2. However, this argument is predicated upon small departures from isotropic conditions. It is interesting, therefore, to see how well this prediction holds for flows which are initially quite anisotropic. Figure 7.1 displays the time history of the expression $R_a(t)$ for each of the two cases studied (the time t is normalized by the large-eddy circulation time). Somewhat surprisingly, in view of Rotta's argument, we see that for the second case $E_1(0) = \frac{1}{2} E_2(0)$, which represents fairly isotropic initial conditions, the rate of return to isotropy is considerably less constant than that observed in the first case $E_1(0)=0$, which began with completely anisotropic initial structure. This is indicative of large statistical fluctuations in the first case, and suggests that even fairly isotropic turbulent flows remain in strong disequilibrium for long periods of time. That is, isotropic relaxation of turbulence is a very slow process. Thus, turbulence closure models which suppose self-similar asymptotic conditions are strongly suspect in this regard.

We may note, finally, that these numerical results are roughly consistent with calculations based upon the Direct Interaction Approximation turbulence theory of Kraichnan (Herring 1974).

8.0 Recommendations for Future Research

Although the primary research objective of direct turbulence simulations was not achieved in the current contract because of limited computer resources, we remain confident that the use of spectral methods holds considerable promise for operational improvement of air quality numerical modeling in a number of specific applications areas. These include:

(a) more accurate treatment of advection and viscous terms by means of spectral representations which preserve better than do finite-difference schemes the true phase and amplitude structure of such terms;

(b) accurate representation of the advection-diffusion of point-source and line-source pollutants, as suggested by the discussion in chapter 5;

(c) efficient spectral schemes for accurate representation of vertical structure and boundary layers, in particular the use of Chebyshev spectral methods to provide effectively increased resolution at viscous boundaries;

(d) the use of spectral methods, in conjunction with mapping techniques, for accurate treatment of topography, as, for example, the modeling of pollutant advection-diffusion from a highway situated in a valley;

(e) the use of spectral methods for the accurate simulation of lateral inflow and outflow boundary conditions, without requiring the imposition of ad-hoc one-sided differencing schemes.

We recommend, therefore, that careful investigation be made of the prospective benefits to be gained by implementation of these spectral methods within existing air-quality models of importance to EPA, in particular, the photochemical air-pollution model developed at Systems Applications, Inc., and the air-pollution model developed at IBM.

As to the problem of simulating the turbulent diffusion of passive contaminants in fully three-dimensional turbulent sheared flows by the direct spectral approach of the current effort, we do not recommend further pursuit of this study at present for two reasons.

The first of these concerns the timeliness of application of this research. It does not appear likely that extension of the present study would provide to EPA, in the near term, the capability for better estimation of eddy Austauch coefficients for turbulent diffusion of pollutants in the place of field observations. We do believe, however, that the prospects for success of a longer-term research effort remain very good. We do not know of any fundamental theoretical impediments to the successful numerical simulation of such turbulent flows by direct spectral methods, especially in the light of previous recognized achievements in this area by Orszag and collaborators.

The second reason concerns the prohibitive economics of the required calculations. Neither the computer core time necessary for adequate spectral resolution, nor the computer time required to establish realistic turbulent dynamics, will be available to us in the near future. At present, such calculational efforts can possibly only be undertaken by university-affiliated groups with access to the NCAR computer facility or a comparable installation. When the computing-resource situation improves, as may be anticipated, it would be most worthwhile, we believe, to pursue this study anew.

9.0 References

Arakawa, A. (1966) *J. Comp. Phys.* *1*, 119-143.

Arakawa, A. (1970) *Numerical Solution of Field Problems in Continuum Physics* 24, American Mathematical Society, Providence, R.I.

Bourke, W. (1972) *Mon. Weath. Rev.* *100*, 683-689.

Calder, K. L. (1967) *QJRMS*, 88-92.

Collatz, L. (1960) *Numerical Treatment of Differential Equations*, Springer-Verlag, Berlin.

Cooley, J. W. and Tukey, J. W. (1965) *Math. Comp.* *19*, 297-301.

Crowley, W. P. (1968) *Mon. Weath. Rev.* 96, 1-11.

Cunnold, D., Alyea, F., Phillips, N. and Prinn, R. (1975) *J.A.S.* *32*, 123.

Deardorff, J. W. (1970) *J. Fluid Mech.* *41*, 453.

Donaldson, C. duP. (1973) "Atmospheric Turbulence and the Dispersal of Atmospheric Pollutants," EPA report EPA-R4-73-016a.

Dorr, F. W. (1970) *SIAM Rev.* *12*, 248.

Eliassen, E., Machaver, B. and Rasmussen, E. (1970) "On a Numerical Method for Integration of the Hydrodynamical Equations with a Spectral Representation of the Horizontal Fields," Institute for Teoretisic Meteorologi, Univ. of Copenhagen, Report No. 2.

Fornberg, B. (1972) "On High Order Approximations of Hyperbolic Partial Differential Equations by a Fourier Method." Dept. of Computer Sciences, Uppsala Univ. Sweden, Report No. 39.

Fox, L., and Parker, J. B. (1968) *Chebyshev Polynomials in Numerical Analysis*, Oxford Univ. Press, Oxford

Fromm, J. E. (1963) *"A Method for Computing Nonsteady Incompressible Viscous Fluid Flows,"* Los Alamos Scientific Laboratory, Report LA-2910.

Fromm, J. E. (1970) *An Introduction to Computer Simulation in Applied Science*, ed., F. F. Abraham, W. A. Tiller, IBM Data Processing Division, Palo, Alto, Calif.

GARP (1974) "The GARP Programme on Numerical Experimentation," Report of the Int. Symp. on Spectral Methods in Report No. 7, Copenhagen.

Gentleman, W. M. and Sande, G. (1966) Proc. Fall Joint Computer Conference, 1966, 563-578.

Gordon, A. and Stern, W. (1974) "Spectral Modelling at GFDL," on GARP (1974) (see above).

Grammeltvedt, A. (1969) Mon. Weath. Rev. 97, 384.

Harlow, F. H. and Welch, J. E. (1965) Phys. Fluids 8, 2182.

Herring, J. R. (1974) Phys. Fluids 17, 859-872.

Herring, J. R., Orszag, S. A. Kraichnan, R. H. and Fox, D. G., (1974) J. Fluid Mech. 66, 417-444.

Hockney, R. W. (1970) Methods in Computational Physics 9, 135.

Israeli, M. (1971) "Time Dependent Motions of Confined Rotating Fluids," PhD. Thesis, Dept. of Applied Mathematics, M.I.T., Cambridge, MA.

Kreiss, H. O. and Oliger, J. (1972) Tellus 24, 199.

Kreiss, H. O. and Oliger, S. (1973), Methods for the Approximate Solution of Time Dependent Problems, GARP Publication Series No. 10, WMO, Geneva.

Lanczos, C. (1956) Applied Analysis, Prentice Hall Pub. Co., Englewood, N.J.

Lilly, D. K. (1965) Mon. Weath. Rev. 93, 11.

Lumley, J. L. and Khajeh-Nouri, B. (1973) "Computational Modeling of Turbulent Transport," Proc. Second IUGG-IUTAM Symp. on Atmoshperic Diffusion on Environmental Pollution, Academic Press, N.Y.

Merilees, P. E. (1973) Atmosphere 11, 13-20, (1974) Mon. Weath. Rev. 102, 82-84.

Metcalfe, R. W. (1973) "Spectral Methods for Boundary Value Problems in Fluid Dynamics," PhD. Thesis, M.I.T. Cambridge MA.

Molenkamp, C. R. (1968) J.A.M. 7, 160-167.

Neuringer, J. L. (1968) SIAM J. Appl. Math 16, 4.

Orszag, S. A. (1969) Phys. Fluids (Suppl. 2) 12, 250.

Orszag, S. A. (1971a) Stud. in Applied Math 50, 293.

Orszag, S. A. (1971b) J. Fluid Mech. 49, 75

Orszag, S. A. (1971c) Stud. in Applied Math 50, 395.

Orszag, S. A. (1971d) Phys. Rev. Letters 26, 1100.

Orszag, S. A. (1971e) J. Fluid Mech. 50, 689.

Orszag, S. A. (1972) Stud. in Applied Math 51, 253.

Orszag, S. A. and Israeli, M. (1974) Ann. Rev. Fluid Mech. 6, 281.

Orszag, S. A. and Pao, Y. H. (1974) "Numerical Computation of Turbulent Shear Flows," Advances on Geophysics 18A, Academic Press, Inc., NYC 225-236.

Orszag, S. A. and Patterson, G. S. (1972) Statistical Models and Turbulence, ed. Rosenblatt, Springer-Verlag, Berlin, 127.

Patterson, G. S. and Orszag, S. A. (1971) Phys. Fluids 14, 2538-2541.

Phillips, N. A. (1959) The Atmosphere and the Sea in Motion. Rockefeller Institute Press, NYC.

Piacsek, S. A. and Williams, G. P. (1970) J. Comp. Phys. 6, 392.

Roache, P. J. (1972) Computational Fluid Dynamics, Hermosa Publishers, Albuquerque, NM.

Rotta, J. C. (1951) Z. Phys. 129, 547.

Spiegel, E. A. and Veronis, G. (1960) Astrophys. J. 131, 442-447.

Swartztrauber, P. (1972) A Direct Method for the Discrete Solution of Separable Elliptic Equations (unpublished).

Williams, G. P., (1969) J. Fluid Mech. 37, 727.

Appendix 1

The Data Content of Discrete-Grid Representations

It is conventional practice, in the numerical solution of many fluid motion problems, to perform such calculations with respect to a discrete spatial grid and suitably spatially discretized versions of the governing differential equations whether by finite-difference of finite-spectral methods. In this section, we discuss the underlying assumptions and limitations which inhere to the discretization method.

Imagine that we wish to estimate the frequency spectrum of a continuous spatial waveform, $f(x)$, which is periodic with wavelength L. A harmonic analysis of this waveform might be performed as follows:

(1) partition the interval L into N equal segments by the discrete points $x_p = p\Delta x$ $(p=0, \ldots N-1)$; $\Delta x = L/N$, where for convenience, N is a power of 2);

(2) tabulate the string of values $f(x_p)$ at each of these points;

(3) employ the Discrete Fourier Transform algorithm (Appendix 2) to compute the Fourier modes $g(\lambda_q)$ corresponding to the discrete wavenumbers

$$\lambda_q = \frac{2\pi q}{N\Delta x} \quad q=0,\ 1,\ \ldots\ N/2\ .$$

Note that there is an upper wavenumber cutoff (the "folding" or Nyquist, frequency N/2) so that we possess no data whatever about harmonic components higher than $q = \pm N/2$. If we now attempt to reconstruct the waveform $f(x)$ by inverse discrete Fourier transform upon the truncated set of modes $g(\lambda_q)$, $q=0, \ldots \frac{N}{2}$, the only data recoverable about the spatial behavior of $f(x)$ is precisely its values at just the discrete points x_p $(p=0, \ldots N-1)$. That is, the data content of the truncated discrete spectral representation of the waveform is precisely equivalent to that contained in the N distinct functional values $f(x_p)$; $p=0, \ldots N-1$. Therefore, the spectral representation of this data contains precisely N distinct degrees of freedom. To see why this is so, consider the Fourier series representation of a real function periodic with fundamental wavelength L, sampled at the uniformly spaced points x_p $(p=0, \ldots N-1)$, viz:

$$f(x_p) = a_0 + \sum_{q=1} \left(a_q \cos\frac{2\pi pq}{L} + b_q \sin\frac{2\pi pq}{L}\right) .$$

If this system of equations is to be uniquely soluble for the set of Fourier coefficients a's and b's, then we can only specify a total of N Fourier coefficients. The most general choice of coefficients which are determinable for the data string $f(x_0)$, $\ldots f(x_{N-1})$ in the absense of any additional information about the function f, is precisely the set

$$a_0, a_1, b_1, a_2, b_2 \ldots . a_{(\frac{N}{2}-1)}, b_{(\frac{N}{2}-1)}, a_{\frac{N}{2}} .$$

Note that the discrete Fourier representation of the function incorporates exactly as much data about the spatial structure of the function $f(x)$ as does the discrete string $f(x_p) \ldots$.

How then do we interpret the correspondence between a real physical variable which is a continuous spatial function and its point-wise representation in a discrete-grid numerical model? One approach is to assume that the physical variable is sufficiently smoothly varying; that is, its assigned value at a discrete point x_0 is representative of its behavior over some neighborhood $x-x_0$ of the point in question, although the notion of neighborhood is not made precise. In fact, for highly discontinuous processes, as, for example, in the propagation of shocks, or small-scale turbulent cascade processes such an assumption is extremely dangerous. A more satisfactory approach is to consider the discrete-point representation as only a "best-fit" to the data contained within the numerically resolvable scales of the variable. The finite cutoff wavelength forces us to surrender any detailed data about small-scale structure which cannot be determined entirely from the resolvable larger scales. This interpretation does not require a notion of smoothness.

Appendix 2

Discrete Fourier Transform Representations

The bulk of the computational effort in the model we have developed is expended in performing discrete Fourier transforms from discrete three-dimensional real space to discrete three-dimensional wave space, and vice versa, using the Fast Fourier Transform (FFT) as discussed in Appendix 4. In this appendix the discussion is limited only to the discrete three-dimensional Fourier transform. The discrete three-dimensional Fourier transform pair is defined as follows:

Let f_{J_1, J_2, J_3} be a three-dimensional field defined over the $N_1 \times N_2 \times N_3$ real-space grid:

$$(x_1, x_2, x_3) = (J_1\Delta x \;\; J_2\Delta x \;\; J_3\Delta x) \qquad \begin{array}{l} J_1=1, \ldots N_1 \\ J_2=1, \ldots N_2 \\ J_3=1, \ldots N_3. \end{array}$$

Let $\tilde{F}_{K_1, K_2, K_3}$ be a three-dimensional field defined over the $N_1 \times N_2 \times N_3$ discrete wave-space grid

$$(k_1, k_2, k_3) = (K_1\Delta k, K_2\Delta k, K_3\Delta k) \qquad \begin{array}{l} K_1=1, \ldots N_1 \\ K_2=1, \ldots N_2 \\ K_3=1, \ldots N_3. \end{array}$$

Then f_{J_1, J_2, J_3} and $\tilde{F}_{K_1, K_2, K_3}$ are a discrete Fourier transform pair if (with one choice of normalization)

$$\text{(A2.1)} \quad \tilde{F}_{K_1, K_2, K_3} = \frac{1}{N_1N_2N_3} \sum_{J_1=1}^{N_1} \sum_{J_2=1}^{N_2} \sum_{J_3=1}^{N_3} e^{-2\pi i \left\{ \frac{(J_1-1)(K_1-1)}{N_1} \right.}$$

(cont'd)

(A2.1)
(cont'd)

$$+ \frac{(J_2-1)(K_2-1)}{N_2} + \frac{(J_3-1)(K_3-1)}{N_3} \Bigg\} f_{J_1,\ J_2,\ J_3}$$

(A2.2)

$$f_{J_1, J_2, J_3} = \sum_{K_1'=1}^{N_1} \sum_{K_2'=1}^{N_2} \sum_{K_3'=1}^{N_3} e^{+2\pi i \Bigg\{ \frac{(K_1'-1)(J_1-1)}{N_1} + \frac{(K_2'-1)(J_2-1)}{N_2} + \frac{(K_3'-1)(J_3'-1)}{N_3} \Bigg\}} \tilde{F}_{K_1',\ K_2',\ K_3'} .$$

The basis functions are orthogonal in the sense

$$\sum_{J_\alpha=1}^{N_\alpha} e^{\pm 2\pi i \frac{(J_\alpha-1)(K_\alpha-K_\alpha')}{N_\alpha}} = N_\alpha \delta_{N_\alpha}(K_\alpha, K_\alpha') \qquad (\alpha=1,2,3)$$

$$\sum_{K_\beta=1}^{N_\beta} e^{\pm 2\pi i \frac{(K_\beta-1)(J_\beta-J_\beta')}{N_\beta}} = N_\beta \delta_{N_\beta}(J_\beta,\ J_\beta') \qquad (\beta=1,2,3)$$

where

$$\delta_N\ (K,K') = \begin{cases} 1, & \text{for modulo}[(K-K'),N]=0 \\ 0, & \text{otherwise} \end{cases} ,$$ i.e., the Kronecker delta function, modulo N.

Writing the functions in vectorial form

$\underline{J} = (J_1,\ J_2,\ J_3)$

$\underline{K} = (K_1,\ K_2,\ K_3)$,

we have

$$\sum_{\underline{J}} e^{2\pi i\,\underline{J}\cdot(\underline{K}-\underline{K}')} = N_1\,N_2\,N_3\delta_N(\underline{K},\underline{K}')$$

If f_{J_1,J_2,J_3} is a real array, then $\tilde{F}_{K_1,K_2,K_3}$ is a conjugate-symmetric array (the conjugate symmetry being denoted by a star)

$$\tilde{F}_{K_1,K_2,K_3} = \left[\tilde{F}_{K_1',\,K_2',\,K_3'}\right]^* \text{ , where}$$

$$\left\{\begin{array}{l} K_i'=1 \quad \text{if} \quad K_i=1 \\ K_i'=(N_i+2-K_i) \quad \text{if} \quad K_i>1 \end{array}\right\} .$$

Noting that the wave-space coordinates K_i $(i=1,2,3)$ are indexed relative to one rather than zero and folded relative to the Nyquist frequency $N/2$, the following table provides the correspondence between the computational wave-space coordinate K_i of the algorithm and the associated non-dimensional physical wavenumber:

K_i of DFT algorithm	corresponding physical wavenumber
1	0
2	1
.	.
.	.
N/2	N/2-1
N/2 + 1	N/2
N/2 + 2	-(N/2 -1)
.	.
.	.
N	-1

Appendix 3

Elimination of Aliasing in Discrete Real-Space Multiplications

This appendix describes, in a simplified two-dimensional context, the algorithm developed by Orszag (1971a) for the efficient alias-free evaluation of real-space products. In order to help the reader become fully familiar with such techniques, we have included all relevant mathematical details.

Let us define the two-dimensional real-space grid (X_{J_1}, Y_{J_2}) for $0 \leq J_1, J_2 \leq N-1$; that is, $X_{J_1} = J_1 \Delta x$, $Y_{J_2} = J_2 \Delta y$, $\Delta y = \Delta x$. For compactness we will use the vector notation $\underline{J} = (J_1, J_2)$. Similarly, we define the two-dimensional wave-space grid $\underline{K} = (k_1, k_2)$, where $-\frac{N}{2} \leq k_1, k_2 < \frac{N}{2}$. These are equivalent to the notation of Appendix 2, but for a shift in coordinate origins. Consider now two real functions of the variables X_{J_1}, Y_{J_2}. These will be denoted as

$$g_{\underline{J}} = g(X_{J_1}, Y_{J_2})$$

$$h_{\underline{J}} = h(X_{J_1}, Y_{J_2})$$

defined over the real-space grid. Their product

$$W(X_{J_1}, Y_{J_2}) = W_{\underline{J}} = g_{\underline{J}} h_{\underline{J}}$$

is fully aliased in the sense that all spectral components $|\underline{K}| > \frac{N}{2}$ appear falsely, within the spectral domain $|K| \leq \frac{N}{2}$. The problem is to construct a scheme for evaluation of W such that only those spectral components for which $|\underline{K}| < \frac{N}{2}$ are properly included.

Define, as in Appendix 2, the two-dimensional discrete Fourier transform pair(1,2).

(A3.1) $$f_{\underline{J}} = \sum_{\substack{\underline{K} \\ |\underline{K}| \leq N/2}} F_{\underline{K}}\, e^{\frac{2\pi i}{N} \underline{K}\cdot\underline{J}} = \text{say, } DF_{\underline{K}}$$

where $\sum_{\underline{K}}$, $|\underline{K}| \leq N/2$ is taken to mean $-\frac{N}{2} \leq K_1, K_2 < \frac{N}{2}$.

The inverse DFT is

(A3.2) $$F_{\underline{K}} = \frac{1}{N^2} \sum_{\underline{J}} f_{\underline{J}}\, e^{-\frac{2\pi i}{N} \underline{K}\cdot\underline{J}} = D^{-1} f_{\underline{J}}$$

where $\sum_{\underline{J}}$ is taken to mean $0 \leq J_1, J_2 \leq N-1$.

Then the DFT of the fully aliased local product $W_{\underline{J}}$ is

$$W_{\underline{K}} = D^{-1} W_{\underline{J}} = \frac{1}{N^2} \sum_{\underline{J}} g_{\underline{J}}\, h_{\underline{J}}\, e^{-\frac{2\pi i}{N} \underline{K}\cdot\underline{J}}$$

(A3.3) $$= \frac{1}{N^2} \sum_{\underline{J}} \sum_{\underline{K}'} G_{\underline{K}'}\, e^{+\frac{2\pi i}{N} \underline{K}'\cdot\underline{J}} \sum_{\underline{K}''} H_{\underline{K}''}\, e^{+\frac{2\pi i}{N} \underline{K}''\cdot\underline{J}}\, e^{-\frac{2\pi i}{N} \underline{K}\cdot\underline{J}} .$$

By rearrangement of order of summations we have

(A3.4) $$W_{\underline{K}} = \frac{1}{N^2} \sum_{\underline{K}'} \sum_{\underline{K}''} G_{\underline{K}'}\, H_{\underline{K}''} \sum_{\underline{J}} e^{\frac{-2\pi i}{N}(\underline{K}-(\underline{K}'+\underline{K}''))\cdot\underline{J}}$$

where

$$G_{\underline{K}} = D^{-1} g_{\underline{J}}$$

$$H_{\underline{K}} = D^{-1} h_{\underline{J}} .$$

---

(1) The notation $\underline{K}\cdot\underline{J}$ is understood to mean the scalar dot product $K_1J_1 + K_2J_2 + K_3J_3$.

(2) The notation D is shorthand for the inverse Fourier transformation operation applied to $F_{\underline{K}}$.

The orthogonality relationships can be written as

$$\text{(A3.5)} \qquad \sum_{J_1=0}^{N-1} e^{-\frac{2\pi i}{N}(K_1-(K_1' + K_1''))J_1} = N, \text{ if } K_1=(K_1' + K_1'') \text{ modulo } N$$
$$= 0, \text{ otherwise .}$$

Since $|K_1'| \le \frac{N}{2}$, $|K_1''| \le \frac{N}{2}$, then $|K_1' + K_2'| \le N$ and the summation (A3.5) = N, if $K_1 = (K_1' + K_1'')$ or $(K_1' + K_1'' + N)$, or $(K_1' + K_1'' - N)$. Similar orthogonal relationships hold for summation over index J_2. Therefore, the summation over index J_2. Therefore, the summation

$$\sum_{\underline{J}} e^{\frac{2\pi i}{N}(\underline{K} - (\underline{K}' + \underline{K}''))\cdot\underline{J}}$$

$$= N^2, \quad \text{if} \quad \left\{\begin{array}{lcl} K_1' + K_1'' = K_1 & & K_2' + K_2'' = K_2 \\ K_1' + K_1'' = K_1 - N & \text{and} & K_2' + K_2'' = K_2 - N \\ K_1' + K_1'' = K_1 + N & & K_2' + K_2'' = K_2 + N \end{array}\right\}$$

and $\qquad = 0$, otherwise

(A3.4) may therefore be written out fully as

$$\left\{\begin{array}{l} \displaystyle\sum_{K_1'+K_1''=K_1} \sum_{K_2'+K_2''=K_2} + \sum_{K_1'+K_1''=K_1+N} \sum_{K_2'+K_2''=K_2} + \sum_{K_1'+K_1''=K_1-N} \sum_{K_2'+K_2''=K_2} \\ \displaystyle + \sum_{K_1'+K_1''=K_1} \sum_{K_2'+K_2''=K_2+N} + \sum_{K_1'+K_1''=K_1+N} \sum_{K_2'+K_2''=K_2+N} + \sum_{K_1'+K_1''=K_1-N} \sum_{K_2'+K_2''=K_2+N} \\ \displaystyle + \sum_{K_1'+K_1''=K_1} \sum_{K_2'+K_2''=K_2-N} + \sum_{K_1'+K_1''=K_1+N} \sum_{K_2'+K_2''=K_2-N} + \sum_{K_1'+K_1''=K_1-N} \sum_{K_2'+K_2''=K_2-N} \end{array}\right\}$$

$$^{*}G_{K_1', K_2'} \quad H_{K_1'', K_2''}$$

whence

$$(A3.6)\quad W_{K_1,K_2} = \overline{W}_{K_1,K_2} + \overline{W}_{K_1+N,K_2} + \overline{W}_{K_1-N,K_2}$$
$$+ \overline{W}_{K_1,K_2+N} + \overline{W}_{K_1+N,K_2+N} + \overline{W}_{K_1-N,K_2+N}$$
$$+ \overline{W}_{K_1,K_2-N} + \overline{W}_{K_1+N,K_2-N} + \overline{W}_{K_1-N,K_2-N}$$

where

$$\overline{W}_{K_a,K_b} = \sum_{K_1'+K_1''=K_a} \sum_{K_2'+K_2''=K_b} G_{K_1',K_2'} \; H_{K_1'',K_2''} \; .$$

The first term on the right hand side of (A3.6), $\overline{W}_{K_1,K_2}$, is the desired alias-free convolution of $G_{\underline{K}}$ and $\underline{H}_{\underline{K}}$, i.e.,the D^{-1} transform of the alias-free product of $g_{\underline{J}}$ and $h_{\underline{J}}$. Each of the other terms in A3.6 implies the presence of aliased contribution of the form $K_1 \pm N$, etc. The task now is to isolate the first term from the other eight terms on the right hand side of (A3.6). To achieve this in economical fashion, Orszag has introduced the "shifted-grids" procedure. There are a number of variants of this method, but we will choose the "quartergrid" scheme as particularly convenient. Let us define the four shifted grids

$$\underline{J}_{\underline{S}_p} = (J_1 + \frac{S_1}{4}p,\; J_2 + \frac{S_2}{4}p) \qquad (p=1, \cdot\cdot 4)$$

where

$$\underline{S}_p = (S_{1_p}, S_{2_p})$$

$$\underline{S}_1 = (1,1); \quad \underline{S}_2 = (-1,-1); \quad \underline{S}_3 = (-1,+1); \quad \underline{S}_4 = (+1,-1).$$

(The shifted grids are introduced for the purpose of developing expressions which permit the isolation of the alias-free term.)

For each shifted grid (p=1,··4), define

$$\text{(A3.7)} \qquad g_{(\underline{J}_{\underline{S}_p})} = \sum_{\underline{K}} G_{\underline{K}}\, e^{\frac{2\pi i}{N}\, \underline{K}\cdot\underline{J}_{\underline{S}_p}}$$

$$\text{(A3.8)} \qquad h_{(\underline{J}_{\underline{S}_p})} = \sum_{\underline{K}} H_{\underline{K}}\, e^{\frac{2\pi i}{N}\, \underline{K}\cdot\underline{J}_{\underline{S}_p}}$$

and define

$$\text{(A3.9)} \qquad W^{\underline{S}_p}_{K_1,K_2} = D^{-1}\; g_{(\underline{J}_{\underline{S}_p})} \cdot h_{(\underline{J}_{\underline{S}_p})}$$

$$= \frac{1}{N^2} \sum_{K'_1} \sum_{K'_2} \sum_{K''_1} \sum_{K''_2} G_{K'_1,\,K'_2}\; H_{K''_1,\,K''_2} \sum_{J_1} \sum_{J_2} \exp\; \left(\frac{2\pi i}{N}\right) \Big[(K'_1+K''_1-K_1) \times (J_1+\frac{S_{1p}}{4}) + (K'_2+K''_2-K_2)(J_2+\frac{S_{2p}}{4})\Big] .$$

Again using the orthogonality relationships

$$\sum_{J_1} \sum_{J_2} \exp\; \left(\frac{2\pi i}{N}\right) \Big[(K'_1+K''_1-K_1) \times (J_1+\frac{S_{1p}}{4}) + (K'_2+K''_2-K_2)\;(J_2+\frac{S_{2p}}{4})\Big] = N^2\; e^{\frac{2\pi i}{N}\left(K^*_1 \frac{S_{1p}}{4} + K^*_2 \frac{S_{2p}}{4}\right)}$$

where

$$K^*_1\;,\; K^*_2 \;=\; 0,\; \pm\, N \;\; \text{only}.$$

Thus, evaluating the quadruple sums $\sum_{K'_1} \cdots \sum_{K''_2}$ for each of the shifted grids in turn, we find:

(A3.10a)

$$W^{\underline{S}_1}_{K_1,K_2} = \bar{W}_{K_1,K_2} + i\,\bar{W}_{K_1,K_2+N} - i\,\bar{W}_{K_1,K_2-N}$$

$$+ i\,\bar{W}_{K_1+N,K_2} - i\,\bar{W}_{K_1-N,K_2} - \bar{W}_{K_1+N,K_2+N}$$

$$+ \bar{W}_{K_1-N,K_2+N} + \bar{W}_{K_1+N,K_2-N} - \bar{W}_{K_1-N,K_2-N}$$

(A3.10b)

$$W^{\underline{S}_2}_{K_1,K_2} = \bar{W}_{K_1,K_2} - i\,\bar{W}_{K_1,K_2+N} + i\,\bar{W}_{K_1,K_2-N} + i\,\bar{W}_{K_1+N,K_2}$$

$$- i\,\bar{W}_{K_1-N,K_2} + \bar{W}_{K_1+N,K_2+N} - \bar{W}_{K_1-N,K_2+N}$$

$$+ i\,\bar{W}_{K_1+N,K_2-N} - i\bar{W}_{K_1-N,K_2-N}$$

(A3.10c)

$$W^{\underline{S}_3}_{K_1,K_2} = \bar{W}_{K_1,K_2} + i\,\bar{W}_{K_1,K_2+N} - i\,\bar{W}_{K_1,K_2-N}$$

$$- i\,\bar{W}_{K_1+N,K_2} + i\,\bar{W}_{K_1-N,K_2} + \bar{W}_{K_1+N,K_2+N}$$

$$- \bar{W}_{K_1+N,K_2+N} - \bar{W}_{K_1+N,K_2-N} + \bar{W}_{K_1-N,K_2-N}$$

(A3.10d)

$$W^{\underline{S}_4}_{K_1,K_2} = \bar{W}_{K_1,K_2} - i\,\bar{W}_{K_1,K_2+N} + i\,\bar{W}_{K_1,K_2-N}$$

(A3.10d) (Cont'd)

$$- i \bar{W}_{K_1+N,K_2} + i \bar{W}_{K_1-N,K_2} - \bar{W}_{K_1+N,K_2+N}$$

$$+ \bar{W}_{K_1-N,K_2+N} + \bar{W}_{K_1+N,K_2-N} - \bar{W}_{K_1-N,K_2-N} .$$

Thus:

$$W^{\underline{S}_1}_{K_1,K_2} + W^{\underline{S}_2}_{K_1,K_2} + W^{\underline{S}_3}_{K_1,K_2} + W^{\underline{S}_4}_{K_1,K_2} = 4\bar{W}_{K_1,K_2}$$

whence we have the remarkable result

(A3.11)

$$\bar{W}_{K_1,K_2} = \frac{1}{4} \sum_{\substack{\underline{S}_p \\ p=1,\cdots 4}} W^{\underline{S}_p}_{K_1,K_2} .$$

Finally, by performing one further DFT

(A3.12)

$$\bar{W}_{J_1,J_2} = D\bar{W}_{K_1,K_2}$$

we recover the *alias-free* product of $g_{\underline{J}}$ and $h_{\underline{J}}$.

As outlined above, the grid-shifting procedure requires *twelve* DFT operations, namely

$$\left.\begin{array}{l} \tilde{G}_K \to g_{\underline{J}_{\underline{S}_p}} \\ \tilde{H}_K \to h_{\underline{J}_{\underline{S}_p}} \\ (g_{\underline{J}_{\underline{S}_p}} \quad h_{\underline{J}_{\underline{S}_p}}) \to W^{\underline{S}_p} \end{array}\right\} (p=1, \cdots 4).$$

Orszag shows that it is possible to save half of these operations by a simple modification to the above scheme, as follows:

(a) use only one diagonal pair of shifted grids, say

$$\underline{J}_{\underline{S}_1} \text{ and } \underline{J}_{\underline{S}_2};$$

(b) perform evaluations (A3.7, 3.8);

(c) replace (A3.11) with

$$\overline{W}'_{K_1,K_2} = \frac{1}{2} \sum_{p=1}^{2} W^{\underline{S}_p}_{K_1,K_2}$$

where the prime signifies that $\overline{W}'_{K_1,K_2}$ is not yet the alias-free convolution of G_K and H_K;

(d) truncate the field $\overline{W}'$ to the wave-space region

$$0 \leq (K_1^2 + K_2^2)^{1/2} < \frac{N}{2}$$

and let

$$\overline{W}_{K_1,K_2} = (\overline{W}'_{K_1,K_2})_{\text{TRUNCATED}};$$

(e) obtain the alias-free real-space product field by performing operation (A3.12).

The corresponding algorithm for three-dimensional systems is considerably more complex in implementation, but is conceptually identical.

Appendix 4

The Fast Fourier Transform

The basic algorithms underlying the Fast Fourier Transform are well documented in the literature (Gentleman and Sande 1966, Cooley and Tukey 1965).

The definition of the discrete Fourier transform (DFT) defined over the one-dimensional string of N data points $D_j (j=0, \ldots, N-1)$ can be written as

$$\text{(A4.1)} \quad T_K = \frac{1}{\sqrt{N}} \sum_{j=0}^{N-1} D_j W^{jk}, \quad W=e^{2\pi i/N}, \quad k=0, \ldots, N-1.$$

(where we have incorporated $\sqrt{N}$ normalization in each direction, in contrast to the one-way $1/N$ normalization used in Appendix 2).

Explicitly for $N=8$,

$$\text{(A4.2)} \quad \begin{aligned} \sqrt{8}\, T_0 &= D_0 W^0 + D_1 W^0 + D_2 W^0 + \ldots \\ \sqrt{8}\, T_1 &= D_0 W^0 + D_1 W^1 + D_2 W^2 + \ldots \\ \sqrt{8}\, T_2 &= D_0 W^0 + D_1 W^2 + D_2 W^4 + \ldots \\ \sqrt{8}\, T_3 &= D_0 W^0 + D_1 W^3 + D_2 W^6 + \ldots \\ &\ldots\ldots \end{aligned}$$

Naively, to perform the evaluation of T_K, one would compute directly from (A4.2). This would require 64 complex multiplications and 56 complex additions. However, the trigonometric function $W^{jk} = e^{2\pi ijk/N} = \cos \frac{2\pi jk}{N} + i \sin \frac{2\pi jk}{N}$ possesses two important properties namely:

(1) Periodicity ... $W^N = e^{2\pi iN/N} = 1$, so that for $N=8$, $W^8 = W^0 = 1$, $W^9 = W$, $W^{10} = W^2$, etc.

(2) Symmetry ... For N a power of two, we may utilize the

reflections of the cosine and sine functions in the eight octants: $W^2 = i$, $W^3 = iW$, $W^4 = -1$, $W^5 = -W$, etc.

Hence, expressions (A4.2) reduce to 32 multiplications and 56 additions:

(A4.3)

$$\sqrt{8}\ T_0 = D_0 + D_1 + D_2 + D_3 + D_4 + D_5 + D_6 + D_7$$

$$\sqrt{8}\ T_1 = D_0 + D_1W + D_2i + D_3iW - D_4 - D_5W - D_6i - D_7iW$$

$$\sqrt{8}\ T_2 = D_0 + D_1i - D_2 - D_3i + D_4 + D_5i - D_6 - D_7i$$

$$\sqrt{8}\ T_3 = D_0 + D_1iW - D_1i + D_3W - D_4 - D_5iW + D_6i - D_7W$$

$$\sqrt{8}\ T_4 = D_0 - D_1 + D_2 - D_3 + D_4 - D_5 + D_6 - D_7$$

$$\sqrt{8}\ T_5 = D_0 - D_1W + D_2i - D_3iW - D_4 + D_5W - D_6i - D_7iW$$

$$\sqrt{8}\ T_6 = D_0 - D_1i - D_2 + D_3i + D_4 - D_5i - D_6 + D_7i$$

$$\sqrt{8}\ T_7 = D_0 - D_1iW - D_2i - D_3W - D_4 + D_5iW + D_6i + D_7W\ .$$

By adroit grouping of terms in (A4.3), it is possible to reduce the amount of computation still further. Proceeding systematically, define:

$$A_0 = D_0/\sqrt{8}$$
$$A_1 = D_4/\sqrt{8}$$
$$A_2 = D_2/\sqrt{8}$$
$$A_3 = D_6/\sqrt{8}$$
$$A_4 = D_1/\sqrt{8}$$
$$A_5 = D_5/\sqrt{8}$$

(A4.4) (Cont'd)

$A_6 = D_3/\sqrt{8}$

$A_7 = D_7/\sqrt{8}$.

Next:

(A4.5)

$B_0 = A_0 + A_1$

$B_1 = A_0 - A_1$

$B_2 = A_2 + A_3$

$B_3 = (A_2 - A_3)i$

$B_4 = A_4 + A_5$

$B_5 = A_4 - A_5$

$B_6 = A_6 + A_7$

$B_7 = (A_6 - A_7)i$

$C_0 = B_0 + B_2$

$C_1 = B_1 + B_3$

$C_2 = B_0 - B_2$

$C_3 = B_1 - B_3$

$C_4 = B_4 + B_6$

$C_5 = (B_5 + B_7)W$

$C_6 = (B_4 - B_6)i$

$C_7 = (B_5 - B_7)iW$

$T_0 = C_0 + C_4$

$T_1 = C_1 + C_5$

$T_2 = C_2 + C_6$

$T_3 = C_3 + C_7$

$T_4 = C_0 - C_4$

(A4.5) (Cont'd)

$$T_5 = C_1 - C_5$$

$$T_6 = C_2 - C_6$$

$$T_7 = C_3 - C_7 \ .$$

Excluding the normalization of (A4.4), we have accomplished the DFT in only 5 complex multiplications and 24 complex additions. In general, when N is a power of two, the Fast Fourier Transform (FFT) performs a DFT in only $\frac{N}{2}\ \log_2 N$ complex multiplications (for $N \geq 32$) and only $N \log_2 N$ complex additions. Comparatively, the naive approach to (A4.2) requires N^2 multiplications and N^2 additions.

The flow diagram below displays the FFT technique of (A4.4) and (A4.5). A circle of the form $\textcircled{\pm/_n}$ means to add (subtract) all the values flowing in from the left and then to multiply by W^n. An empty circle means do nothing to the incoming value.

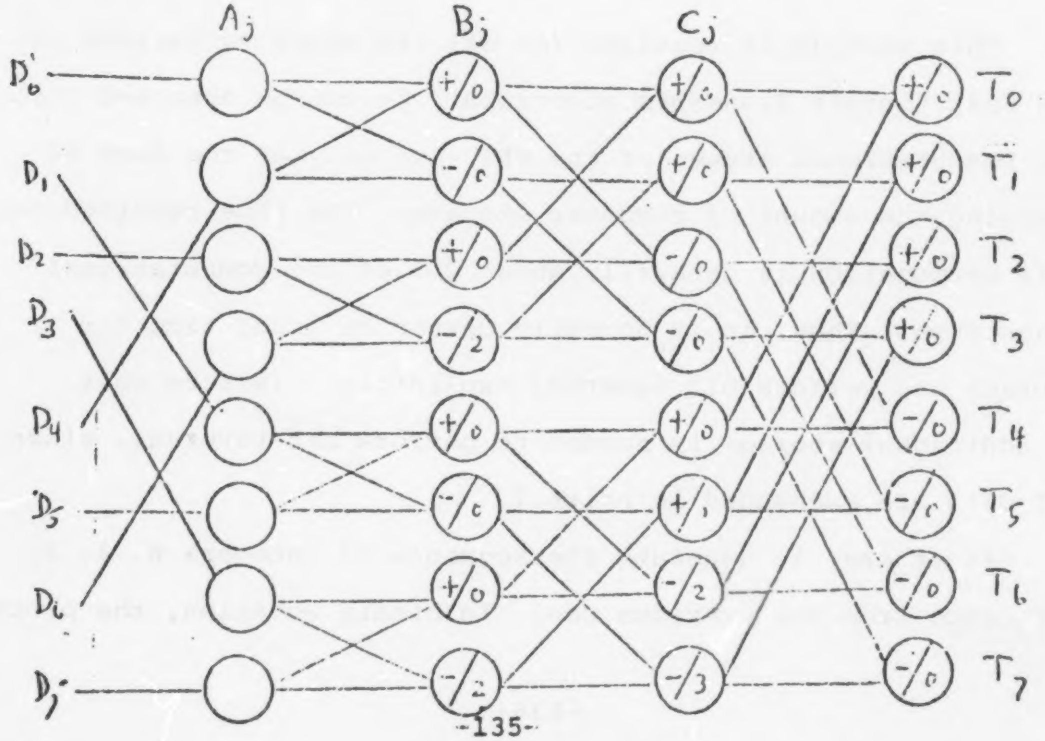

Notice that the first stage of the calculations, (A4.4), performs a peculiar permutation of the data.

Index before	Index after
0	0
1	4
2	2
3	6
4	1
5	5
6	3
7	7

Writing these indices in binary notation, we see why this process has received the name "bit reversal":

Index before	Index after
000	000
001	100
010	010
011	110
100	001
101	101
110	011
111	111

This sorting is required for all the major variations of the Fast Fourier Transform algorithm. It can be absorbed into the computational stages of the FFT, but only at the cost of doubling the amount of computer storage. The time required for this permutation is generally about 25% of the computational stage time. Thus, it is normally better to trade time for storage and perform bit reversal explicitly. (Notice that no additional storage is needed to perform bit reversal, since all data are exchanged in pairs.)

It is easy to generate the sequence of integers 0, 1, 2, etc., each from the previous one. In binary notation, the process may be stated as: add one to the low order bit, and carry upward if it overflows (becomes larger than one), repeating with higher order bits until no further overflows occur. Similarly, beginning with 0, which is certainly the bit reversal of the integer 0, we generate the reversal of the successive integers by an analogous process: add 1 to the highest bit of the reversed index; if it overflows, carry one to the next-lower bit, repeating with lower order bits until no further overflow occurs.

E.g., for N=8, we start with 000 and add one to the high-order bit:

100 = 4.

Generate the next reversed integer by adding a high order one:

200→010 = 2.

Again add one:

110 = 6.

And again

210→020→001 = 1.

And so forth.

In a high-level language like Fortran, an integer may be tested for the value (0 or 1) of the high-order bit by comparing it to N/2; the high bit is 1 if the integer is greater than N/2. If the high bit is 0, then we must test the second highest bit by comparing to N/4, and so on.

Appendix 5

Construction of Initial Perturbation Flow Field

The initial flow fields specified in this model, as described in chapter 6, are of two types:

(a) the mean velocity field, with a suitable shear structure $\overline{U}(z)$,

(b) the perturbation velocity field, which is comprised of a large ensemble of small-amplitude incompressible modes, distributed in statistically homogeneous and isotropic manner, and obeying a designated spectral power law $E(k)$. This Appendix describes the process by which such a perturbation field is constructed in wave space.

Let us define the two random processes $\underline{\alpha}(\underline{k})$ and $\underline{\beta}(\underline{k})$, which are independent, real vector fields, uniformly distributed over the interval [0,1] satisfying $<\alpha_i(\underline{k})\alpha_j(\underline{k}')> = <\beta_i(\underline{k})\beta_j(\underline{k}')>=0$ $(\underline{k}\neq\underline{k}')$ where $<\cdot\cdot>$ designates ensemble averaging, and $\underline{k}$ is the discretized wavenumber vector. The random processes α and β can be obtained from any of a variety of pseudo-random number generation algorithms. Next, define the vector potential field in wave space as

$$\underline{A}(\underline{k}) = \{[E(k)]^{1/2}/k^2\} + |2\,\ell n\,\alpha(\underline{k})|^{1/2}\,e^{2\pi i\beta(\underline{k})} \quad .$$

Then, we construct the initial perturbation velocity field in wave space $\underline{U}(k)$ as the curl of $\underline{A}(\underline{k})$

$$U(\underline{k}) = i\underline{k} \times A(\underline{k})$$

which automatically guarantees incompressibility. Finally, the real-space perturbation velocity field $\underline{V}(\underline{x})$ is obtained from $\underline{U}(\underline{k})$ by discrete Fourier transformation.